TUNING THE BAND STRUCTURE OF CARBON NANOTUBES

A Dissertation

Presented to the Faculty of the Graduate School

of Cornell University

In Partial Fulfillment of the Requirements for the Degree of

Doctor of Philosophy

by

Ethan Davis Minot

August 2004

TUNING THE BAND STRUCTURE OF CARBON NANOTUBES

Ethan Davis Minot, Ph. D.

Cornell University 2004

The experiments presented in this thesis show that carbon nanotube (NT) electronic structure can be tuned by mechanical stretching and by magnetic fields. These fascinating electromechanical and magnetic effects are quantified using electrical transport techniques.

Nanotubes are thin, hollow cylinders made entirely from carbon atoms. The electron wavestates of a NT are quantized into one-dimensional (1-D) subbands, with each subband corresponding to a different wrapping mode. The 1-D subbands in a NT come in degenerate pairs due to the clockwise/counterclockwise (CW/CCW) symmetry of the wrapping modes. Electron transport though a NT occurs in the pair of subbands with electron states nearest the Fermi level. This pair of subbands can be metallic or semiconducting depending on NT diameter and chirality.

To investigate the electromechanical properties of NTs, electrical transport measurements are combined with *in-situ* atomic force microscopy (AFM) manipulation. Nanotubes suspended over trenches are stretched by pushing with an AFM tip. Electrical measurements taken during stretching reveal dramatic changes in electronic structure near the Fermi level. It is shown that stretching can open a bandgap in metallic subbands and modify the bandgap of semiconducting subbands. These measurements are consistent with theoretical work which predicts that bandgap changes can range between ±100 meV per 1% strain, depending on NT chirality, and that stretching does not break the degeneracy between subband pairs.

Significant changes in electronic structure are also found in magnetic field experiments. Because CW and CCW electron orbitals have opposite magnetic moments, a magnetic field is expected to break the degeneracy between NT subbands. Breaking of subband degeneracy is measured by detecting the charge carriers that are thermally activated across the NT bandgaps, and by measuring the energy shifts of individual electron states in a NT quantum dot. Both techniques show that electron states near the NT bandgaps have large magnetic moments along the NT axis. The measured magnitudes and directions of orbital magnetic moments are consistent with theoretical predictions and are an order of magnitude larger than the Bohr magneton.

BIOGRAPHICAL SKETCH

Ethan Minot attended high school at Awatapu College in Palmerston North, New Zealand, graduating in 1994. He completed a Bachelors of Science with Honours in Physics at Massey University, Palmerston North, in December 1998. His Honours thesis, written in the group of Prof. Paul Callaghan during his last year at Massey, investigated multiple quantum coherences in nuclear magnetic resonance experiments. Ethan began graduate school at the University of California in Berkeley in August 1999 where he joined the group of Prof. Paul McEuen. He followed Prof. McEuen to Cornell University in January 2001.

ACKNOWLEDGMENTS

Many people have helped me complete this thesis.

My advisor, Paul, has been a fantastic mentor and teacher, opening my eyes to new ideas at every step. Thank you for patiently sharing all you know about science and how to communicate science. Thank you, also, for knowing when to push me – I'm grateful I was able to experience the fun of discovery that follows long hours of work.

Thanks for all the help and good company I've had in the McEuen group. It has been such a valuable experience to work with excellent physicists from many different backgrounds: first at Berkeley – Adrian Bachtold, Barry Baker, Michael Furher, Manu Forero, Jeff Gore, Philip Kim, Noah Kubow, Andrew Lim, Jiwoong Park, Chris Vale and Michael Woodside – and later at Cornell – Ken Bosnik, Markus Brink, Scott Bunch, Luke Donev, Shahal Ilani, Lisa Larrimore, Ji-Yong Park, Sami Rosenblatt, Vera Sazonova, Arend van der Zande, Yuval Yaish, Alex Yanson, Xinjian Zhou and Jun Zhu. In particular, thanks to Yuval and Vera, who have contributed so much to the projects in this thesis.

The atmosphere of collaboration between different groups at Cornell has been wonderful. Thanks in particular to Abhay Pasupathy and Alex Champagne, for discussions and help with equipment and to Hande Ustunel for help with nanotube theory.

Friends in Berkeley and in Ithaca have made life fun. Thank you to my Berkeley housemates Andrew and Michelle for a fantastic year and half on Blake St, to Lizzy for unforgettable trips into the Sierras, to Alisa for your wonderful company, and my best friends Nikhil and Uday – I'm sorry I left Berkeley so soon. When I arrived in Ithaca I was warmly welcomed by new housemates on Dryden Rd and later at the

iv

Science Co-op. In Ithaca it has been fantastic hanging out with Nick, Wendy, Jeandrew and Wendy (making crazy trips all over the East coast), and with Mark and Anna (pursuing of crazy projects with you has been as exciting as any rock climb).

Mum, Dad, and my sister Hannah, thank you for putting up with me living so far away - for your love and support as I explore the world. I look forward to every visit home. And Cassie, thank you for walking beside me the last four years, sharing the fun times and challenges alike. Much love.

TABLE OF CONTENTS

LIST OF FIGURES

Page

LIST OF TABLES

CHAPTER 1

INTRODUCTION AND BACKGROUND

1.1 Carbon nanotubes as nanoscale systems

Nanoscale structures are used to study a range of interesting effects that occur when electrons are confined to very small geometries. For example, the quantized electron wavestates in a nanostructure are reflected in measurements of electron transport through the structure. Electron transport experiments have been used to investigate many different nanostructures (Fig. 1.1), including small metal clusters (Ralph et al. 1995), two-dimensional "pancakes" in GaAs-based systems (Kouwenhoven & Marcus 1998), a variety of single molecules (Reed 1999) and carbon nanotubes (Dekker 1999; McEuen et al. 2002). Among these structures, carbon nanotubes (NTs) have some of the most fascinating relationships between nanoscale geometry and transport properties.

Carbon nanotubes are thin, hollow cylinders made entirely of carbon. The walls of a NT are formed from graphene - a honey-comb lattice of carbon atoms. As shown in Fig. 1.2, different orientations between the honey-comb lattice and the cylinder axis of a NT are possible. Several unique properties result from the cylindrical shape and the carbon-carbon bonding geometry of NTs. The electronic structure of a NT is sensitive to the precise arrangement of carbon atoms; some NTs are moderate bandgap semiconductors while others are metallic (Odom et al. 1998; Wildoer et al. 1998). Moreover, when the arrangement of carbon atoms is changed by mechanical stretching, a NT is expected to change from semiconducting to metallic or vice versa (Heyd et al. 1997; Rochefort et al. 1998; Yang et al. 1999; Yang & Han 2000). The cylindrical shape of NTs also leads to interesting magnetic properties. Significant
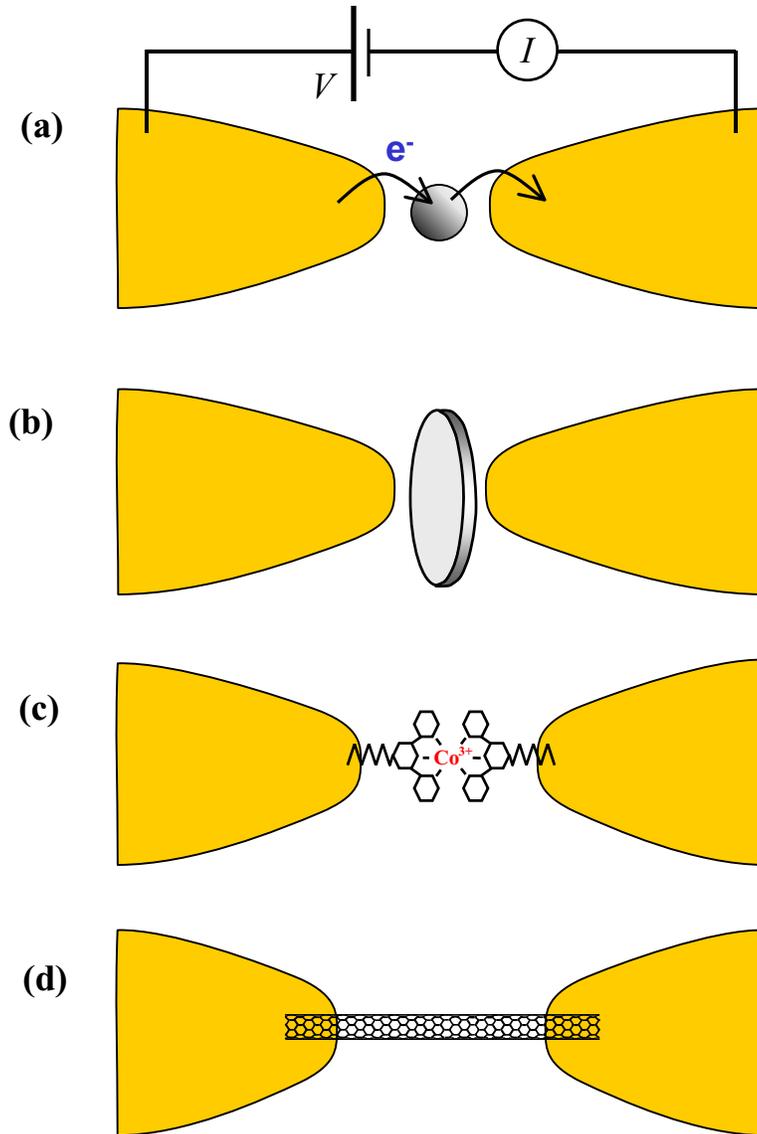
Figure 1.1 Examples of different types of nanostructures that have been studied using electron transport techniques (not drawn to scale). **(a)** A small metal particle (diameter ~ 5nm) very close to a pair of electrodes. A bias applied between the electrodes causes electrons to hop on and off the particle. **(b)** A pancake-shaped GaAs-based structure coupled to electrodes. **(c)** The single-molecule $Co(tpy-(CH_2)_5-SH)_2$ studied by Park et al. (2003). **(d)** A carbon nanotube connected to a pair of electrodes. Depending on the fabrication process the NT/electrode contacts can be tunnel barriers or ohmic contacts.

(a)

(b)

(c)
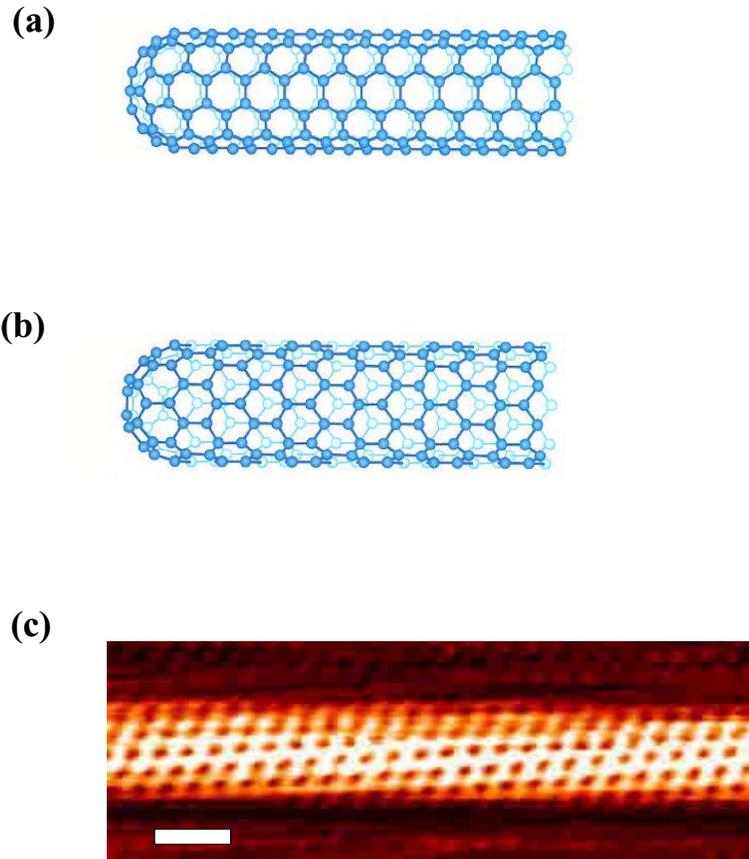
Figure 1.2 Different NT geometries. **(a) (b)** Two examples of how carbon atoms can be arranged in a NT. There are many more possibilities, as discussed in Section 2.2. The NT shown in (a) is metallic, while the NT in (b) is semiconducting. **(c)** Scanning tunneling microscope image of a NT, taken from Wildoer et al. (1998). The scale bar is 1 nm. The bright spots in this image reveal the locations of carbon atoms.

changes in NT electronic structure are expected in applied axial magnetic fields due to Aranov-Bohm-type interference around the NT circumference (Ajiki & Ando 1993; Lu 1995).

The experiments presented in this thesis focus on these beautiful examples of how geometry influences the electronic properties of a nanostructure. This Chapter introduces the concepts and experimental techniques that are used to investigate these electromechanical and magnetic effects in NTs.

1.2 Ballistic transport in nanoscale systems

Nanoscale structures are often smaller than electron scattering lengths. For example, GaAs-based nanostrutures and NTs can have a scattering length $l_{scatter} > 1$ μm. Therefore, NTs and other nanostructures can be used as ballistic conductors, acting as waveguides for electrons. In this section we discuss the Landauer-Buttiker formalism for the ballistic transmission of electrons (reviewed by Datta 1995). The Landauer-Buttiker formalism leads us to the idea of conductance quantization, our starting point for understanding electron transport in NTs.

Electron wavestates encircling a NT are quantized into "wrapping modes." Within each wrapping mode there is a continuum of wavestates along the NT axis described by wave numbers $k_{\parallel}$. The $k_{\parallel}$ states associated with each wrapping mode form one-dimensional (1-D) conduction channels (also refered to as 1-D subbands). To calculate how much current can pass through a 1-D channel we must consider the balance of left-moving and right-moving electrons in the channel. In equilibrium, every 1-D subband will have equal number of left- and right-moving electrons. If a bias is applied, however, left- and right-moving states can be unequally populated. Figure 1.3 shows a 1-D subband connected to two electrodes. The chemical potential of the right electrode μ_R is raised slightly above that of the left electrode. Electrons

(a)

μ_L I μ_R

(b)

E

$\mu_L = \mu_R$

Filled left-moving states | Filled right-moving states

$k_{\parallel}$

(c)

$\downarrow eV_{bais}$ μ_R

μ_L

states contributing to net current

$k_{\parallel}$
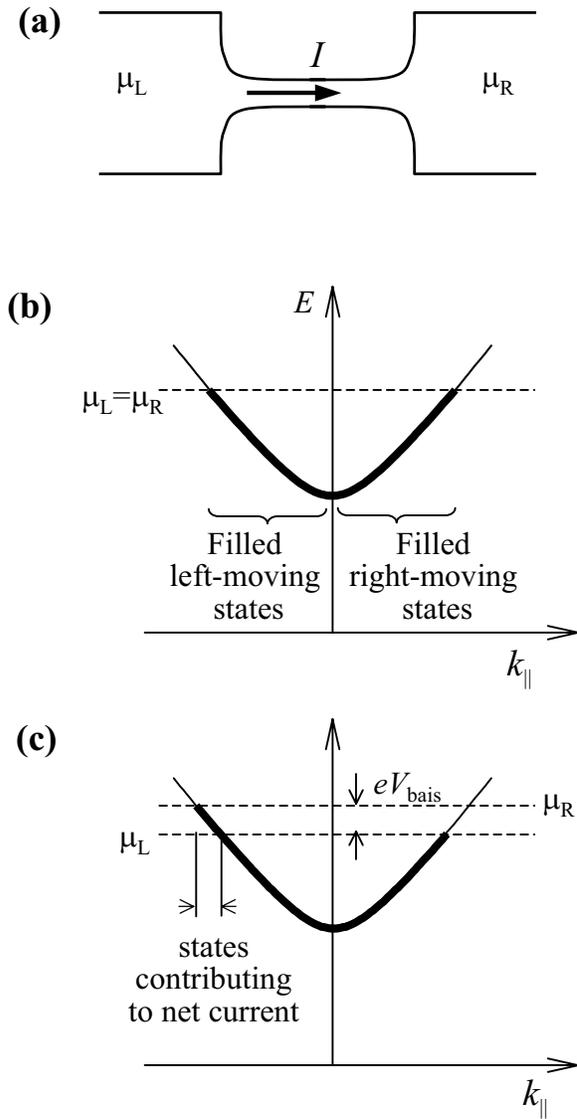
Figure 1.3 (a) A narrow channel connecting a pair of electrodes. The left and right electrodes are large electron reservoirs with chemical potential μ_L and μ_R. If $\mu_L \neq \mu_R$ a net current I can flow between the electrodes. **(b)** The energy and occupancy of electron states in a 1-D mode of the narrow channel. Left- and right-moving states are equally occupied (net current $I = 0$) since $\mu_L = \mu_R$. **(c)** $\mu_R > \mu_L$. More left-moving electron states are occupied than right-moving states and $I > 0$.

entering the 1-D channel from the left populate right-moving states, while electrons entering from the right populate left-moving states. A net current, I, flows due to the imbalance of left and right moving electrons. When transport is ballistic (no scattering in the 1-D channel) and the coupling to the electrodes is transmissive (no electrons reflected at the contacts) the net current is given by

$$I = (n_R - n_L)ev = \int \left(\frac{dn}{dE} (f_R(E) - f_L(E)) \right) e \frac{1}{\hbar} \frac{dE}{dk_{\parallel}} dE \qquad (1.1)$$

where n_R and n_L are the number of right and left moving electrons per unit length in the channel, $v = (1/\hbar)\, dE/dk_{\parallel}$ is the velocity of these electrons, dn/dE is the density of states per unit length in the channel, f_R and f_L are the Fermi distributions in the left and right electrodes. Equation 1.1 is simplified by writing $dn/dE = (dn/dk_{\parallel}) / (dE/dk_{\parallel})$. For a 1-D system $dn/dk_{\parallel}$ is simply $1/\pi$ (including spin degeneracy), and we have

$$I = \frac{2e}{h} \int (f_R(E) - f_L(E)) dE \qquad (1.2a)$$

$$= \frac{2e^2}{h} V \qquad (1.2b)$$

The last step follows from the difference in chemical potential, $eV=\mu_R-\mu_L$, between the two electrodes.

Equation 1.2b assumes that transport through the channel is ballistic (no scattering). Scattering is accounted for by assuming that each electron has a probability $|t|^2$ of being transmitted through the channel. Including the effect of scattering we have

$$I = \frac{2e^2}{h}|t|^2 V \,.$$

From these results we see that the conductance of a perfectly contacted, ballistic 1-D channel depends only on fundamental constants. This remarkable prediction of the Landauer-Buttiker formalism is called conductance quantization. The effect was first experimentally verified using electrostatic constrictions in GaAs nanostructures (Van Wees et al. 1988; Wharam et al. 1988).

In NTs the 1-D channels come in degenerate pairs, due to the clockwise/anti-clockwise symmetry of the wrapping modes around a cylinder. A metallic NT has one pair of channels with energies that overlap the Fermi level. At low bias, only this pair of channels can be unequally populated with left- and right-moving electrons; all other wrapping modes remain completely filled or completely empty. Therefore, a perfectly contacted metallic NT, with length smaller than l_{scatter}, is expected to have a quantized conductance $2(2e^2/h)$ (= 6.5 kΩ^{-1}). Indeed, well contacted metallic NTs with length ~ 200 nm are found to have conductance of nearly $4e^2/h$ (Kong et al. 2001; Liang et al. 2001).

1.3 Semiconducting nanotubes

In semiconducting NTs there is an energy range in which no electron states exist. Because of this energy gap interrupting the 1-D channels of a semiconducting NT, conductance can be turned on and off by an electric field (Tans et al. 1998). This field-effect transistor (FET) behavior has possible technological applications. It is hoped that NTs can be used in densely packed integrated circuits or as tiny sensors. In the context of this thesis, FET behavior is extremely useful for measuring NT energy gaps and how these gaps change with mechanical stretching or applied magnetic field.

A typical NT transistor geometry is shown in Fig. 1.4a. A conducting plane, also called a gate, lies underneath an electrically contacted NT. The NT and the gate form two sides of a capacitor – a voltage difference will cause opposite charge to accumulate on the NT and the gate. The number of electrons on a NT can be controlled in this way. Conductance is turned on when the number of electrons on the NT is such that a 1-D channel (either above or below the energy gap) is partially occupied. Conduction is turned off when the 1-D channels above (below) the energy gap are empty (filled). A semiconducting NT in the "on" state, like a metallic NT, is expected to have maximum conductance of $4e^2/h$. Semiconducting NTs with ohmic electrical contacts have been observed with on-state conductance $\sim 4e^2/h$ (Javey et al. 2003; Yaish et al. 2004).

Band diagrams (see Fig. 1.4c) are used to show how different parts of a NT are affected by an applied electric field. Figure 1.4c shows the combined chemical energy plus electrostatic energy of the highest-energy valence state and lowest-energy conduction state in a NT as a function of position along the tube. The energy gap separating these states in a typical semiconducting NT is $E_{gap} \sim 0.5$ eV. The Fermi level in Fig. 1.4c is aligned below the valence band edge. This is known to happen when semiconducting NTs are contacted to certain metals (for example Pt (Javey et al. 2003) or Au with a Cr adhesion layer (Park & McEuen 2001)). When $V_g = 0$ there are unoccupied valence states, and current can pass through the NT. Because conductance is via unoccupied valence states, the NT is a conductor with positive-type charge carriers (p-type). As the gate voltage is increased ($V_g > 0$) valence states become completely filled in the middle of the NT. The NT is in the "off" state and conductance drops. Changes in electrostatic energy are greatest in the middle section of the NT because the electric field is screened close to the electrodes. As V_g is increased further the chemical-potential energy of states in the middle of the NT is

(a)

V_{bias}

NT

I

dielectric

V_g

gate

(b)

G (e^2/h)

1.0

0

off
state

-10   0   10

V_g (V)

(c)

$V_g = 0V$ $V_g \sim 4V$ $V_g > 4V$

off state

E_{gap} C

E_F V P_{tunnel}

$x_{tube\ axis}$
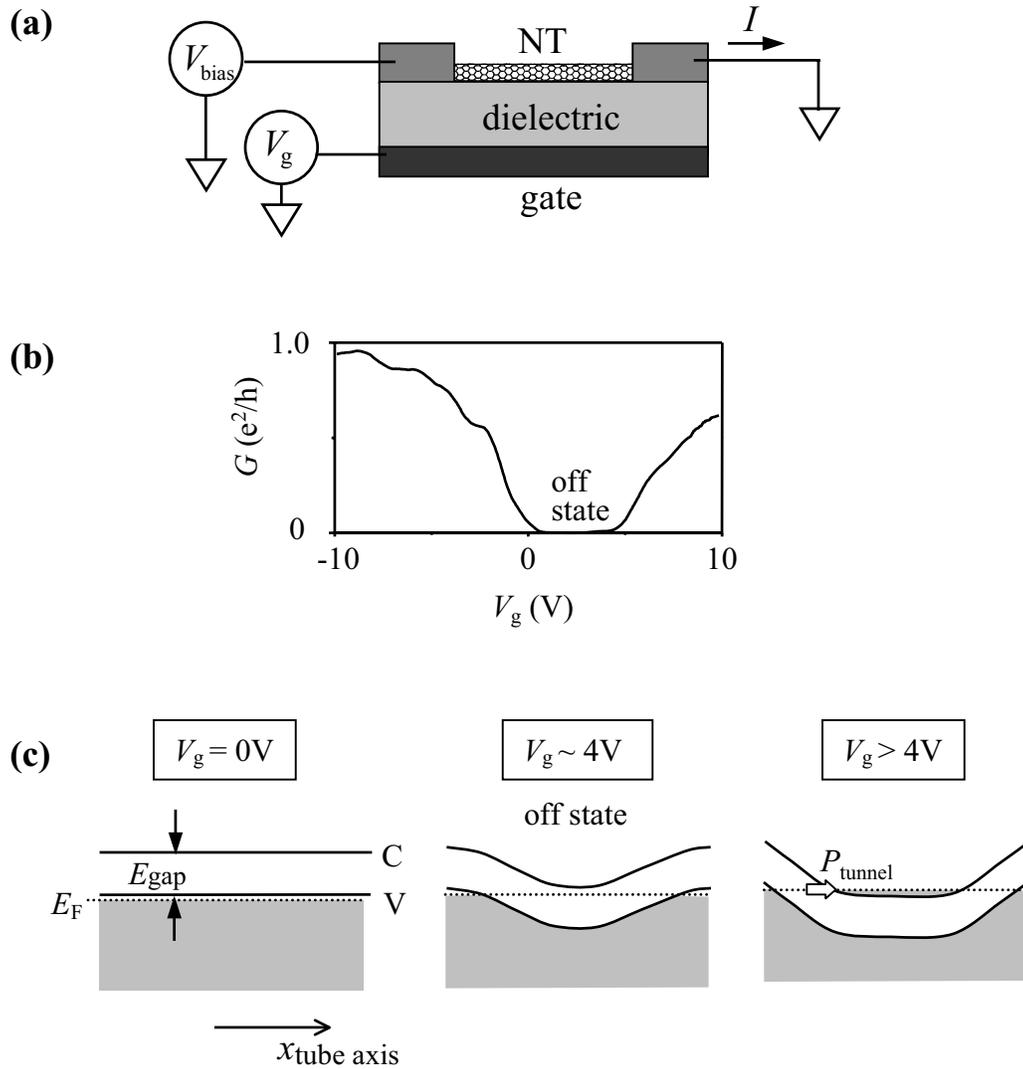
Figure 1.4 A nanotube transistor. **(a)** Side view of a typical NT transistor
geometry. The NT is insulated from the gate by a dielectric material, typically
SiO_2. **(b)** The conductance of a NT device, G, changes as a function of gate
voltage V_g. **(c)** Band diagrams of the NT device at different V_g. The NT conducts
when $V_g < 0$ because valence states are partially filled. Conduction also occurs
when $V_g > 4V$, but is limited by the probability of tunneling from valence states to
conduction states. When $0 < V_g < 4V$ the valence (conduction) band is completely
filled (empty) and the transistor is in the "off state".

lowered far enough so that conduction states become occupied (Fig. 1.4c). The middle

section of the NT is n-type (negative-type charge carriers). At this gate voltage

transport is limited by the p-n tunnel barriers at either end of the NT.

At zero temperature the "off" state of a NT would correspond to a completely

filled valence band and a completely empty conduction band. However, at finite

temperature, thermal activation of electrons over the energy gap results in empty

valence states and occupied conduction states. Therefore, the off-state conductance of

a semiconducting NT is non-zero and depends sensitively on temperature and the size

of E_{gap}. Figure 1.5 shows conductance vs. V_g for a small-bandgap NT ($E_{gap} \sim kT$). This

NT has a much smaller bandgap than the NT in Fig. 1.4b and the two devices have

very different off-state conductance. Measurements of off-state conductance can be

used to quantify NT bandgaps as discussed in Chapters 4 and 5.

1.4 Quantum dot spectroscopy

In the previous section we saw how the energy gap of a semiconducting NTs is

reflected in field-effect transistor behavior. More information about the energies of

electron states in a NT can be found using quantum dot spectroscopy.

Quantum dots (QDs) are formed when a nanostructure confines electrons in all

three dimensions. In the case of NTs this occurs when electrons are held in the tube by

tunnel barriers at either end (Bockrath et al. 1997; Tans et al. 1997). Due to this

complete confinement, the electrons in a QD occupy a discrete spectrum of energy

levels which can be probed by electron transport experiments (Kouwenhoven et al.

1997; Kouwenhoven & Marcus 1998). In this section we discuss how measurements

of electrons tunneling in and out of a QD are used to study the quantized energy levels

of the dot. In Chapter 5 we use these methods to investigate the coupling between

magnetic field and the electron orbitals in NTs.
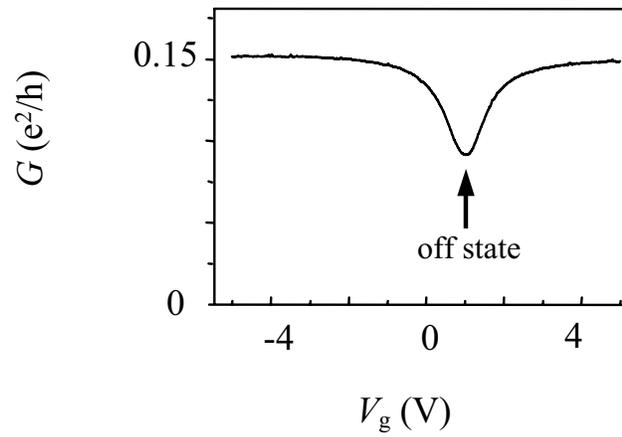
Figure 1.5 Room temperature conductance of a NT with $E_{gap} \sim k_B T$. The off-state conductance is high because many carriers are thermally activated over the small bandgap.

Single-electron charging plays an important role in the transport properties of a QD. Figure 1.6a shows a nanostructure coupled to electrodes via tunnel barriers. From the size scale of the island, L, we estimate the capacitance of the island $C \sim \varepsilon L$. If the number of electrons occupying the dot changes by one, there is an energy cost $\sim e^2/C$. By lowering temperature such that $kT < e^2/C$, the number of electrons, N, on a QD becomes stable (the fluctuations in N due to thermal energy are suppressed). For a typical NT device ($L = 1\mu m$, silicon oxide substrate $\varepsilon = 4\,\varepsilon_0$) this "Coulomb blockade" regime is reached at temperatures below ~ 30K.

The total energy of the N-electron state of a QD depends on the electrostatic environment felt by the electrons and the quantized energy levels occupied by the electrons. In the constant-interaction model (Kouwenhoven et al. 1997), electrostatic interactions are approximated using the capacitance of the dot C, and the energy of the ith quantum state E_i is assumed to be independent of electron number. The energy of the ground state with N electrons is then

$$U(N) = \sum_{i=1}^{N} E_i + \frac{(Ne)^2}{2C},$$

The difference between ground state energies $U(N) - U(N\text{-}1)$ is the electrochemical potential of the dot

$$\mu_{dot}(N) = U(N) - U(N-1) = E_N + \frac{(N-1/2)e^2}{C}$$

The Nth electron will enter the dot if $\mu_{dot}(N)$ is smaller than the electrochemical potential of a nearby electrode. Note that μ_{dot} increases with N; each additional electron raises the total energy of the electronic ground state more than the electron before. The ladder of $\mu_{dot}(N)$ is shown in Fig. 1.6b and c.
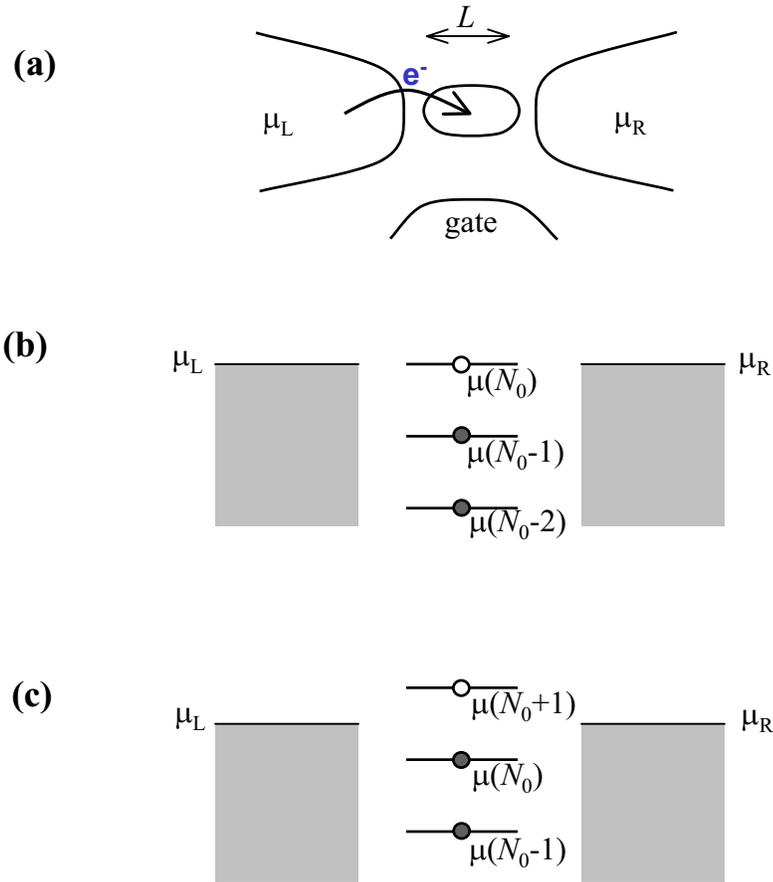
Figure 1.6 Electron transport through a quantum dot. **(a)** A quantum dot with length scale L. Tunnel barriers separate the dot from a pair of electrodes. The dot is capacitively coupled to a gate electrode. **(b)** The chemical potential of the dot (a function of the number of electrons on the dot) and the chemical potential of the electrodes μ_L and μ_R. Because $\mu(N_0)$ is aligned with $\mu_{L,R}$ the occupancy of the dot can fluctuate between N_0 and N_0-1 and low-bias conduction is possible. **(c)** Same as (b) except the dot is stable with N_0 electrons. Low-bias conduction is blocked because electron occupancy cannot fluctuate.

For current to flow through a QD, the number of electrons occupying the dot must fluctuate. In the Coulomb blockade regime ($kT < e^2/C$) this can occur if there exists $\mu_{\text{dot}}(N)$ such that $\mu_L \leq \mu_{\text{dot}}(N) \leq \mu_R$ (or $\mu_L \geq \mu_{\text{dot}}(N) \geq \mu_R$) where μ_L and μ_R are the chemical potentials of the electrodes. Figure 1.6b illustrates the situation where $\mu_L = \mu_{\text{dot}}(N_0) = \mu_R$. The total energy of the system (the two electrodes and the dot) does not change as the occupancy of the dot fluctuates between N_0 and N_0-1 electrons. The N_0^{th} electron makes an equal contribution to the energy of the system whether it is on the dot or one of the electrodes. Because of this degeneracy between N_0 and N_0-1 states, a small bias ($\mu_L - \mu_R \neq 0$) will cause current to flow through the dot. The non-degenerate situation is shown in Fig 1.6b. Here the occupancy of the dot cannot be changed without increasing the overall energy of the system. The dot is stable with N_0 electrons and low-bias current is blocked.

A gate voltage V_g can be used to adjust μ_{dot}, and therefore the conductance of a quantum dot. With the chemical potential of the electrodes held constant we have (Kouwenhoven et al. 1997)

$$\mu_{dot}(N,V_g) = E_N + (N - 1/2)\frac{e^2}{C} - e\frac{C_g}{C}V_g \qquad (1.5)$$

The term in V_g is independent of N since the electric field between gate and dot is felt equally by every electron. Figures 1.6b and c are examples of electrochemical potentials at different values of V_g. If V_g is swept continuously, the electrochemical potential of different charge states will periodically align with $\mu_{L,R}$. A peak in low-bias conductance is expected whenever $\mu_{\text{dot}}(N, V_g)$ aligns with the chemical potential of the electrodes. These "Coulomb peaks" are illustrated in Fig. 1.7a. An expression for the position of the Nth Coulomb peak is found by rearranging Eq. 1.5

(a)

(b)

(c)
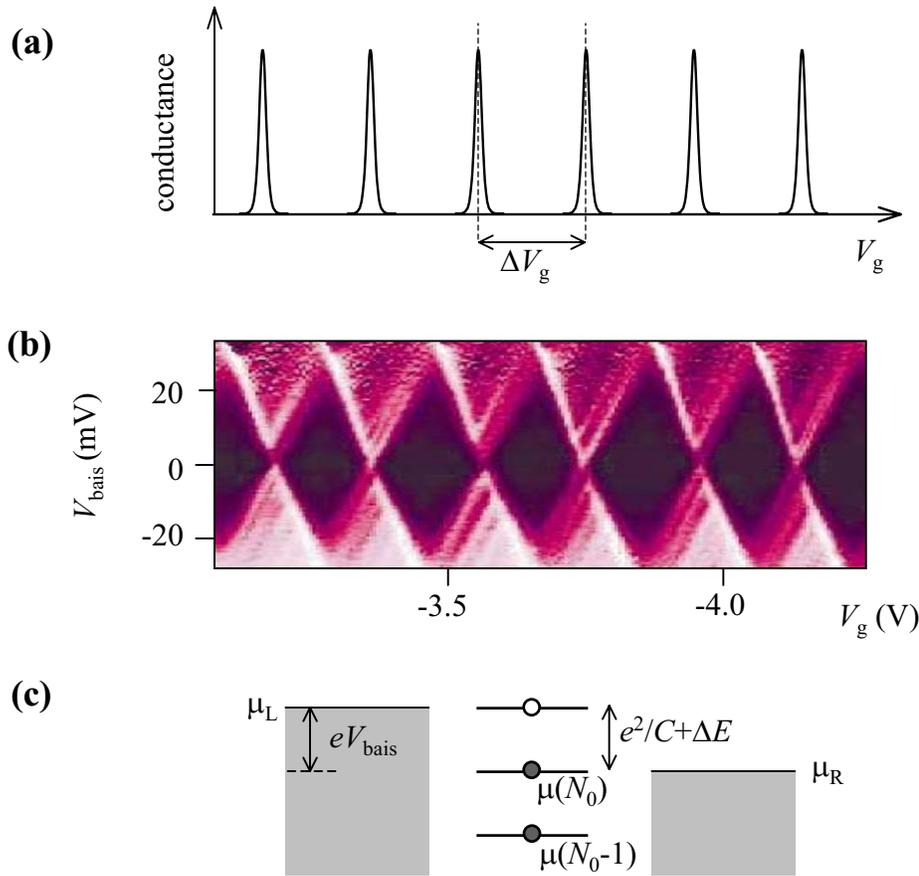
Figure 1.7 (a) Schematic of the low-bias conductance of a QD as a function of V_g. Sharp peaks in conductance occur when μ_{dot} aligns with the electrochemical potential of the electrodes. **(b)** Color plot of differential conductance dI/dV_{bias} of a NTQD as a function of bias $eV_{bias} = \mu_L - \mu_R$, and gate voltage V_g at temperature $T = 4$ K (from Jarillo-Herrero et al. 2004). Black is zero conductance, white is 3 μS. Regions of (V_g, V_{bias}) where current is blocked appear as dark diamonds. The width of the diamonds corresponds to ΔV_g in (a). The height of the diamonds is $e^2/C + \Delta E$ as illustrated in (c). **(c)** Electrochemical potential of the dot and electrodes near the top of a zero conductance diamond. V_g is such that current is blocked for bias $\mu_L - \mu_R < e^2/C + \Delta E$. If V_g is changed, or V_{bias} increased, a charge state of the dot (either N_0 or $N_0 + 1$) will become available to facilitate transport.

$$V_g(N) = \frac{C}{eC_g}\left(E_N + N\frac{e^2}{C}\right) + \text{constant} \qquad (1.6)$$

We see that the constant-interaction model predicts that Coulomb peak positions will reflect the orbital energies E_N.

To use Coulomb peak positions $V_g(N)$ to infer E_N we must find the ratio of total capacitance C to gate capacitance C_g. This ratio is found experimentally by mapping out the conductance of a dot at different V_g and different biases $eV_{bias} = \mu_R - \mu_L$. Figure 1.7b shows a two-dimensional plot of conductance as a function of V_g and V_{bias} for a NTQD. A series of diamonds can be seen where the dot does not conduct current. The width of a diamond is the distance between Coulomb peaks $V_g(N)-V_g(N-1) = (C/eC_g)(\Delta E + e^2/C)$, where $\Delta E = E_N - E_{N-1}$. The height of a diamond is $eV_{bias} = \Delta E + e^2/C$, as illustrated in Fig 1.7c. The ratio of width to height, therefore, gives C/C_g.

1.5 Scanned Probe Techniques

Scanned probe techniques are an indispensable tool for preparing and characterizing NT samples. Basic information, such as NT diameter, is easily measured with a commercial atomic force microscope (AFM). More sophisticated characterization is possible using nano-manipulation techniques and taking advantage of electrical interactions between an AFM tip and a NT.

Figure 1.8b shows an AFM image of a NT on a SiO_2 substrate. A cross-section of this topographic image gives height information about the NT. Care must be taken in interpreting these measurements because the NT is more compressible than the substrate. The apparent NT height in an AFM image can be smaller than the true NT diameter (Postma et al. 2000). Error is minimized by reducing the forces between the AFM tip and the NT.

(a)

(b)

height
(nm)

x position

$F_{elastic}$

(c)
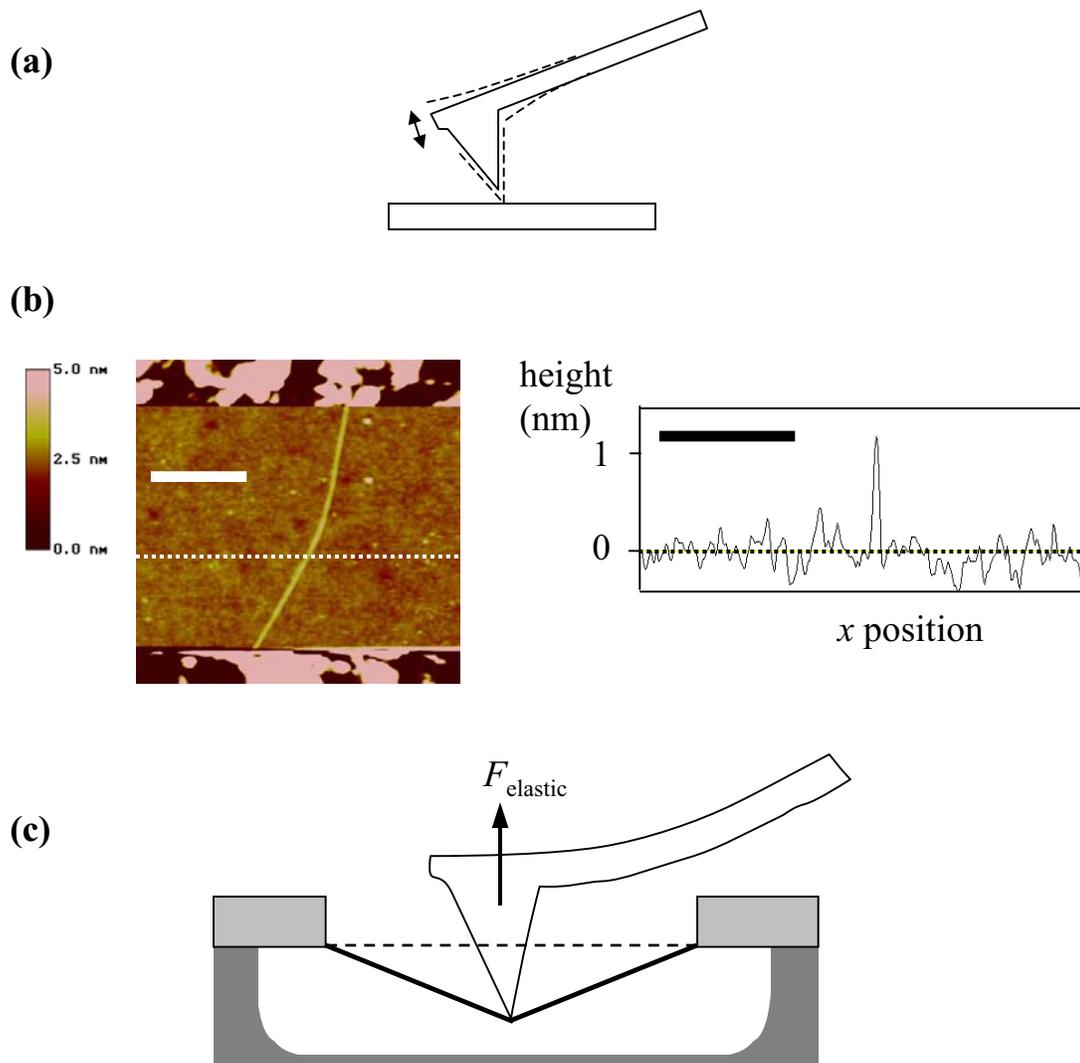
Figure 1.8 Scanning probe techniques. **(a)** An oscillating AFM tip is used to detect the surface. The tip approaches the surface until a drop in oscillation amplitude is detected. Images of surface topography are made by maintaining a constant diminished amplitude. **(b)** A surface topography image of a NT device and a cross section of the image. Scale bars are 300nm. Gold electrodes at the top and bottom of the image are much taller than the NT. A cross section of the image shows the diameter of the NT, $D \approx 1$nm. **(c)** The bending of an AFM cantilever can be used to measure the elastic forces associated with stretching a suspended NT.

A gold coated AFM tip can be used to make low-resistance electrical contacts at any point along a NT (de Pablo et al. 2002; Park et al. 2004; Yaish et al. 2004). This technique is very useful when building NT devices. For example, if multiple NTs are connected to a pair of electrodes, the AFM tip can be used as a third electrode to individually characterize the tubes. Unwanted NTs can then be burnt by injecting large currents from the AFM tip into the selected tube (Park et al. 2002). Using an AFM tip as a third electrode is also useful for investigating different sections of the same NT. For example, in Chapter 5, we measure electrical properties of suspended and unsuspended sections of the same NT. These measurements reveal important interactions between the substrate and NT.

The final use of scanned probe techniques in this thesis is for mechanical manipulation of NTs. Long suspended NTs can be stretched by downward pressure from an AFM tip as shown in Fig. 1.8c (Walters et al. 1999; Tombler et al. 2000; Kim et al. 2002). The exquisite force sensitivity of the AFM allows us to measure the elastic forces associated with stretching the NT. In addition to measuring mechanical forces, the electronic properties of a NT can be measured as it is stretched (Tombler et al. 2000). These techniques are used in Chapters 3 and 4 to study NT mechanical and electromechanical properties.

1.6 Summary and Outline

In this Chapter we reviewed the basic theory of electron transport through nanostructures and the experimental techniques that are used in this thesis. Chapter 2 gives a theoretical overview of NT band structure, emphasizing the effects of mechanical strain and magnetic field on NT band structure. In Chapter 3 we describe experiments that probe the mechanical properties of NTs. In Chapter 4 we show that mechanical stretching changes NT bandgaps. Finally, in Chapter 5, we present

measurements of NT band structure in an applied axial magnetic fields, confirming theoretical predictions for orbital magnetic moments in NTs.

CHAPTER 2

THEORY OF NANOTUBE BAND STRUCTURE

2.1 Introduction

Theoretical work on carbon nanotubes (NTs) has lead to many remarkable predictions (Dresselhaus et al. 2001). In this chapter we focus on two of these predictions. First, the strong coupling between NT electrical properties and mechanical strain (Heyd et al. 1997; Rochefort et al. 1998; Yang et al. 1999; Yang & Han 2000). Second, the large orbital magnetic moments of electrons in NTs (Ajiki & Ando 1993; Lu 1995). We present the theory behind these predictions, emphasizing results that are experimentally tested in Chapters 4 and 5.

Our theoretical treatment begins with a description of the electronic structure of NTs. Other useful reviews of NT electronic structure are found in (White & Mintmire 1998; McEuen 2000; Dresselhaus et al. 2001). With a clear picture of the allowed electronic states in a NT, we then explore the effects of mechanical strain and magnetic field.

2.2 Rolled up graphene

Carbon nanotubes have a cylindrical structure. The cylinder is formed from graphene – a honey-comb lattice of covalently bonded carbon atoms (Fig. 2.1). There are many possible NT geometries, depending on how graphene is rolled into a cylinder and whether the NT is strained. Subtle geometric variables, such as the alignment between the cylinder axis and the graphene crystal axes, strongly influence the electrical properties of a NT.

(a)

(b)

$(n_1, n_2){=}(5,5)$
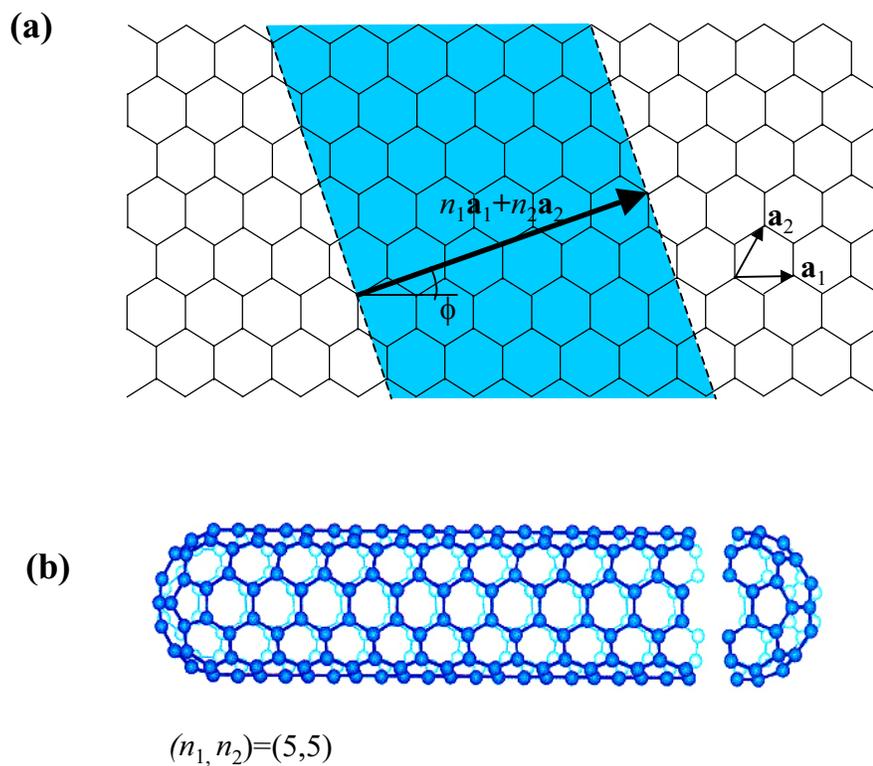
Figure 2.1 Forming a NT from a graphene sheet. **(a)** The graphene lattice and lattice vectors $\mathbf{a}_1$ and $\mathbf{a}_2$. A wrapping vector $n_1\mathbf{a}_1{+}n_2\mathbf{a}_2 = 4\mathbf{a}_1{+}2\mathbf{a}_2$ is shown. The shaded area of graphene will be rolled into a tube so that the wrapping vector encircles the waist of the NT. The chiral angle ϕ is measured between $\mathbf{a}_1$ and the wrapping vector. **(b)** A NT with wrapping vector $5\mathbf{a}_1{+}5\mathbf{a}_2$, $\phi = 30°$.

The geometry of an unstrained NT is described by a wrapping vector. The wrapping vector encircles the waist of a NT so that the tip of the vector meets its own tail. One possible wrapping vector is shown in Fig. 2.1. In this example, the shaded area of graphene will be rolled into the NT. The wrapping vector can be any $n_1\mathbf{a}_1 + n_2\mathbf{a}_2$ where n_1 and n_2 are integers and $\mathbf{a}_1$ and $\mathbf{a}_2$ are the unit vectors of the graphene lattice ($|\mathbf{a}_i| \approx 0.25$ nm). The angle between the wrapping vector and the lattice vector $\mathbf{a}_1$ is the chiral angle of a NT. Chrial angle ϕ can vary between 0° and 30° (any wrapping vector outside this range can be mapped onto 0° < ϕ < 30° by a symmetry transformation). In later sections we will see that the parameters n_1, n_2 and ϕ all play important roles in describing the electrical properties of NTs.

2.3 Tight binding calculation for graphene

To describe the electronic states of a NT we must first understand the electronic structure of graphene. The graphene lattice has unique electronic properties. Using the tight-binding approximation (Ashcroft & Mermin 1976) we will see that conduction and valence states in graphene only meet at two points in k-space and that dispersion around these special points is conical. In Section 2.5 we describe the electronic states of a NT by combining these properties of graphene with cylindrical boundary conditions.

Figure 2.2 shows the real space geometry of the graphene lattice. Each unit cell has two carbon atoms, labeled A and B. The bonds between carbon atoms form a hexagonal lattice, with each A atom connected to three B atoms and vice versa. The bonds are directed along the vectors $\boldsymbol{\rho}_1$, $\boldsymbol{\rho}_2$ and $\boldsymbol{\rho}_3$.

Each carbon atom has four valence electrons. Three of these electrons participate in the C-C sigma bonding. The fourth electron occupies a p_z orbital. The p_z states mix together forming delocalized electron states with a range of energies that
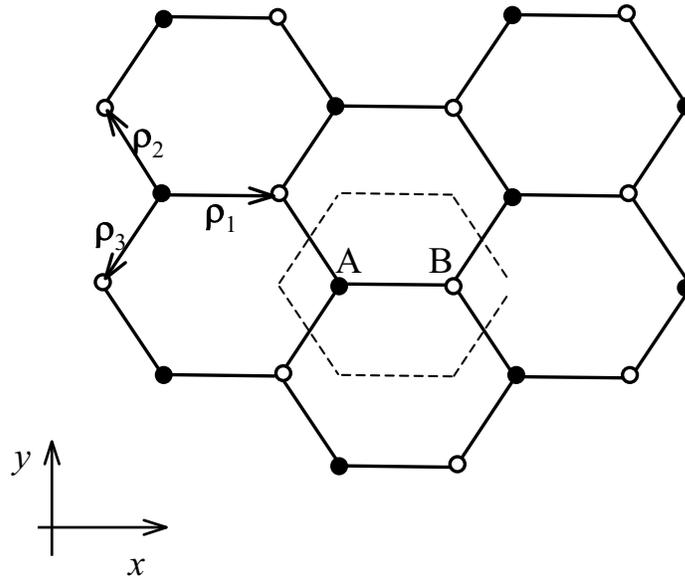
Figure 2.2 Geometry of the graphene lattice. The unit cell, indicated by a dashed line, contains two carbon atoms labelled A (black) and B (white). The three bond vectors are labeled ρ_1, ρ_2 and ρ_3. The x-axis is parallel to $\boldsymbol{\rho}_1$.

includes the Fermi energy. These states are responsible for the electrical conductivity of graphene.

To proceed with a tight-binding calculation we build linear combinations of p_z orbitals that satisfy the symmetry of the graphene lattice. An electron wave function in a periodic lattice must satisfy the Bloch condition.

$$\psi_{\mathbf{k}}(\mathbf{r}) = \exp(i\mathbf{k}\cdot\mathbf{r})u(\mathbf{r}),$$

where $u(\mathbf{r})$ has the periodicity of the crystal lattice (Ashcroft & Mermin 1976). In the case of graphene, the function $u(\mathbf{r})$ can be approximated using $X(\mathbf{r})$, the p_z atomic orbital of an isolated carbon atom. Positioning the function $X(\mathbf{r})$ at every lattice site gives

$$\psi_{\mathbf{k}}(\mathbf{r}) = \sum_A \exp(i\mathbf{k}\cdot\mathbf{R}_A)X(\mathbf{r}-\mathbf{R}_A) + \lambda\sum_B \exp(i\mathbf{k}\cdot\mathbf{R}_B)X(\mathbf{r}-\mathbf{R}_B), \qquad (2.1)$$

where $\mathbf{R}_A$ and $\mathbf{R}_B$ are the positions of A and B atoms. The phase difference between two atoms in the same unit cell is $\lambda e^{i\mathbf{k}\cdot\rho_1}$ (ρ_1 is the bond vector connecting the two atoms in the unit cell). Note that Eq. 2.1 satisfies Bloch's theorem, i.e. $\psi_{\mathbf{k}}$ can be written in the form $\exp(i\mathbf{k}\cdot\mathbf{r})u(\mathbf{r})$ where $u(\mathbf{r})$ has the crystal lattice periodicity.

Our goal is to find the eigenenergies E_k of the wavestates $\psi_{\mathbf{k}}$. To approximate $E_{\mathbf{k}} = \langle\psi_{\mathbf{k}}|H|\psi_{\mathbf{k}}\rangle$ we start with an expression for $\langle\psi_{\mathbf{k}}|H|\psi_{\mathbf{k}}\rangle$ that neglects the overlap integrals between the A atoms (each A atom is surrounded by B atoms):

$$E_{\mathbf{k}} = E_0 \pm \frac{1}{N}\int\left(\sum_A \exp(-i\mathbf{k}\cdot\mathbf{R}_A)X^*(\mathbf{r}-\mathbf{R}_A)\right)H\left(\lambda\sum_B \exp(-i\mathbf{k}\cdot\mathbf{R}_B)X(\mathbf{r}-\mathbf{R}_B)\right)d\mathbf{r}$$

$$(2.2)$$

where E_0 is the energy of the bare p_z orbital, N is the number of carbon atoms in the lattice and H is the Hamiltonian describing the lattice. Equation 2.2 is simplified further by removing the remaining non-nearest-neighbor terms:

$$E_{\mathbf{k}} = E_0 + \lambda \sum_i t_i \exp(-i\mathbf{k} \cdot \mathbf{\rho}_i), \qquad (2.3)$$

with

$$t_i = \int X^*(\mathbf{r} - \mathbf{R}_A) H X(\mathbf{r} - \mathbf{R}_{B,i}) d\mathbf{r}, \qquad (2.4)$$

where the index $i = 1, 2$ or 3 refers to three B atoms neighboring each A atom.

The last step in determining $E_{\mathbf{k}}$ is finding the phase factor λ. From variational principles λ is a complex number of norm unity ($|\lambda| = 1$) which makes Eq. 2.3 real valued (Wallace 1947). From Wallace's result we have

$$E_{\mathbf{k}} = E_0 \pm \left| \sum_i t_i \exp(-i\mathbf{k} \cdot \mathbf{\rho}_i) \right|, \qquad (2.5)$$

where the $\pm$ are associated with different values of λ.

There are two eigenvalues for every $\mathbf{k}$ in Eq. 2.5 due to the two possible values of λ at each point in k-space. For example, at $\mathbf{k} = 0$ the high energy state has $\lambda = 1$ while the low energy state has $\lambda = -1$. The two wavefunctions $\psi_{\mathbf{k}=0}^{\lambda=1}$ and $\psi_{\mathbf{k}=0}^{\lambda=-1}$ are shown schematically in Fig. 2.3. The phase of the wavefunction at each lattice site is designated by + or - signs. Just as in a diatomic molecule, the low-energy "bonding state" forms when neighboring atomic orbitals add constructively ($\lambda = 1$) while the high-energy "anti-bonding state" forms when neighboring orbitals add destructively ($\lambda = -1$).
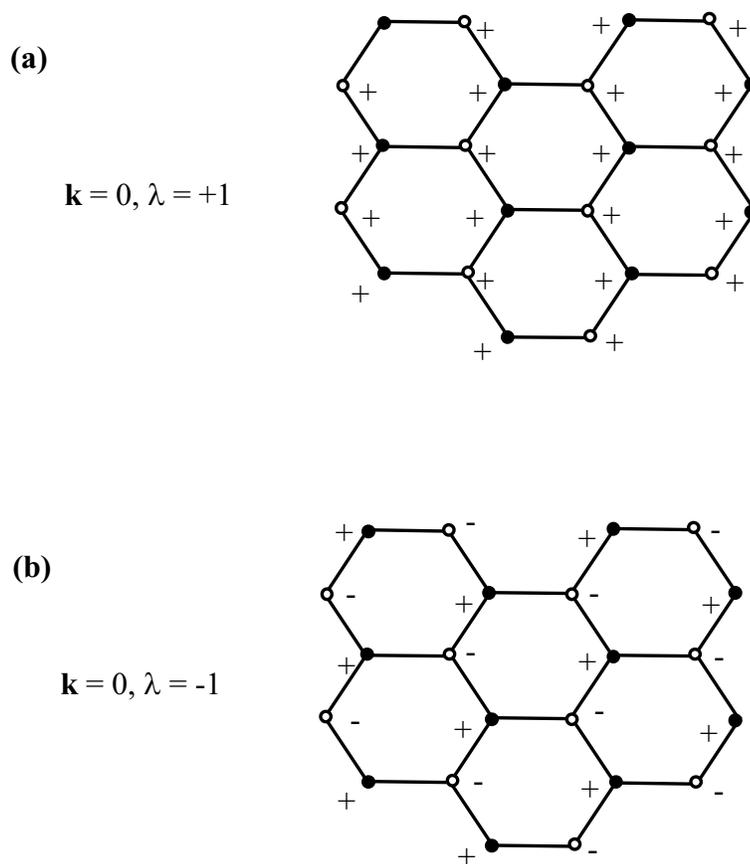
**Figure 2.3** Bonding and anti-bonding wavefunctions in graphene. The tightbinding wavefunction contains an orbital from each atom. The phase of each orbital is labelled either + or -. **(a)** When $\mathbf{k} = 0$, $\lambda = +1$ all orbitals have the same phase and add constructively to form a bonding state. **(b)** When $\mathbf{k} = 0$, $\lambda = -1$ neighboring wavefunctions have opposite phase and an anti-bonding state is formed.

The dispersion relation described by Eq. 2.5 is plotted in Fig. 2.4. Figure 2.4a shows the high energy ($E_{\mathbf{k}}>E_0$) and low energy ($E_{\mathbf{k}}<E_0$) states that make up the conduction and valence bands of graphene. From this plot we see that the conduction and valence bands meet at certain points in k-space. These special points, where conduction and valance states are degenerate, are called "K points". Figure 2.4b shows a contour plot of the energy of valence band states. The circular contours around the K points reflects the conical shape of the dispersion relation near the K points.

Electronic states near the Fermi level of graphene are located on dispersion cones. Therefore, the shape and position of these cones is critical for describing graphene (and NT) electronic properties. The two K points labeled $\mathbf{K}_1$ and $\mathbf{K}_2$ in Fig. 2.4b are positioned at $(k_x, k_y) = a^{-1}(0, \pm 4\pi/3)$ where $a = |\mathbf{a}_i| = 0.25$ nm. The slope of the cones is $(\sqrt{3}/2)t_0 a$ where $t_0 \approx 2.7$eV (White & Mintmire 1998). The slope of the cones determines the Fermi velocity of graphene, $v_F \approx 8 \times 10^5$ ms^{-1}.

2.4 Symmetries in graphene

An important feature of Fig. 2.4 is the vanishing energy diffence between conduction and valance states at special points in k-space (the "K points"). By considering the symmetries of graphene we can gain a deeper understanding of this K-point degeneracy. Symmetry arguments also show there are only two inequivalent K points in graphene, and that this pair of points ($\mathbf{K}_1$ and $\mathbf{K}_2$) must satisfy the relationship $\mathbf{K}_1 = -\mathbf{K}_2$.

To understand K-point degeneracy we consider states associated with the wavevector $\mathbf{K}_1 = (0, 4\pi/3)$. Using this wavevector we construct a pair of wavefunctions (using two different values of λ) which demonstrate the physical basis for this degeneracy. Figure 2.5 illustrates the wavefunctions $\psi_{\mathbf{K}_1}$ with $\lambda = e^{i2\pi/3}$ and $\lambda = e^{i4\pi/3}$. The phase of the wavefunction is indicated at each carbon atom. The wave functions
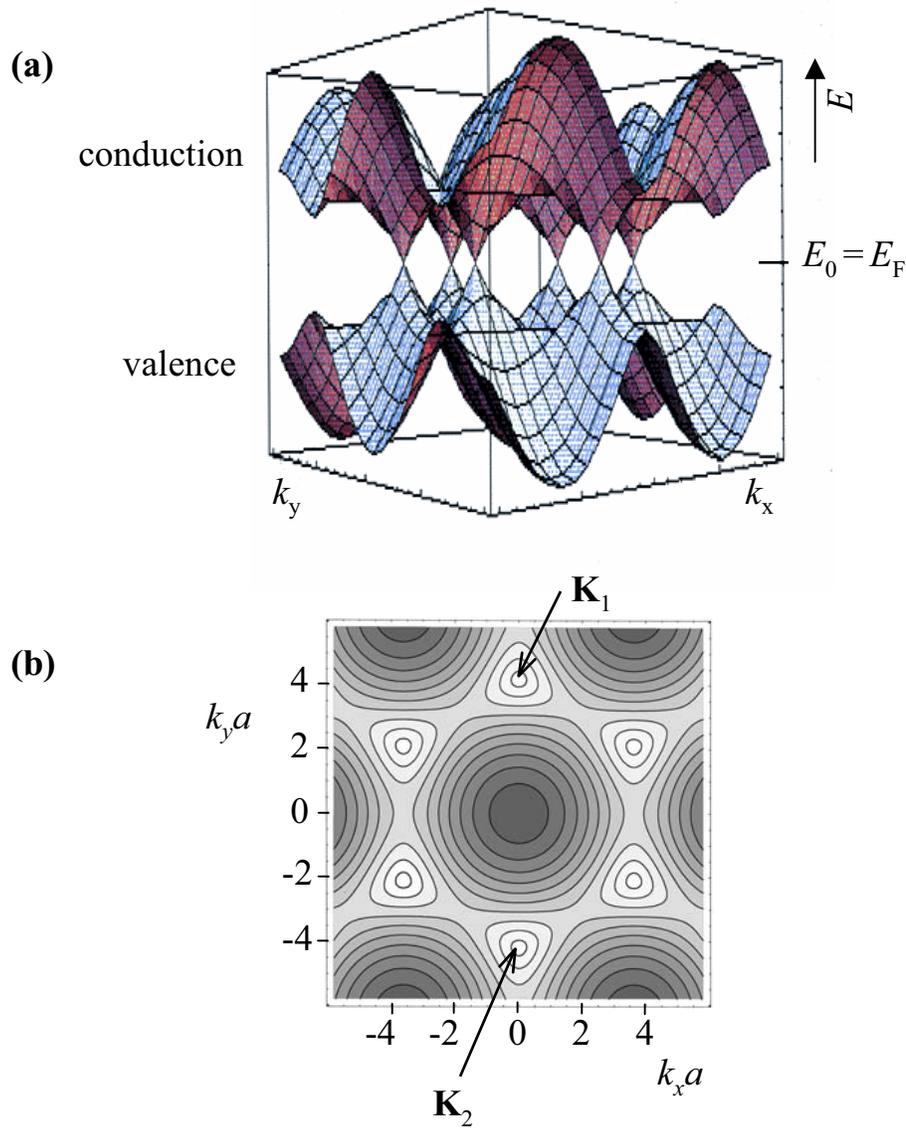
Figure 2.4 The dispersion relation of graphene. **(a)** The energy of valence and conduction states in graphene plotted as a function of wavevector **k**. The valence and conduction states meet at singular points in k-space called K points. Dispersion around these points is conical. **(b)** A contour plot of the valence state energies in (a). Lower energies are colored darker. The circular contours around six K points (colored white) can be seen. The hexagon formed by the six K points defines the graphene unit cell in k-space, beyond this unit cell the dispersion relation repeats itself. Arrows point to the two inequivalent K points, K_1 and K_2.

(a)

$\mathbf{K}_1 = (0, 4\pi/3)$
$\lambda = e^{i2\pi/3}$
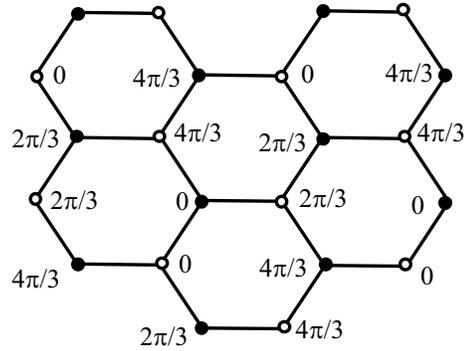
(b)

$\mathbf{K}_1 = (0, 4\pi/3)$
$\lambda = e^{i4\pi/3}$
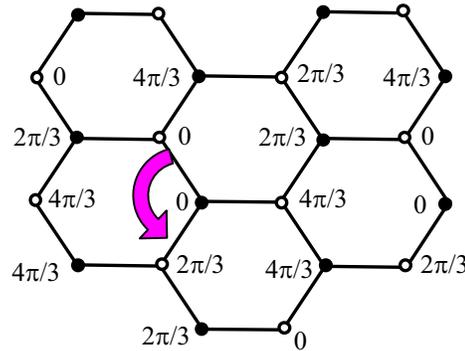
Figure 2.5 Degenerate wavefunctions associated with the $\mathbf{K}_1$ wavevector. The 'A' atoms are colored black and positioned at $\mathbf{R}_A$, the 'B' atoms are colored white. The phase of the wavefunction at the A atoms is $e^{\mathbf{K}_1 \cdot \mathbf{R}_A} = 0$, $e^{i2\pi/3}$ or $e^{i4\pi/3}$ as shown in (a) and (b). The phase of the wavefunction at the B atoms depends on λ. **(a)** The $\mathbf{K}_1$ wavefunction when $\lambda = e^{i2\pi/3}$. **(b)** The $\mathbf{K}_1$ wavefunction when $\lambda = e^{i4\pi/3}$. This wavefunction maps onto (a) by a 120° rotation, as indicated by the arrow.

map onto each other by a 120˚ rotation. Because the graphene lattice also has a 120˚ rotational symmetry the two wavefunctions must be degenerate. Valence and conduction states with $\mathbf{K}_1 = (0, 4\pi/3)$ are built from these degenerate $\lambda = e^{i2\pi/3}$ and $\lambda = e^{i4\pi/3}$ states. Therefore, valence and conduction states at the $\mathbf{K}_1$ point are degenerate.

There are two further symmetries of graphene which are important for our analysis. The first is between $\mathbf{k}$ and $-\mathbf{k}$ states. Unless there is a magnetic field (Section 2.9), forward and backward moving states have identical eigenenergies (by time reversal symmetry). If conduction and valence states meet at $\mathbf{K}_1$ they must also meet at $-\mathbf{K}_1$. Therefore, the degeneracy we found at the $\mathbf{K}_1$ point also occurs at $\mathbf{K}_2 = -\mathbf{K}_1$.[1]

Lastly, the translational symmetry of the graphene lattice means that k-states are equivalent if they can be connected by a reciprocal lattice vector. The unit reciprocal lattice vectors are $\mathbf{G}_1$ and $\mathbf{G}_2$ where $\mathbf{G}_i \cdot \mathbf{a}_j = 2\pi\delta_{ij}$. In Fig. 2.4b the $\mathbf{K}_1$ point can be mapped by reciprocal lattice vectors onto the lower left and lower right K points. Similarly, the $\mathbf{K}_2$ point is equivalent to the upper left and upper right K points. There are only two inequivalent K points in graphene; all electron states near the Fermi level of graphene have k-vectors close to either $\mathbf{K}_1$ or $\mathbf{K}_2$.

In the next section we examine the affect of rolling graphene into a cylinder, focusing on the electronic states near $\mathbf{K}_1 = -\mathbf{K}_2$.

2.5 *Quantization around a graphene cylinder*

In a cylinder such as a NT, the electron wave number perpendicular to the cylinder's axial direction, $k_\perp$, is quantized. This quantization, together with the properties of graphene, lead us to a description of NT electronic structure.

---

[1] We can construct a pair of degenerate wavefunctions for $\mathbf{K}_2$, just as we did for $\mathbf{K}_1$. These $\psi_{\mathbf{K}_2}$ wavefunctions will be mirror images of the $\psi_{\mathbf{K}_1}$ wavefunctions shown in Figs. 2.5a and b.

Because nanotube diameters are small (~ 1nm), there is a significant spacing between quantized values of $k_\perp$ (Fig. 2.6). In the direction parallel to the NT axis, however, electrons are free to move over much larger distances and the electron wavenumber in the parallel direction, $k_\parallel$, is effectively continuous. The continuum of $k_\parallel$ states in each $k_\perp$ wrapping mode are called one-dimensional (1-D) subbands.

The quantized $k_\perp$ are determined by the boundary condition

$$\pi D k_\perp = 2\pi j, \tag{2.5}$$

where j is an integer and D is the NT diameter. The parallel lines in Fig 2.6b represent the allowed **k** states in a NT; each line is a different 1-D subband. The interline separation in Fig 2.6b translates into a large energy spacing between 1-D subbands. The only electron states with $E_\mathbf{k}$ close to E_F are in 1-D subbands with allowed **k** close to $\mathbf{K}_1$ or $\mathbf{K}_2$.

The exact alignment between allowed **k** values and the K points of graphene is critical in determining the electrical properties of a NT. To see how different types of alignment come about, we consider NTs with wrapping indices of the form $(n_1,0)$. In lattice vector units such tubes have circumference n_1, allowed $k_\perp = 2\pi j/n_1$ and $\mathbf{K}_1$ is positioned at $(k_\parallel, \ k_\perp) = (0, \ 4\pi/3)$.

When n_1 is a multiple of 3 ($n_1 = 3q$ where q is an integer) there is an allowed $k_\perp$ that coincides with $\mathbf{K}_1$. Setting $j = 2q$

$$k_\perp = \frac{2\pi j}{n_1} = \frac{4\pi q}{3q} = \frac{4\pi}{3}.$$

The intersection of a 1-D subband with the $\mathbf{K}_1$ point is illustrated in Fig. 2.7a.

Two cases exist when n_1 is not a multiple of 3. First, if $n_1 = 3q+1$ we find the closest $k_\perp$ to $\mathbf{K}_1$ by setting $j = 2q+1$:

(a)

(b)

(c)
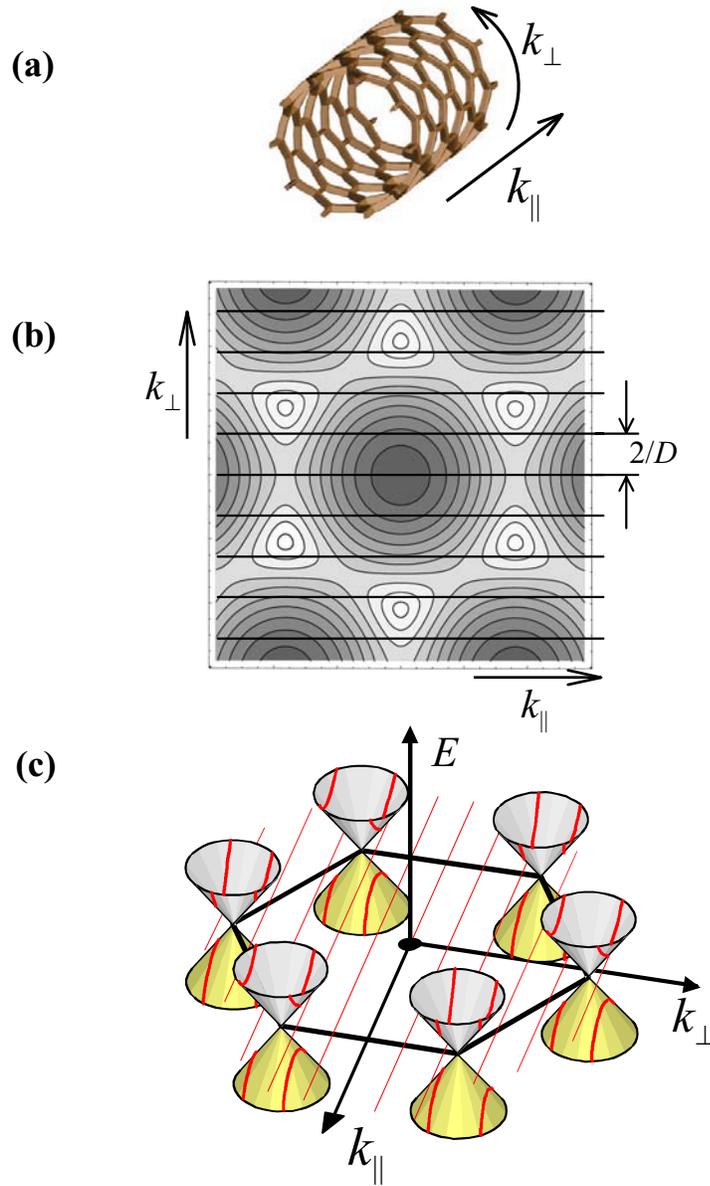
Figure 2.6 Quantization of wave states around a graphene cylinder. **(a)** The parallel and perpendicular axes of a NT. **(b)** Contour plot of graphene valence states for a NT with chiral angle $\phi = 0$. The parallel lines spaced $2/D$ indicate the **k** vectors that are allowed by the cylindrical boundary condition. Each line is a 1-D subband. **(c)** Electron states near E_F are defined by the intersection of allowed **k** with the dispersion cones at the K points.
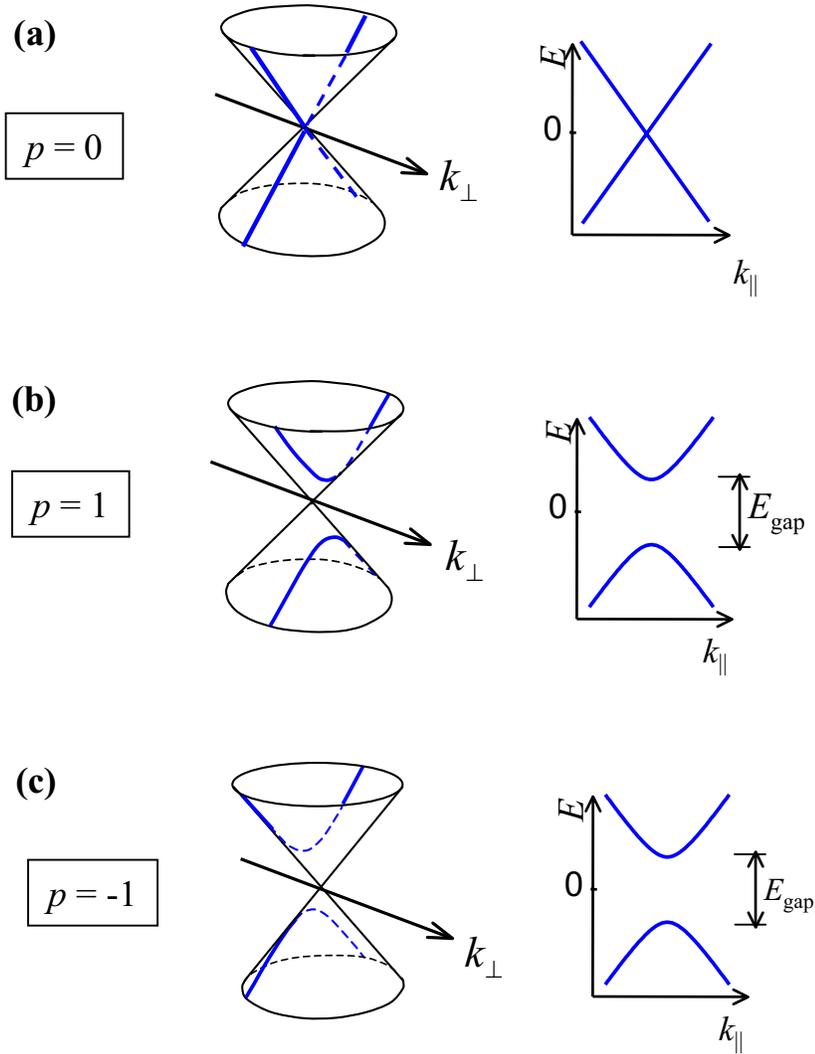
Figure 2.7 Different alignment between the dispersion cone at $\mathbf{K}_1$ and allowed $\mathbf{k}$.
(a) When $p = -1$ the misalignment between $\mathbf{K}_1$ and the nearest 1-D subband is -2/3D. The bandgap of the subband is $E_{gap} = 2hv_F(2/3D)$. **(b)** When $p = 0$ a subband intercepts the K point. The subband is metallic. **(c)** When $p = 1$ the misaligment between $\mathbf{K}_1$ and the nearest 1-D subband is +2/3D. The subband has $E_{gap} = 2hv_F(2/3D)$.

$$k_\perp = \frac{2\pi j}{n_1} = \frac{2\pi(2q+1)}{(3q+1)} = \frac{4\pi}{3} + \frac{2}{3}\frac{\pi}{3q+1} = \frac{4\pi}{3} + \frac{2}{3D}.$$

Similarly, if $n_1 = 3q$-1 the closest allowed $k_\perp$ corresponds to $j = 2q$-1:

$$k_\perp = \frac{2\pi j}{n_1} = \frac{2\pi(2q-1)}{(3q-1)} = \frac{4\pi}{3} - \frac{2}{3}\frac{\pi}{3q-1} = \frac{4\pi}{3} - \frac{2}{3D}.$$

The two cases where 1-D subbands do not intersect K_1 are shown in Fig. 2.7b and c.

All NTs fall into one of the three families illustrated in Fig. 2.7 (Dresselhaus et al. 2001). Given a wrapping index (n_1, n_2) we calculate $n_1 - n_2 = 3q + p$ where q is an integer and p is either -1, 0 or 1. The index p defines the type of alignment between allowed $\mathbf{k}$ and the K points as follows (the symmetry between $+\mathbf{k}$ and $-\mathbf{k}$ states ensures that the subbands near $\mathbf{K}_1$ and $\mathbf{K}_2$ are degenerate):

i) $p = 0$: a line of allowed k intercepts $\mathbf{K}_1$ (Fig. 2.7a). Both 1-D subbands are metallic[2].

ii) $p = 1$: a line of allowed k misses $\mathbf{K}_1$ by $\Delta k = +2/3D$, (Fig. 2.7b). The 1-D subbands associated with both K points have bandgaps $E_{gap} = 2\hbar v_F(2/3D)$.

iii) $p = -1$: a line of allowed k misses $\mathbf{K}_1$ by $\Delta k = -2/3D$, (Fig. 2.7c). The 1-D subbands associated with both K points have bandgaps $E_{gap} = 2\hbar v_F(2/3D)$.

The $p = \pm 1$ type NTs have large bandgaps ($E_{gap} \sim 0.7$eV/D[nm]), a feature which clearly distinguishes them from $p = 0$ type NTs. The physical differences

---

[2] Nantubes with $p = 0$ can develop small bandgaps if Δk is modified by other perturbations such as strain (see Section 2.8).

between $p = 1$ and $p = -1$ type NTs are less obvious, but will become clear as we turn to the electromechanical properties of NTs.

2.6 K points shift due to strain

In this section we consider what happens to the dispersion cones at $\mathbf{K}_1$ and $\mathbf{K}_2$ when graphene is stretched (Heyd et al. 1997; Yang et al. 1999; Yang & Han 2000). We will see that conduction and valence states still meet at single points in k-space, but the position of these points is shifted.

For unstrained graphene the values of overlap integrals t_1, t_2 and t_3 (Eq. 2.3) were identical. When the lattice is stretched, however, the distance between neighboring carbon atoms will change and the overlap integral will become unequal. As the values of t_i become unequal the positions of the K points change. We consider the special case that graphene is stretched along the $\boldsymbol{\rho}_1$ direction, which we define as the x-direction. The strained bond vectors are given by

$$\boldsymbol{\rho}_1 = d_{C-C}(1+\sigma,0) \tag{2.6a}$$

$$\boldsymbol{\rho}_2 = d_{C-C}(-\frac{1}{2}(1+\sigma),\frac{\sqrt{3}}{2}(1-\sigma\upsilon)) \tag{2.6b}$$

$$\boldsymbol{\rho}_3 = d_{C-C}(-\frac{1}{2}(1+\sigma),\frac{-\sqrt{3}}{2}(1-\sigma\upsilon)) \tag{2.6c}$$

where d_{C-C} is the unstrained C-C bond length and strain σ is the fractional change of length along the strain axis. Components of $\boldsymbol{\rho}_i$ perpendicular to the strain axis are compressed by $(1- \sigma\upsilon)$ where υ is the Poisson ratio of the material.

We are interested in dispersion around the K points as we change σ. We concentrate on a slice of the dispersion relation along the line $k_x = 0$. This line

intercepts $\mathbf{K}_1$ and $\mathbf{K}_2$ when $\sigma = 0$ (as shown in Fig. 2.8). Using Eq. 2.5 with $E_0 = 0$ and setting the lattice vectors to length unity (equivalent to setting $d_{C\text{-}C} = 1/\sqrt{3}$), we find

$$E(k_y)\big|_{k_x=0} = \pm \left| t_1 + t_2 \exp(ik_y(1-\sigma\upsilon)/2) + t_3 \exp(-ik_y(1-\sigma\upsilon)/2) \right|,$$

which can be simplified using $t_2 = t_3$, to give

$$E(k_y)\big|_{k_x=0} = \pm 2t_2 \left| \cos\left(\frac{k_y(1-\sigma\upsilon)}{2} \right) + \frac{t_1}{2t_2} \right|. \tag{2.7}$$

Equation 2.7 is plotted in Fig. 2.8b at $\sigma = 0$ and $\sigma = 0.2$. When $\sigma = 0$ ($t_1 = t_2$) the K points are located at $K_{1,y} = -K_{2,y}$ where we have $E(K_{i,y}) = 0$. When $\sigma > 0$ there remains a unique pair of values $K_{1,y} = -K_{2,y}$ for which $E(K_{i,y}) = 0$. The special property of graphene, namely zero bandgap at singular K points, survives when the lattice is strained (Kane & Mele 1997).

To quantify the shift of the K points with respect to σ we use the approximation $t_i \propto 1/|\boldsymbol{\rho}_i|^2$ (Yang & Han 2000). From Eqs. 2.6a and b we have, for small σ,

$$\frac{t_1}{t_2} = 1 - \frac{3}{2}(1+\upsilon)\sigma. \tag{2.8}$$

Combining Eqs. 2.7 and 2.8, and linearizing the function $\cos(k_y(1-\sigma v)/2)$ around $k_y(1-\sigma v)/2 = 2\pi/3$, we find

$$K_{1,y}(\sigma) = -K_{2,y}(\sigma) = \frac{4\pi}{3}(1+\sigma v) - \sqrt{3}(1+\upsilon)\sigma. \tag{2.9}$$

Equation 2.9 describes the strain-induced shift of the K points when strain is parallel to one of the bond vectors. The shift is significant even at small strain, and is critical

(a)

(b)
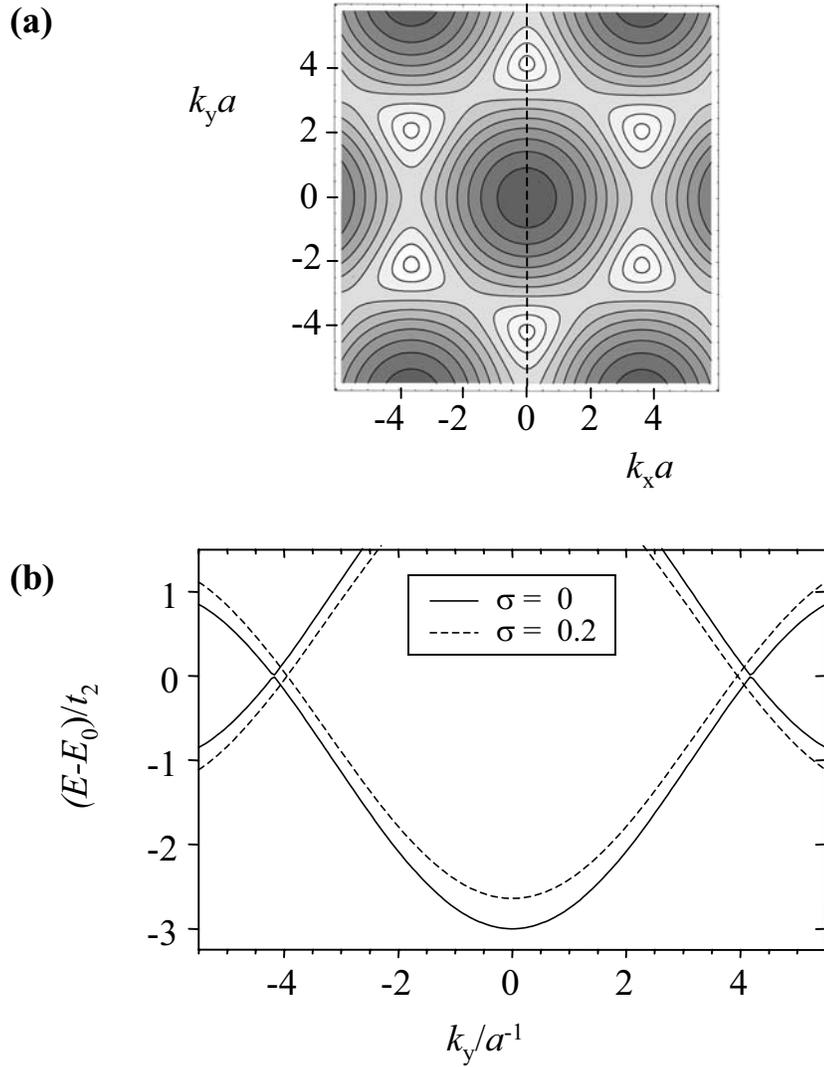
Figure 2.8 Changes in graphene bandstructure when strain is applied in the *x*-direction. **(a)** A contour plot of valence states in unstrained graphene. The vertical dashed line shows the slice $k_x = 0$ which passes through both $\mathbf{K}_1$ and $\mathbf{K}_2$. **(b)** Energy of valence and conduction states along the line $k_x = 0$ when strain $\sigma = 0$ and 0.2. The K points (intersection of valence and conduction states) move toward smaller k_y as strain is increased.

for understanding the electromechanical behavior of NTs, as discussed in the next section.

2.7 Effect of strain on nanotube bandgap

Nanotube bandgaps depend on the alignment of allowed **k** states with the dispersion cones at $\mathbf{K}_1$ and $\mathbf{K}_2$ (Fig. 2.7). We found in Section 2.6 that $\mathbf{K}_i$ move when the graphene lattice is strained, therefore, we expect NT bandgaps to be sensitive to strain. We calculate this strain sensitivity below and show that it varies dramatically between different types of NTs. Depending on the chiral angle ϕ and the index $p = -1$, 0 or 1, the bandgap of a NT can increase, decrease or remain unchanged with strain (Heyd et al. 1997; Yang et al. 1999; Yang & Han 2000).

We begin by considering a NT of type $p = 0$, with chiral angle $\phi = 0$ as shown in Fig. 2.9. When the NT is unstrained there is no misalignment between $\mathbf{K}_i$ and the nearest allowed **k** (Fig 2.9a). When the NT is strained, however, both $\mathbf{K}_i$ and the allowed **k** shift. The shift of $\mathbf{K}_i$ due to axial strain is given by Eq. 2.9 (the axis of the NT corresponds to the $\boldsymbol{\rho}_1$ direction since $\phi = 0$). The quantized $k_\perp$ values change due to the changing diameter of the NT. The diameter shrinks by a factor $(1-\sigma v)$, and the $k_\perp$ nearest $\mathbf{K}_i$ become $\pm (4\pi/3)(1-\sigma v)^{-1}$. To first order in σ, the misalignment between $\mathbf{K}_1$ and the nearest allowed **k** is given by

$$\Delta k(\sigma) = \frac{1}{a}\sqrt{3}(1+\upsilon)\sigma,$$

where a is the unstrained lattice constant. A similar shift occurs near $\mathbf{K}_2$ and the subbands remain degenerate. From the slope of the dispersion cones around the K points, $(\sqrt{3}/2)t_0 a$, we have
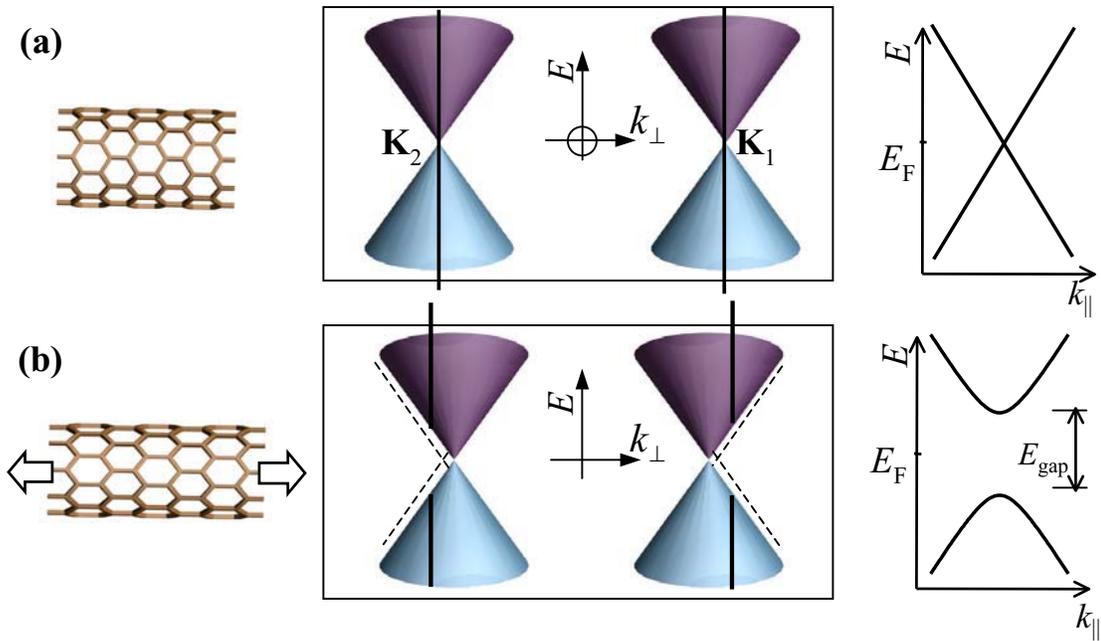
Figure 2.9 Stretching a $p = 0$ NT. The quantized $k_\perp$ values are represented by vertical lines intercepting the dispersion cones at $\mathbf{K}_1$ and $\mathbf{K}_2$. **(a)** Allowed $\mathbf{k}$ intercept the K points and the 1D subbands near $\mathbf{K}_1$ and $\mathbf{K}_2$ have zero bandgap. **(b)** Both the K points and the quantized $k_\perp$ values shift when the NT is strained. Bandgaps open in the 1D subbands. Subbands remain degenerate due to $\mathbf{k}$, $-\mathbf{k}$ symmetry.

$$E_{gap}(\sigma) = 2\frac{\sqrt{3}}{2}t_0 a \cdot \left|\Delta k(\sigma)\right| = 3t_0(1+\upsilon)\sigma . \tag{2.10}$$

Axial strain opens a bandgap in $\phi = 0$, $p = 0$ type NTs. The change in bandgap is independent of diameter.

Next we consider NTs of type $p = 1$ and -1, also with chiral angle $\phi = 0$. The unstrained p = 1 tube has $\Delta k = 2/3D$, while the unstrained p = -1 tube has $\Delta k = -2/3D$ (see Fig. 2.7b,c). As in the $p = 0$ case, axial strain shifts the relative position of $\mathbf{K}_1$ and the nearest allowed $\mathbf{k}$, and we find

$$\Delta k(\sigma) = \frac{2}{3D} + \frac{1}{a}\sqrt{3}(1+\upsilon)\sigma \qquad \text{when p = 1,}$$

$$\Delta k(\sigma) = -\frac{2}{3D} + \frac{1}{a}\sqrt{3}(1+\upsilon)\sigma \qquad \text{when p = -1.}$$

Since $E_{gap} \propto |\Delta k|$ we find that the bandgap of a $p = 1$ type NT increases with strain, while the bandgap of the $p = -1$ type NTs decreases with strain.

The examples given above are for NTs with chiral angle $\phi = 0$. Nanotube chirality affects the angle between $d\mathbf{K}_i/d\sigma$ and the lines of allowed $\mathbf{k}$. For example, in the $\phi = 0$ cases above, axial strain causes $\mathbf{K}_i$ to move perpendicular to the lines of allowed $\mathbf{k}$. When $\phi = 30°$ the motion of the K points is parallel to the lines of allowed $\mathbf{k}$ and axial strain does not affect E_{gap}. The following expression summarizes the full range of electromechanical behavior in NTs (Yang & Han 2000)

$$\frac{dE_{gap}}{d\sigma} = \pm 3t_0(1+\upsilon)\cos 3\phi , \tag{2.11}$$

Where + applies to $p = 0$ and 1 type NTs and $-$ applies to $p = -1$ type NTs.

The maximum change in bandgap with respect to strain, assuming $t_0 \approx 2.7\text{eV}$ and $\upsilon \approx 0.2$, is approximately 100 meV per 1% strain. This value is similar in magnitude to $\left| dE_{\text{gap}} / d\sigma \right|$ of typical bulk semiconductors. Unlike bulk semiconductors, however, NTs can have zero bandgap at zero strain ($p = 0$) and $dE_{\text{gap}} / d\sigma$ can be either positive or negative in semiconducting NTs ($p = \pm 1$). These predictions are tested experimentally in Chapter 4.

2.8 Perturbations that modify nanotube bandgap

We have seen that axial strain shifts the dispersion cones in a NT. Other perturbations, such as curvature (Kane & Mele 1997), twist (Yang & Han 2000), and inner-outer shell interactions (Kwon & Tomanek 1998), also shift the dispersion cones, thereby changing NT bandgap. Curvature and inter-shell interactions are intrinsic properties of a NT, while strain and twist can be built into a NT when it adheres to a surface. All of these factors affect the exact bandstructure of a NT.

In $p = 0$ type NTs perturbations will open small bandgaps. For example, the curvature effect is expected to open a bandgap of ~ 40 meV in a $p = 0$ NT with $D = 1$ nm and $\phi = 0$ (Kane & Mele 1997)[3]. Small bandgap NTs are often observed in transport experiments (Zhou et al. 2000). The perturbations responsible for these small bandgaps are not always clear, especially if the NT is stuck to a surface or has multiple walls.

There is also experimental evidence of perturbation-induced shifts of the K points in semiconducting NTs (type $p = 1$ and -1). The 1-D subbands on either side of $\mathbf{K}_1$ are shown in Fig. 2.10 for both types of semiconducting NT. With no perturbation the subband closest to $\mathbf{K}_1$ is expected to have an energy gap $2\hbar v_{\text{F}}(2/3D)$, while the

---

[3] The curvature bandgap scales as $1/D^2$ (Kane and Mele 1997) and is largest in NTs with small chiral angle.
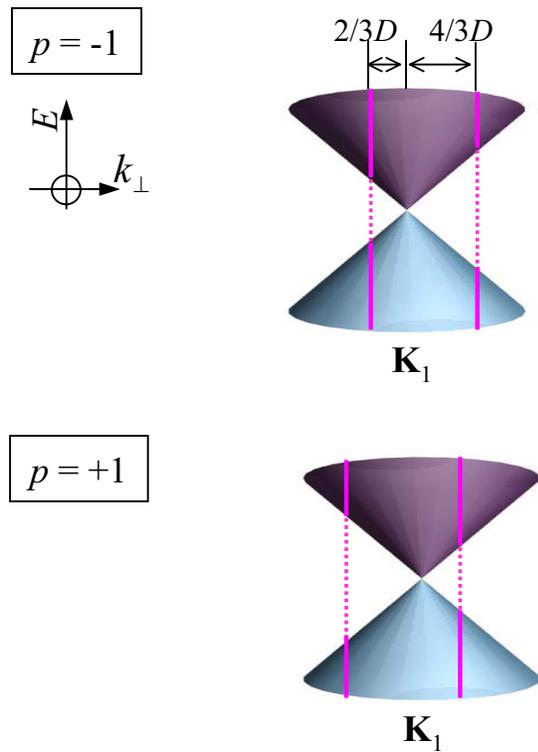
Figure 2.10 Measuring the position of the $\mathbf{K}_1$ point relative to the nearest and next-nearest allowed $k_\perp$. The quantized $k_\perp$ values are represented by vertical lines intercepting the dispersion cones. Without perturbations, the subband nearest $\mathbf{K}_1$ has half the bandgap of the next-nearest subband. Curvature induced strain moves the $\mathbf{K}_1$ point to the right. If $p = -1$, this curvature effect causes the large bandgap to decrease and the small bandgap to increase. If $p = +1$, curvature has the opposite effect on the bandgaps.

next-nearest subband is expected to have twice the bandgap, $2\hbar v_F$ $(4/3D)$. If the $\mathbf{K}_1$ point shifts, the ratio between these two bandgaps will be changed. A range of different bandgap ratios have been measured in photoluminescence experiments on semiconducting NTs (Bachilo et al. 2002). The spread in measured ratios was most dramatic in small diameter NTs (diameter can be measured independently by Raman spectroscopy). In some NTs the large bandgap was larger than expected (and the small bandgap smaller). In other cases, the opposite change in ratio was observed. The effect is well described by curvature-induced strain. This type of strain is predicted to move the $\mathbf{K}_1$ point to the right in Fig. 2.10. The strain will increase the larger bandgap and decrease the smaller bandgap in $p = 1$ type NTs, while the change in ratio is reversed for $p = -1$ type NTs. Because strain-induced bandgap changes are sensitive to chirality, Bachilo et al. were able to assign chiral angles to the small diameter NTs in their experiment.

None of the perturbations discussed above break the degeneracy between the $\mathbf{K}_1$ and $\mathbf{K}_2$ subbands. Regardless of the perturbation, $\mathbf{K}_1 = -\mathbf{K}_2$, and the quantization condition allows both $k_\perp$ and $-k_\perp$. Therefore, the 1-D subbands still come in degenerate pairs, even in strained NTs.

2.9 Effect of axial magnetic field

When an axial magnetic field is applied to a NT, the wrapping modes (the allowed $k_\perp$) are modified by an Aharonov-Bohm (A-B) phase (Ajiki & Ando 1993; Lu 1995). The A-B phase affects electron states differently depending on which direction the electron orbits a magnetic flux. As in previous sections, changes in NT bandgap can be calculated by considering the alignment between allowed $k_\perp$ and the K points. Unlike previous sections, however, subband degeneracy can be broken.

The boundary condition for electron wave states encircling a NT in the presence of an axial magnetic field $B_\parallel$ is

$$\pi D k_\perp + 2\pi \frac{\Phi}{\Phi_0} = 2\pi j , \qquad (2.12)$$

where $\Phi = B_\parallel \pi D^2/4$ is the flux threading the NT and $\Phi_0 = h/e$ is the flux quantum. The second term in Eq. 2.12 is the Aharonov-Bohm phase acquired by electrons as they encircle a magnetic flux. The set of allowed $k_\perp$ values shifts by an amount $(2/D)(\Phi/\Phi_0)$ as illustrated in Fig. 2.11. In this example, Δk is initially non-zero and the bandgap of the $\mathbf{K}_1$ subband, $E_{gap}^{K_1}$, decreases with $B_\parallel$, while the bandgap of the $\mathbf{K}_2$ subband, $E_{gap}^{K_2}$, increases with B. The changes in bandgap are given by

$$\frac{dE_{gap}^{K2}}{dB} = -\frac{dE_{gap}^{K1}}{dB} = 2\hbar v_F \frac{dk_\perp}{dB} = 2\frac{ev_F D}{4} . \qquad (2.13)$$

For a NT with $D = 1$nm the magnitude of this bandgap change is ~ 0.4 meV/T.

Equation 2.13 leads us to an interesting connection between the quantum mechanical description of the NT wrapping modes and a semiclassical picture of electrons orbiting a NT. The quantity $ev_F D/4$ is the magnetic moment of an electron traveling in a loop of diameter D with velocity v_F. Changes in the energy of electron states can be described by the interaction of this orbital magnetic moment $\mu_{orb} = ev_F D/4$ with an axial magnetic field. This semiclassical treatment is discussed in more detail in Chapter 5.

We see that axial magnetic fields are predicted to cause significant changes in NT electronic structure. Electron states are shifted in energy due to orbital motion and the degeneracy between the $\mathbf{K}_1$ and $\mathbf{K}_2$ subbands is broken if Δk is initially non-zero. These predictions are experimentally tested in Chapter 5.
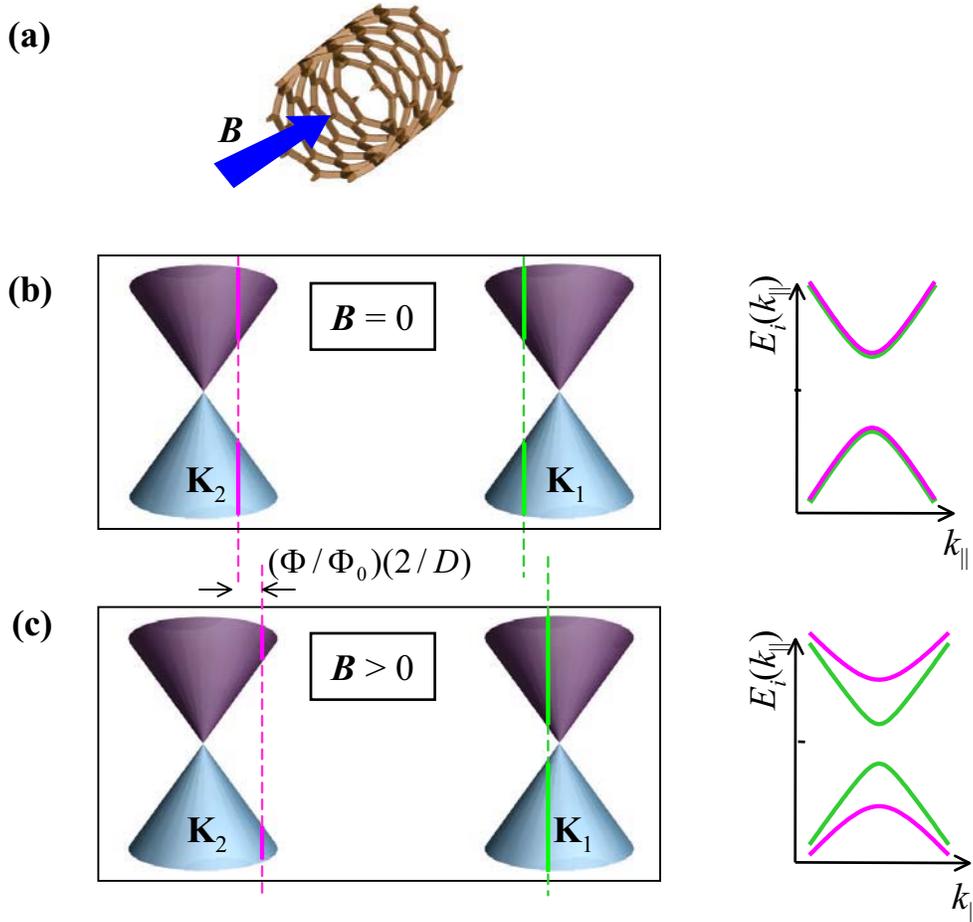
Figure 2.11 Changing bandgap due to axial magnetic field. **(a)** Applied magnetic field B along the axis of a NT. **(b)** Quantized $k_\perp$ values are represented by vertical lines intercepting the dispersion cones at $\mathbf{K}_1$ and $\mathbf{K}_2$. When $B = 0$ the both subbands have the same non-zero bandgap. **(c)** When $B > 0$ the allowed $k_\perp$ values shifted to the right an amount $(\Phi/\Phi_0)(2/D)$ due to the Aharonov-Bohm phase. One bandgap becomes smaller, the other becomes larger. The degeneracy between subbands is broken.

2.10 Conclusions

There are important common elements in the description of electromechanical and magnetic effects in NTs. Both effects can be described by relative shifts between the allowed **k** states and the K points of a NT. From this unified theoretical framework the electromechanical and magnetic properties of NTs are relatively easy to describe. The theory predicts a rich variety of electromechanical effects and a strong coupling between axial magnetic field and NT electronic states. These predictions motivate the experiments described in Chapters 4 and 5.

CHAPTER 3

MECHANICAL PROPERTIES OF NANOTUBES

3.1 Introduction

Carbon nanotubes (NTs) are cylinders of covalently bonded carbon atoms. The mechanical properties of NTs reflect the tremendous strength of this bonding network. Pioneering experiments have shown that NTs can accommodate very large strains (Walters et al. 1999; Yu et al. 2000) and have an extremely high Young's modulus (for a review see Salvetat et al. 1999). Because of their great strength, tiny dimensions and high aspect ratio, NTs are promising as reinforcing fibers in composite materials (Calvert 1999), nanoscale probes (Dai et al. 1996) and nanomechanical resonators (Craighead 2000, Sazonova et al. 2004). With recent observations of strong coupling between mechanical deformation and electrical behavior (Tombler et al. 2000), NTs may also be important elements in nano-electromechanical systems.

In this chapter we describe the use of an atomic force microscope (AFM) to study the mechanics of individual NTs. We measure the relationship between strain (fractional change in length) and tension in NTs with a range of diameters. We also demonstrate a new level of control in constructing NT structures by building tension into suspended NTs. The techniques developed in this chapter are critical for electromechanical studies presented in Chapter 4.

3.2 Previous Work

It is challenging to measure the mechanical properties of nano-structures. High resolution imaging must be combined with sensitive measurements of mechanical

forces. Two experimental techniques have played a critical role in exploring NT mechanics, atomic force microscopy (AFM) and electron microscopy.

Early AFM work on NT mechanical properties measured the bending rigidity of large diameter multi-walled nanotubes (MWNTs) and NT ropes (Wong 1997, Salvetat 1999). These experiments made use of small aspect ratio suspended NT structures, in which bending forces were larger than tensile forces. In later work, individual small diameter NTs (D~1-2nm) were suspended over long lengths (~ 500 nm). The suspended NTs were fixed at both ends, allowing AFM measurements of tensile forces (Tombler et al. 2000; Kim et al. 2002). Further work remains to be done since Tombler and Kim each present data from only a single device.

Electron microscopy techniques have complimented AFM studies. Inside a scanning electron microscope (SEM), Yu attached MWNTs (D~30nm) to spring-like cantilevers and stretched the fibers while monitoring tensile forces (Yu et al. 2000). In other work, using a transmission electron microscope (TEM), it was shown that the inner and outer shells of a MWNT slide against each other with very little friction (Cumings & Zettl 2000). Other SEM/TEM experiments have quantified NT bending rigidity by imaging vibrations (Treacy et al. 1996; Krishnan et al. 1998; Poncharal et al. 1999).

3.3 Device Fabrication

The samples studied in this chapter consist of individual NTs suspended above trenches made in Silicon dioxide (Fig. 3.1). In most cases our devices also have electrical contacts which are used in complimentary experiments (see Chapters 4 and 5). There are three major fabrication steps, 1) Growing NTs, 2) Fabricating electrodes, 3) Removing oxide from beneath the NTs. The steps are outlined below.

Nanotubes are grown on Si/SiO_2 substrates (500nm oxide layer) using the CVD process (Kong et al. 1998). First, Fe/Alumina catalyst particles are deposited at lithographically defined sites on the substrate. NTs grow from these catalyst particles when exposed to a flow of methane gas at 900ºC. We find NTs with diameters $1 – 10$ nm and lengths of several microns growing from the catalyst sites.

Gold electrodes (50 nm Au with 5 nm Cr adhesion layer) are aligned close to the catalyst sites using photolithography (Rosenblatt et al. 2002). The gap between each pair of electrodes is $\sim 1 – 2$ μm. We identify devices in which the electrodes are connected by one or more NTs by probing electrical conductivity. The diameter of the NTs in conducting devices is then measured by AFM.

In the final fabrication step we release NTs from the SiO_2 substrate by etching the oxide with a solution of buffered hydrofluoric acid BHF (3 minutes in 6:1 BHF, etch rate 80 nm/min) (Walters et al. 1999; Nygard & Cobden 2001). There are two options for defining the oxide area that will be etched. In the 'self-aligned' method the gold electrodes protect the oxide beneath them, while the exposed oxide between the electrodes is etched. The NT is left hanging between the electrodes (Fig. 3.1c). In the 'lithography' method, e-beam lithography is used to define a strip of exposed oxide centered between the electrodes. Using the lithography method, only a short section of the NT lying between the electrodes is suspended (Fig. 3.1d).
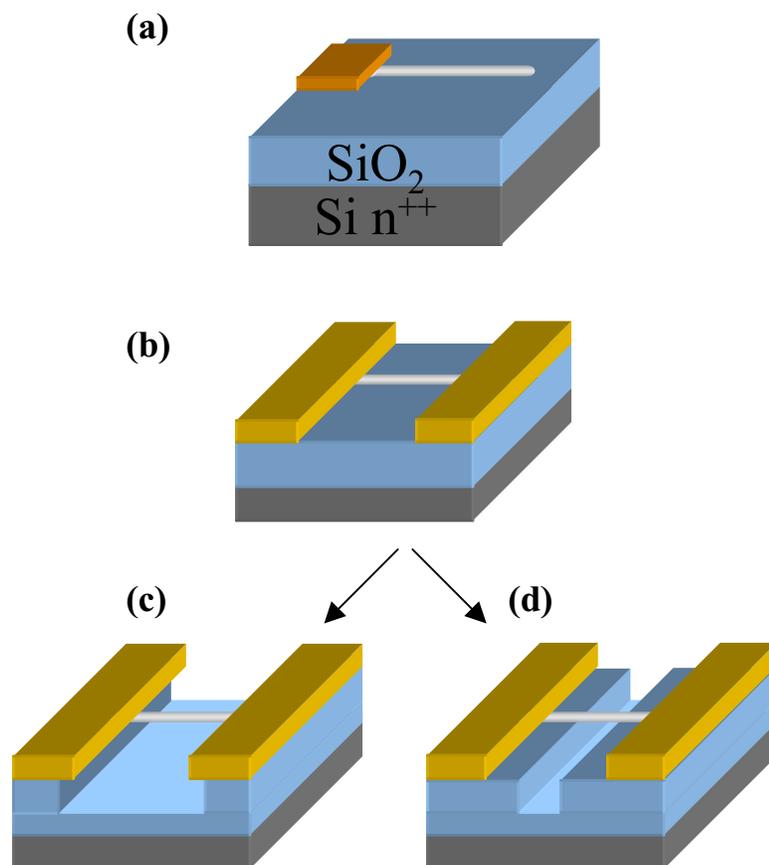
Figure 3.1 Fabrication steps for suspended NT devices. **(a)** Catalyst is patterned on SiO_2/Si wafer. Nanotubes grow from catalyst. **(b)** Electrodes are defined by photolithography. **(c)** The "self-aligned" etching method. All exposed SiO_2 is etched. **(d)** The "lithography" etching method. A narrow trench between the electrodes is etched into the SiO_2.

After the wet oxide-etching procedure, care must be taken in drying the devices. Surface tension forces during drying tend to collapse suspended structures. To avoid the problematic liquid/gas phase transition we have used critical point drying. This process utilizes the high pressure, high temperature state of CO_2 where there is no phase transition between liquid and gas.

Following the drying procedure, a final cleaning step is used. Residue left behind by early steps is effectively removed by heating chips to 400ºC in an Argon atmosphere. A completed device is shown in Fig. 3.2.

3.4 AFM Techniques

Our experiments were carried out in a commercial AFM system (Dimension 3100, Digital Instruments). An important component of the instrument is the laser used to detect bending of the AFM cantilever. We use a low noise laser, available by special request from Digital Instruments technical support, designed to suppress interference effects that can occur as the partially reflective cantilever travels up and down above a reflective substrate.

Two calibration steps are necessary for AFM-based mechanical measurements. The output voltage of the laser detector (which is proportional to the bending angle of the cantilever) must be calibrated to measure the displacement of the cantilever δ_{DC}. Figure 3.3b shows a typical calibration curve. The photodetector voltage increases as the piezo presses the tip against an oxide surface. Because the oxide is rigid there is a one-to-one correspondence between δ_{DC} and the distance traveled by the piezo z_{piezo}.

In the second calibration step, the spring constant of the cantilever is measured. The AFM tips used (Nanosensor EFM tip) have a nominal spring constant $k_{tip} = 1\text{-}5$ N/m. To determine k_{tip} more accurately we use the thermal noise method (Hutter & Bechhoefer 1993). A typical frequency spectrum for the thermal motion of a tip is
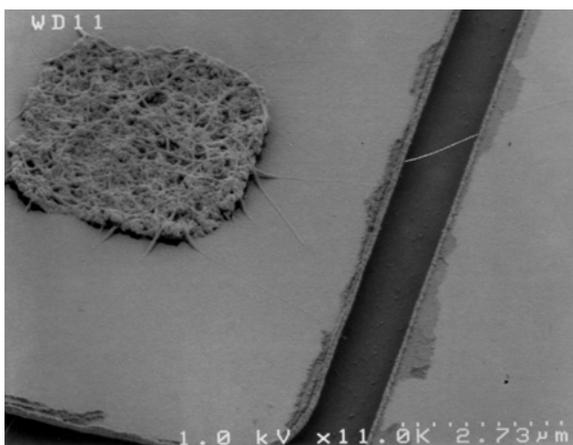
Figure 3.2. SEM image of a nanotube device. A catalyst pad is seen on the left (4 μm square). Hundreds of NTs grow in the catalyst area. The distance between the catalyst pad and the edge of electrodes is chosen so that, on average, one NT bridges the gap between the electrodes.

(a)

$\delta_{DC} > 0$

z_{piezo}

(b)

Deflection signal (V)

z_{piezo} (nm)

(c)

$\langle x^2 \rangle$

(nm^2/Hz)

frequency (kHz)
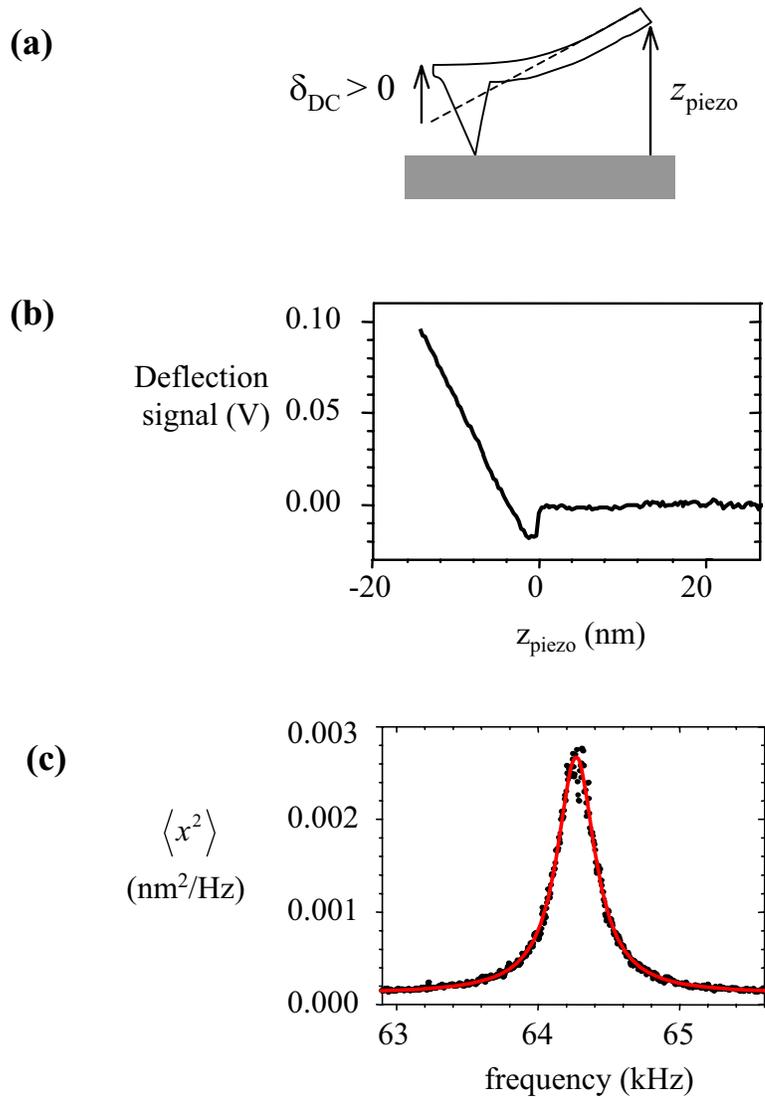
Figure 3.3 AFM calibration **(a)** Pushing the AFM tip into a rigid surface to calibrate δ_{DC}. The spring-like cantilever is bent backward. A laser aimed at the back of the cantilever reflects onto a photodetector. **(b)** The photodetector's response to cantilever deflection. The photodetector signal is proportional to δ_{DC}. **(c)** Thermal motion of an AFM cantilever at room temperature. The fit curve is a Lorentzian with integrated area 0.0013 nm^2. The area under the curve implies the cantilever spring constant is 3.1 N/m.

shown in Fig 3.3c. The measurement was made with a Stanford Research Systems Spectrum Analyser and a two minute integration time. From the area under the Lorentzian fit curve we the find average thermal displacement $<\delta_{th}^2>$. The total energy stored in this vibrational mode is $\frac{1}{2}\,k_{tip}<\delta_{th}^2>$. Comparing this energy to $\frac{1}{2}\,k_B T$ we have, by the equipartition theorem,

$$k_{tip} = \frac{k_b T}{\left\langle \delta_{Th}^2 \right\rangle}.$$

After completing these calibration steps the AFM can be used to measure forces in z-direction, $F_z = k_{tip}\delta_{DC}$.

We locate suspended NT devices in the AFM by tapping mode imaging. In this mode, the cantilever is driven into oscillation at its resonant frequency. The oscillation amplitude drops when the tip approaches the surface, or comes into contact with a suspended NT (the interaction between the suspended NT and the oscillating AFM tip is discussed in Appendix 1). Topography is mapped by recording the height of the AFM tip while a feed-back circuit maintains a constant oscillation amplitude. A typical image is shown in Fig 3.4a. The suspended NT appears fuzzy because it is displaced by the AFM tip during imaging.

To make mechanical measurements, the AFM tip (nominal radius of curvature of 20 nm) is centered above a suspended NT using the tapping mode image for guidance. Piezo drift is neglible on the time-scale of ~ 1 minute if the x-y position is allowed several minutes to stabilize. The AFM tip is then moved in the z-direction as illustrated in Fig. 3.4b. As the AFM tip pushes on the NT the oscillation amplitude drops to zero (see Appendix 1) and we monitor the static deflection of the cantilever δ_{DC}. Note that the position of the tip z_{tip} depends on both z_{piezo} and δ_{DC} as shown in Fig 3.4c.

(a)

500nm

0   400nm

(b)

gold θ gold

$z_{tip} < 0$

L_0

(c)

δ_{DC}

z_{piezo}

z_{tip}
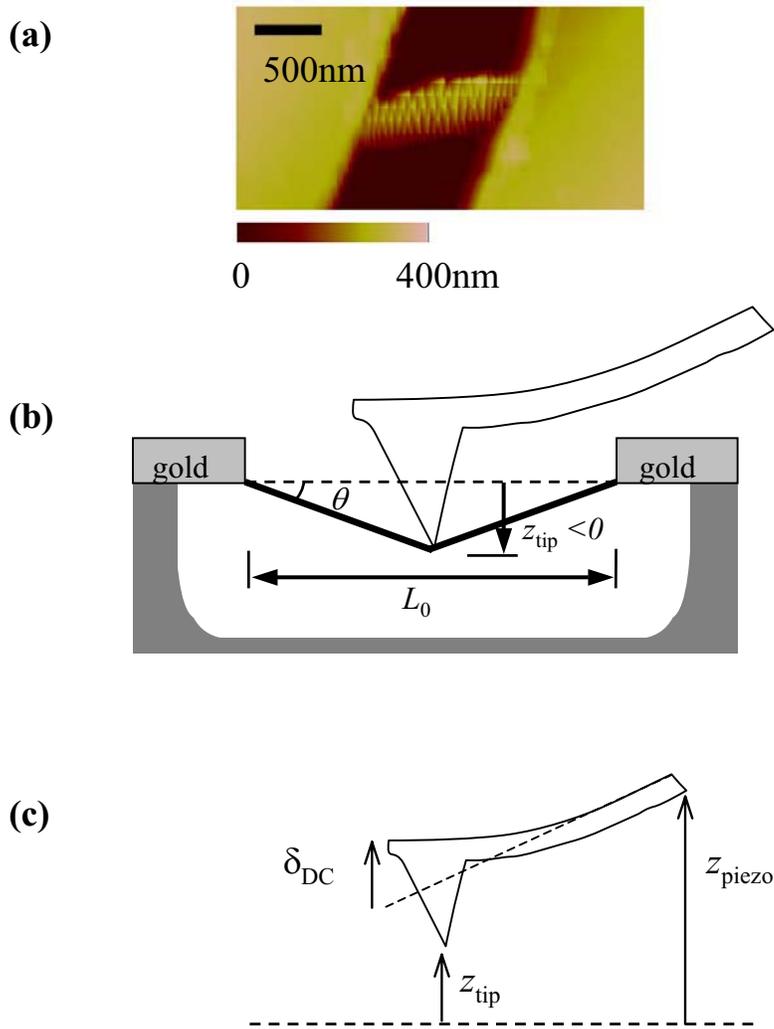
Figure 3.4 (a) AFM image of a suspended NT. **(b)** Experimental geometry for applying strain and gate voltage with an AFM tip. L_0 is distance between anchoring points, z is the distance the center of the NT is displaced from the plane of the anchoring points. **(c)** Schematic of the relationship $z_{tip} = z_{piezo} + \delta_{DC} +$ constant.

3.5 Mechanical Measurements

Plotted in Fig. 3.5 is the deflection force on the cantilever F_z, as a function of the tip height z_{tip} while raising the AFM tip. Figure 3.5 shows that the force the tube exerts on the tip can be both positive (upward) as well as negative (downward). These are separated by a region of near-zero force when the tip is near the plane of the contacts.

From Fig. 3.5 we note that there is significant adhesion between the AFM tip and the NT, allowing the AFM tip to pull upward on a NT. As discussed by Decossas et al. (2001) some adhesion is likely due to van der Waals forces between NT and tip. In Appendix 2 we show that NT/tip adhesion is also sensitive to electrostatic forces.

From force-distance curves such as Fig. 3.5 we can determine the "slack" in suspended NTs. Slack is defined here as $L_{tube} - L_0$ where L_{tube}, the tube length, is greater than L_0, the separation between the anchoring points. We determine slack from the distance between pushing and pulling onsets, $\pm z_{onset}$, in a force-distance curve. For example, in Fig 3.5, NT1 has $z_{onset} = 80$ nm and $L_0 = 1 \mu$m. From the sides of a right-angle triangle we have

$$\left(\frac{L_{Tube}}{2}\right)^2 = \left(\frac{L_0}{2}\right)^2 + z_{onset}^2$$

Nearly all NTs measured were slack, with typically 5-10nm of slack for a 1 μm tube. The slack is consistent with the slightly curved paths NTs followed across the oxide surface before etching. We have been able to manipulate the slack in NTs, as discussed in Section 3.6.

Our force-distance curves can be accurately fit by ignoring the bending modulus of the tube and assuming a linear proportionality between NT tension T and axial strain σ. We write the proportionality constant as YA, where Y is an effective Young's modulus, and A is an effective cross-sectional area of the NT:
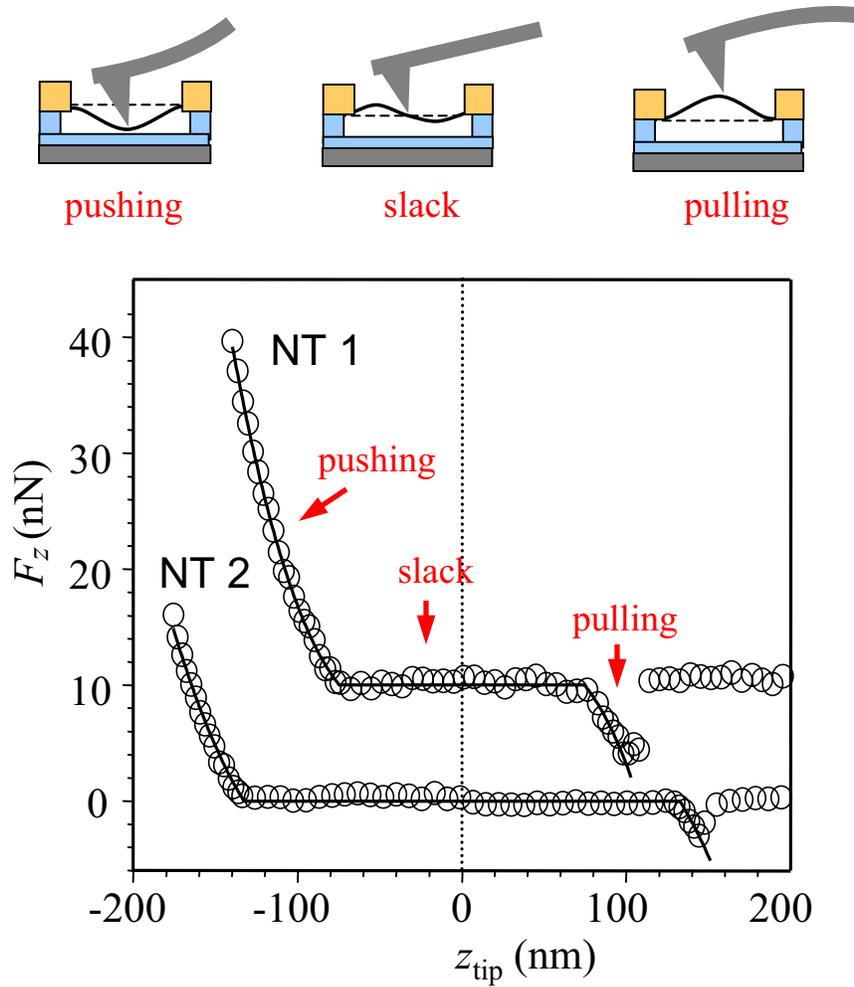
Figure 3.5 Force-distance curves of two NTs; Data from NT 1 is offset for clarity. Open circles show the measured deflection force as the AFM tip retracts towards positive z. NT 1 has D=5.3±0.5nm, L_0=1.0±0.1μm. NT 2 has D= 2.3±0.5nm, L_0=1.5±0.1μm. Solid lines are fit curves given by Eq. 3.1. We find NT 1 has slack=11nm, AY=2μN and NT 2 has slack=22nm and AY=2.9μN. The tubes were not measured by the same AFM cantilever.

$$F_z(z_{tip}) = 2T \sin\theta = 2\left(YA \cdot \sigma(z_{tip})\right) \cdot \left(\frac{2z_{tip}}{\sqrt{L_o^2 + 4z_{tip}^2}}\right) \quad \text{for } |z_{tip}| \geq z_{\text{onset}} \text{ and}$$

$$F_z(z_{tip}) = 0 \qquad \text{for } |z_{tip}| \leq z_{\text{onset}} \tag{3.1}$$

where $\sigma(z) = \left(\sqrt{L_0^2 + 4z_{tip}^2} - L_{\text{tube}}\right)/L_{\text{tube}}$ for $|z_{tip}| \geq z_{\text{onset}}$. Equation 3.1 was used to draw the fit curves in Fig 3.5a. The accurate fit shows that the small-strain mechanical behavior of long, suspended NTs is well described by the effective parameter YA.

A summary of fitted YA parameters, for NTs with a range of diameters D, is shown in Fig. 3.6. Error bars on YA values are considerable, due to the combination of uncertainty in L_0, x-y tip positioning and the cantilever spring constant. However, we can still make important observations. The three lines in Fig. 3.6 show theoretical predictions for YA of single-, double- and triple- wall NTs when all walls share mechanical load (each wall contributes $YA \approx 0.36$ [μN/nm]$*\pi D$ (Yakobson et al. 1996; Lu 1997)). The observed magnitudes of YA and linearity with diameter agree reasonably with the single-wall prediction. This result is initially surprising; NTs with $D > 2$nm are likely to have multiple walls. A possible explanation for this mechanical behavior follows from experiments by Yu et al. (2000) which show that only the outer-most wall of a MWNT breaks when a NT is over strained. From Yu's results, and our measurements of YA magnitude, it appears that mechanical loads are carried predominantly by the outer-most wall of MWNTs, while inner-walls remain unstrained. For this to occur, inner walls must be free to slide against the outer wall.
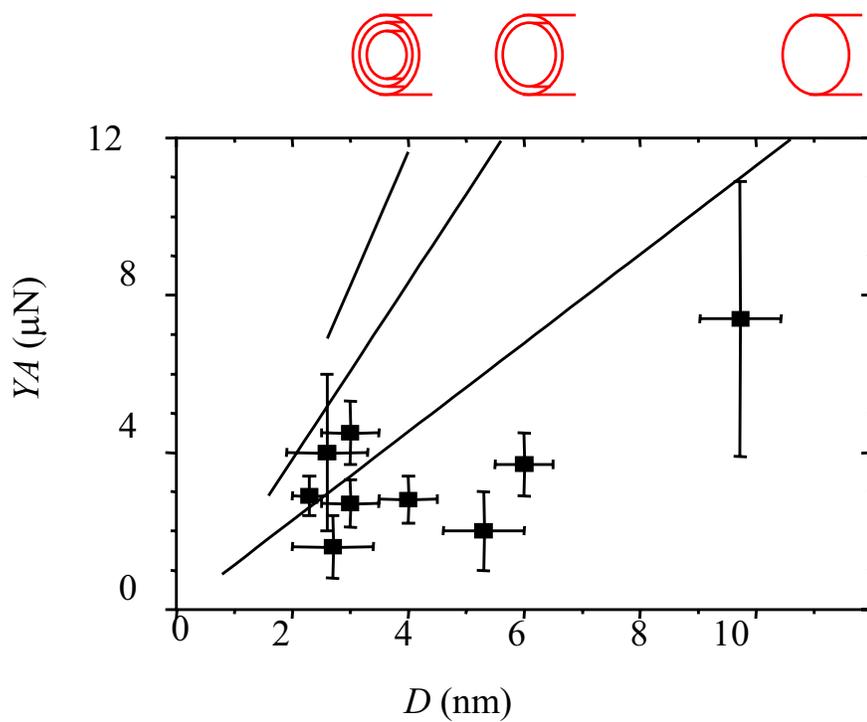
**Figure 3.6** Summary of measured strain-tension proportionality constants, *AY*, for NTs as a function of diameter *D*. Solid lines show predicted *AY* values for single-, double- and triple-walled NTs when all shells carry the same mechanical load.

3.6 Tuning tension in suspended nanotubes

The suspended NTs we have studied are generally slack after standard processing (see Section 3.5). However, by using AFM manipulation we have been able to create suspended NT structures with built-in tension. This technique will be useful for applications such as tuning the frequency of nano-mechanical resonators (Sazonova et al. 2004).

Figure 3.7 shows force-distance curves taken before and after NT tension has been modified. We first concentrate on the upper curve which shows the NT in the slack state. The elastic properties of the tube can be found by fitting Eq 1 to the force-distance curve. We find slack = 9nm and $AY = 3.6\mu N$.

To build tension in the suspended segment of a NT we manipulate a nearby oxide-bound segment of the same NT. Figure 3.7b shows the oxide-bound segment on the right-hand side of the trench. The AFM tip was pressed against the oxide surface with a force of ~ 200 nN and then dragged across the oxide. The arrows in Fig. 3.7b indicate the path taken by the AFM tip as it pushed the tube in three different places. The dashed line indicates the original position of the NT on the oxide.

This manipulation put significant tension into the suspended section of the NT as shown by the lower curve of Fig 3.7a. We estimate tension T from the slope of $F_z(z_{tip})$ at $z_{tip}=0$

$$\left. \frac{dF_z}{dz_{tip}} \right|_{z_{tip}=0} = \frac{d}{dz_{tip}} \left(2T \frac{z_{tip}}{(L_0 / 2)} \right) = \frac{4T}{L_0}$$

From Fig 3.7a we find $(dF_z/dz_{tip})|_{z=0}$ ~ 0.2N/m and $T = 85$nN (σ ~ 2%). The adhesion of the NT to the oxide substrate is sufficient to hold this strain in place. This tensioned
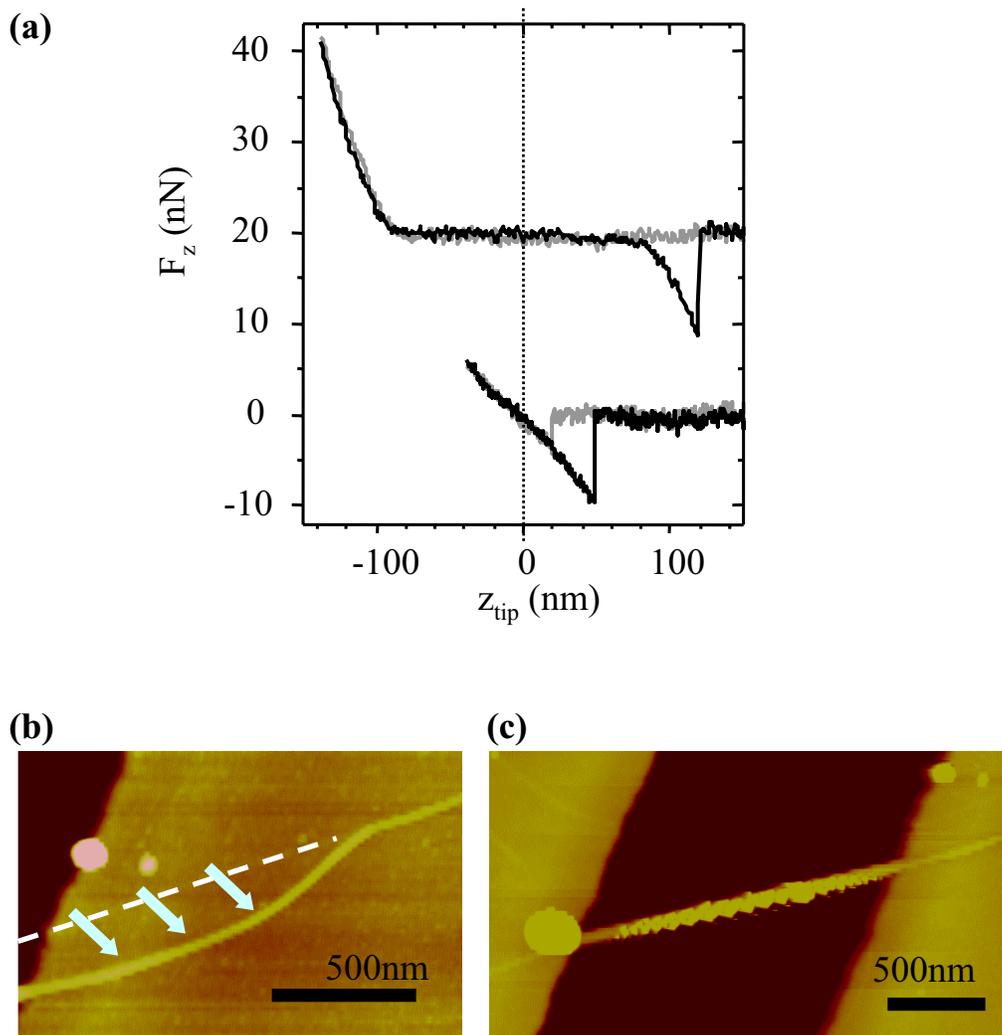
Figure 3.7 Creating tension in a suspended NT. **(a)** The first measurement (upper curve) was made on the NT in its slack configuration. From $z_{onset} = 90nm$ and $L_0 \sim 1.7um$ we find $L_{tube} = L_0 + 9nm$. The second measurement (lower curve) was taken after the NT was pushed to a new position on the oxide. **(b)** The manipulated section of oxide-bound NT. The arrows indicate where the AFM tip pushed the tube across the surface. The dashed line shows the initial position of the NT. **(c)** The suspended NT in the tight configuration. The NT diameter $D = 5nm$.

NT should have resonance properties like a guitar string with a fundamental resonance defined by L_0 and T, rather than bending modulus.

3.7 Limited range of strain

The work presented in this chapter is limited to strains of about 2%. At higher strain we encounter problems such as the NT slipping up the side of the pyramidal AFM tip or sliding across the oxide surface.

There are many interesting possibilities to explore at higher strains. For example, the onset of plastic deformations (irreversible changes in bonding topology) is predicted to depend sensitively on temperature and NT chirality (Nardelli et al. 1998; Zhang et al. 1998). The onset of these deformations could be detected by mechanical measurements. Electromechanical effects at high strain are also predicted to be very interesting (Heyd et al. 1997; Rochefort et al. 1998; Yang et al. 1999; Yang & Han 2000).

Possibilities for reaching higher strain are promising, but require new methods of device fabrication and different AFM techniques. For example, recent work showed that the ends of suspended NTs can be embedded in oxide (Whittaker et al. 2003) or resin (Kim et al. 2002). These embedded tubes may have improved mechanical anchoring. Problems of tube/tip slipping may be solved with lateral force microscopy. In this technique, the side of the AFM tip is used to pull the structures sideways while measuring twisting forces on the cantilever (Wong et al. 1997; Walters et al. 1999).

3.8 Conclusions

We have successfully used AFM techniques to characterize the slack/tension and elasticity of suspended NT structures. We show that it is possible to control the residual slack or tension in these structures by AFM manipulation.

Our elasticity measurements show that tensile forces in NTs are well described by a proportionality constant *YA* relating strain and tension. A linear trend between *YA* and NT diameter is observed, suggesting that only the outer shell of a MWNT is effective at carrying mechanical load.

CHAPTER 4

TUNING NANOTUBE BANDGAPS WITH STRAIN

4.1 Introduction

Carbon nanotubes (NT) have exciting electromechanical properties. The conductance of a metallic NT can be dramatically lowered by mechanical strain (Tombler et al. 2000) and it is hoped that NTs may be used as the active elements in nano-electromechanical devices such as strain gauges and pressure sensors. As discussed in Chapter 2, NT electromechanical properties are expected to depend sensitively on chirality, with axial strain predicted to open a bandgap in certain metallic NTs, and to either open or close the bandgap of semiconducting NTs (Heyd et al. 1997; Rochefort et al. 1998; Yang et al. 1999; Yang & Han 2000). These chirality dependent predictions suggest that there is a rich variety of electromechanical effects to be explored in NTs.

In this chapter we study the relationship between axial strain and electronic structure in a number of individual NTs. Following the pioneering work of Tombler et al (Tombler et al. 2000) we use an atomic force microscope (AFM) tip to strain doubly-clamped suspended NTs while simultaneously measuring electrical transport characteristics (Fig. 4.1). Our measurements show that the conductance of some NTs decreases with strain while the conductance of others increases. We show that these changes in conductance are related to either increasing or decreasing bandgaps. Our measurements are consistent with theory (Heyd et al. 1997; Rochefort et al. 1998; Yang et al. 1999; Yang & Han 2000) and provide the first conclusive evidence that strain can be used to tune NT bandgaps.
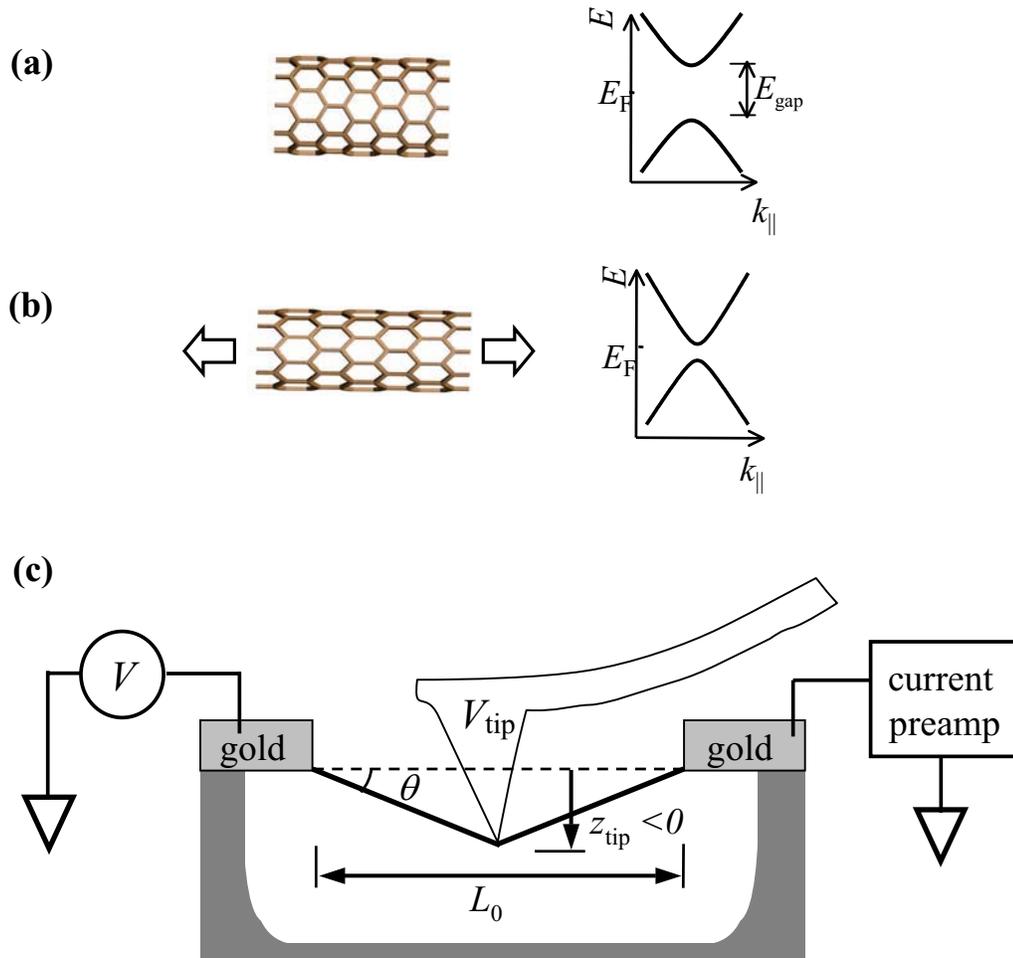
Figure 4.1 Straining a NT and measuring changes in bandgap. **(a)** A semiconduting NT with chiral angle $\phi = 0$ and bandgap E_{gap}. **(b)** The same NT after mechanical stretching. The bandgap is modified due to strain. **(c)** Experimental geometry for applying strain and gate voltage with an AFM tip, and measuring conductance with gold contacts. L_0 is the distance between anchoring points; z_{tip} is the height of the AFM tip, measured from the plane of the anchoring points.

4.2 Methods

Suspended NT devices were fabricated as described in Section 3.3. The oxide substrate is etched from beneath the NT, leaving the tube hanging between gold electrodes (Fig. 4.1c). The entire length of NT is suspended allowing the whole tube to be uniformly strained.

Electromechanical measurements are carried out in the atomic force microscope (AFM) described in Chapter 3 (Dimension 3100, Digital Instruments). Probe station manipulators mounted to the AFM stage were used to make electrical contact to the NT devices (Park et al. 2002). Conductance measurements were made at low-bias (10mV) using a lock-in amplifier. Axial strain σ was controlled by pushing or pulling on the suspended tube with the AFM tip (see Fig. 4.1 and Sections 3.3 and 3.4).

The AFM tips used (Nanosensor EFM tip) have a nominal radius of 20 nm, cantilever spring constants k_{tip} = 1-5 N/m, and are coated with a PtIr metal layer. The conductive coating allows us to use the tip as a local gate to change electrostatic potential of the NT. The PtIr coating makes very poor electrical contact with the NT and leakage currents occur very infrequently.

4.3 Electromechanical measurements

To probe the electromechanical response of a NT, we monitor device conductance G and control AFM tip voltage V_{tip} while straining the tube. Figure 4.2 shows the deflection force on the AFM tip F_z, and conductance G, while pushing (z_{tip} <0) and then pulling (z_{tip} > 0) on a tube. V_{tip} is held at 0V. Whenever the cantilever is deflected (σ > 0), G is lowered, in agreement with previous results (Tombler et al. 2000). When the NT is released from the AFM tip (z_{tip} = 110nm) conductance returns to the zero-strain value.
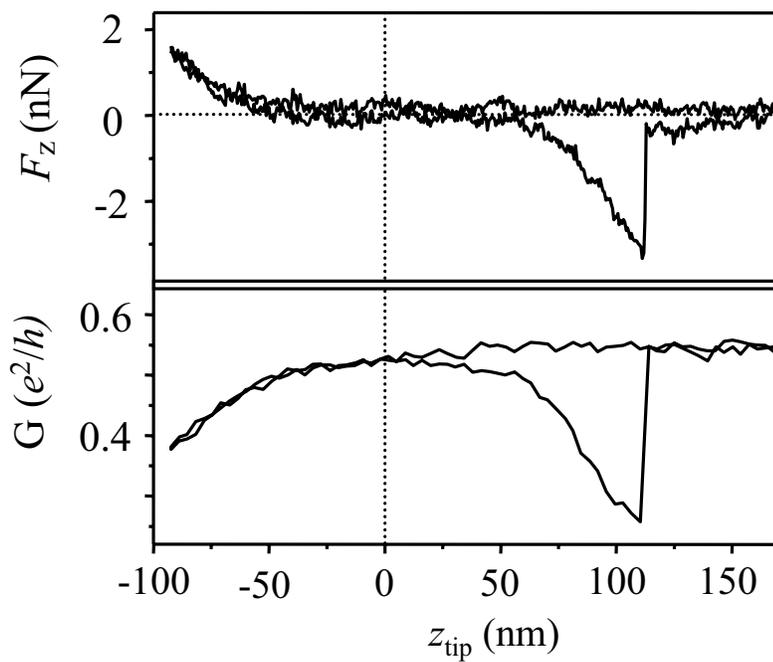
Figure 4.2 Deflection force and conductance as a function of tip height for a NT with $d = 6.5$nm, $L_0 = 1.9\mu$m at $V_{tip} = 0$V. The tip was first moved toward the surface (toward negative z) and then away from the surface.

Interestingly, different NTs showed very different response to strain. Of the seven samples studied, two semiconducting tubes showed *increasing G* when strained, one semiconducting and two metallic tubes showed decreasing *G* when strained. We have also observed two metallic tubes which showed no significant change in conductance when strained.

To understand the origin of this behavior, the AFM tip is used as a gate to investigate the band structure of the NT under strain. V_{tip} is swept ~ 3 times a second over a range of a few volts as strain is slowly increased. *G* vs. V_{tip} for different σ are shown in Fig. 4.3 for two NTs. We first concentrate on Fig. 4.3a. At no strain ($\sigma = 0$) the observed V_{tip} dependence indicates that this NT is metallic (*G* is independent of V_{tip}). As strain increases, an asymmetric dip centered at $V_{tip} \approx 1V$ develops in G-V_{tip}. The NT shown in Fig. 4.3b is semiconducting at $\sigma = 0$ (*G* is strongly dependent on V_{tip}). This semiconducting tube shows an increase of *G* with strain and the dip in G-V_{tip} becomes more symmetric with strain. The insets show the maximum resistance $R_{max}(\sigma)$ for each sweep of V_{tip} as a function of strain, along with a fit to the functional form:

$$R_{max}(\sigma) = R_0 + R_1 \exp(\beta\sigma).$$

(4.1)

This exponential form fits the data well in both cases, but with different values of R_0, R_1 and β.
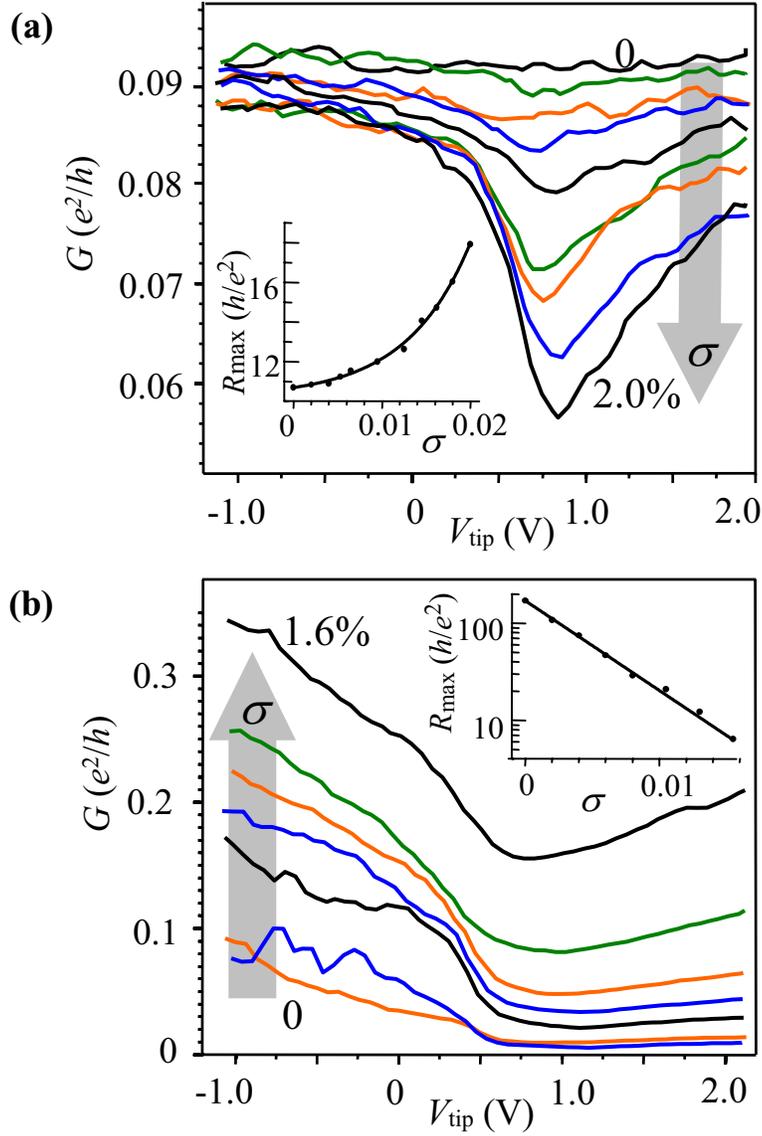
Figure 4.3 (a) G-V_{tip} measurements of NT with $d = 3 \pm 0.5$nm and $L_0 = 1.4 \pm 0.1\mu$m at 0, 0.5, 0.7, 1.0, 1.2, 1.4, 1.6, 1.8 and 2.0% strain. **(b)** G-V_{tip} measurements of NT with $d = 4 \pm 0.5$nm and $L_0 = 1.1 \pm 0.1\mu$m at 0, 0.2, 0.6, 0.8, 1.1, 1.3, and 1.6% strain. Closed circles in the insets show maximum device resistance as a function of strain. Solid lines in the insets show fit curves given by Eq. 3. For (a) $R_0 = 10.2h/e^2$, $R_1 = 0.5h/e^2$ and $\beta = 139$. For (b) $R_0 = 0$, $R_1 = 171h/e^2$ and $\beta = -213$.

4.4 Analysis of electromechanical measurements

Our electromechanical measurements can be understood by the effect of axial strain on the bandgap of the tube, as described by previous authors (Heyd et al. 1997; Yang et al. 1999; Yang & Han 2000). From Chapter 2, Eq 2.10 we have

$$\frac{dE_{gap}}{d\sigma} = \text{sign}(2p+1)3t_0(1+\upsilon)\cos3\phi, \tag{4.2}$$

where $t_0 \approx 2.7\text{eV}$ is the tight-binding overlap integral, $\upsilon \approx 0.2$ is the Poisson ratio, ϕ is NT chiral angle and $p = -1$, 0 or 1 such that the wrapping indices, n_1 and n_2 satisfy $n_1 - n_2 = 3q + p$ where q is an integer. The maximum value of $\left|dE_{gap}/d\sigma\right|$ is $3t_0(1+\upsilon) \approx 100\text{meV}/\%$. Note that half of all semiconducting NTs ($p = 1$) will have $dE_{gap}/d\sigma > 0$, while the other half ($p = -1$) have $dE_{gap}/d\sigma < 0$.

We first interpret the measurements taken at constant V_{tip} (such as Fig. 4.2). When strain causes G to decreases we have $dE_{gap}/d\sigma > 0$. When strain causes G to increase we have $dE_{gap}/d\sigma < 0$. If G does not change, then $dE_{gap}/d\sigma$ is close enough to zero to be undetectable.[1]

The G-V_{tip} curves shown in Fig. 4.3 confirm this picture. The changing shape of these curves indicates a changing bandgap. Both NTs conduct well at negative tip voltages showing they are p-type for $V_{tip} < 0$. Increasing V_{tip} electrostatically depletes the p-type carriers from the NTs causing a dip in conductance. The size of the conductance dip depends on E_{gap}, which changes with strain. In Fig. 4.3a the conductance dip deepens with σ (indicting an increasing E_{gap}), while in Fig. 4.3b the minimum conductance increases with σ (indicating decreasing E_{gap}).

---

[1] Changes in the intrinsic conductance of a NT can be masked by the contact resistance between the NT and the metal electrodes. We observed two metallic NTs which showed no change in conductance at strains of ~ 1%. Based on the contact resistance of these devices, and measurement noise, we estimate that dE_{gap}/dσ could be up to 10 meV/% in these devices where conductance changes were not detected.

To model changes in conductance associated with changing E_{gap} we assume the tip gate affects the middle portion of the tube while sections close to the contacts remain p-type (Park & McEuen 2001). For small positive V_{tip} the middle portion of NT is depleted of charge carriers (Fig. 4.4b). At higher V_{tip} an n-type region develops in the middle of the tube (Fig. 4.4c). As V_{tip} increases further, there is an increasing probability of tunneling between p-type and n-type sections and G can increase.

The model shown in Fig. 4.4 predicts that the maximum device resistance R_{max} will occur shortly before the depleted section of NT becomes n-type. Referring to Fig. 4.4b electrons with energy $|E\text{-}E_F|<E_{gap}$ will be reflected (neglecting the probability of tunneling between the p-type regions), while electrons with energy $|E\text{-}E_F|>E_{gap}$ will be transmitted with some probability $|t|^2$. We calculate the current I due to these thermally activated carriers by following the Landauer formalism for a 1D channel (see Appendix 3),

$$I = |t|^2 \frac{2e}{h} \cdot 2 \int_{E_F+E_{gap}}^{\infty} (f_R(E) - f_L(E)) dE ,$$

$$= |t|^2 \frac{2e^2}{h} \cdot \frac{2}{1 + \exp(E_{gap}/k_bT)} V$$

where f_R and f_L are the Fermi distributions in the left and right electrodes and reflected electrons have been excluded from the integral. The current in this channel depends on the width of the Fermi distributions ($\propto T$) compared to the size of E_{gap}.

A NT has two 1D channels and additional series resistances R_S due to metal-NT contacts etc. Therefore, we find the following expression for R_{max},:

(a) $V_{tip}=0$

C

E_{gap}

V

E_F

$x_{tube\ axis}$

(b) $V_{tip} \approx 1V$

ζ

(c) $V_{tip} > 1V$

ζ
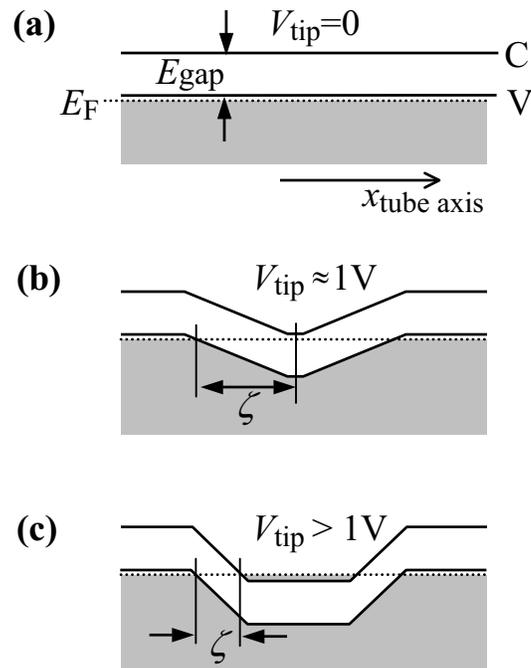
Figure 4.4 Evolution of the energy band diagram as V_{tip} is increased. The tube is held p-type at the contacts. The valence and conduction band edges are denoted by V and C. **(a)** $V_{tip} = 0$, the NT is a p-type semiconductor. **(b)** V_{tip} is near 1V, transport is interrupted by a depleted region. **(c)** $V_{tip} > 1V$, a p-n-p junction forms in the middle of the tube. Transport due to tunneling increases as the distance ζ becomes smaller.

$$R_{\max} = R_S + \frac{1}{|t|^2} \frac{h}{8e^2} \left(1 + \exp\left(\frac{E_{gap}}{k_b T} \right) \right), \tag{4.3}$$

where E_{gap} is expected to depend linearly on strain,

$$E_{gap} = E_{gap}^0 + \frac{dE_{gap}}{d\sigma} \sigma . \tag{4.4}$$

By combining Eqs (4.3) and (4.4) we can interpret the fitting parameters β, R_0 and R_1 that were used to fit measured $R_{\max}(\sigma)$ (see Eq. (4.1)). Most important is β, the exponential fitting parameter which is related to the strain-dependence of the gap: $dE_{gap}/d\sigma = \beta kT$. From the measured values of β, we obtain $dE_{gap}/d\sigma = -53\text{meV}/\%$ for the semiconducting tube in Fig. 4.3b and $dE_{gap}/d\sigma = +35$ meV/% for the metallic tube in Fig. 4.3a.

Additional knowledge about the device can be gained from the fitting parameter $R_1 = (h/8e^2|t|^2) \exp(E_{gap}^0/kT)$. Fitting results for the metallic tube ($E_{gap}^0 = 0$) gives R_1 = 0.49h/e^2, and hence a transmission probability $|t|^2 = 0.25$. Transport of thermally activated electrons across the junction region is thus not ballistic, but nevertheless highly transmissive, as expected from previous measurements of long mean free paths in NTs (Bachtold et al. 2000). Fitting the semiconducting tube data yields a much higher resistance, $R_1 = 171 h/e^2$. Using an estimate of $|t|^2 = 0.25$ from above, we infer $E_{gap}^0 = 160\text{meV}$. This inferred energy gap corresponds to a tube with diameter $d = $ 4.7nm (using $E_{gap} = 0.7\text{eV}/D$[nm] (Dresselhaus et al. 2001)), in reasonable agreement with $d = 4 \pm 0.5$nm measured by AFM. The agreement provides support for the validity of Eq. 4.3. However, variable temperature studies are needed to definitively separate out the tunneling and thermal activation contributions.

4.5 Tunneling model

To better understand the role of tunneling in our measurements we have used a WKB model to quantify the tunneling contribution to R_{max}.

In our expression for R_{max} (Eq. (4.3)) we assume that electrons with $|E-E_F|<E_{gap}$ are completely reflected from the depleted section of the NT (Fig. 4.4b). However, there is a possibility that some of these electrons are transmitted via tunneling processes. To calculate the current from tunneling electrons we consider the WKB expression for the probability of tunneling through a triangular barrier length L and steepness ε (Fig. 4.5a)

$$P_{\text{tunnel}}(L) = \exp\left(-\frac{2}{\hbar}2\int_0^{L/2}\sqrt{2m_{eff}\varepsilon x}\,dx\right)$$

$$= \exp\left(-\frac{\sqrt{2}}{\hbar v_F}E_{gap}^{1/2}\varepsilon^{1/2}L^{3/2}\right),$$

where $m_{eff}=E_{gap}/2v_F^2$. Similar calculations for tunneling probabilities in semiconducting NTs are found in Leonard et al. (1999) and Odintsov (2000).

Referring to Fig. 4.5a, the barrier length L is large for electrons with $E = E_F$ ($L = 2E_{gap}/\varepsilon$) and decreases as E approaches $E_F - E_{gap}$ (L goes to zero). Integrating over this range of energies we estimate a tunneling current

$$I_{tunnel} = \frac{2e}{h}\cdot\int_{EF-Egap}^{EF}P_{tunnel}(E)\big(f_R(E)-f_L(E)\big)dE$$

Figure 4.5b shows I_{tunnel} as a function of E_{gap} for $\varepsilon = 2.5$ meV/nm and 5 meV/nm. For barriers of this steepness the tunneling current is much less than the thermal activation current over all bandgaps. We find that tunneling current becomes

(a)

e^-

Egap

E_F

h^+

(b)

$I/(4e^2V/h)$

1

Thermal current
$kT = 25$ meV

0.1

Tunnel current

$\varepsilon = 5$ meV/nm

0.01

$\varepsilon = 2.5$ meV/nm

0

50

100

150

E_gap (meV)
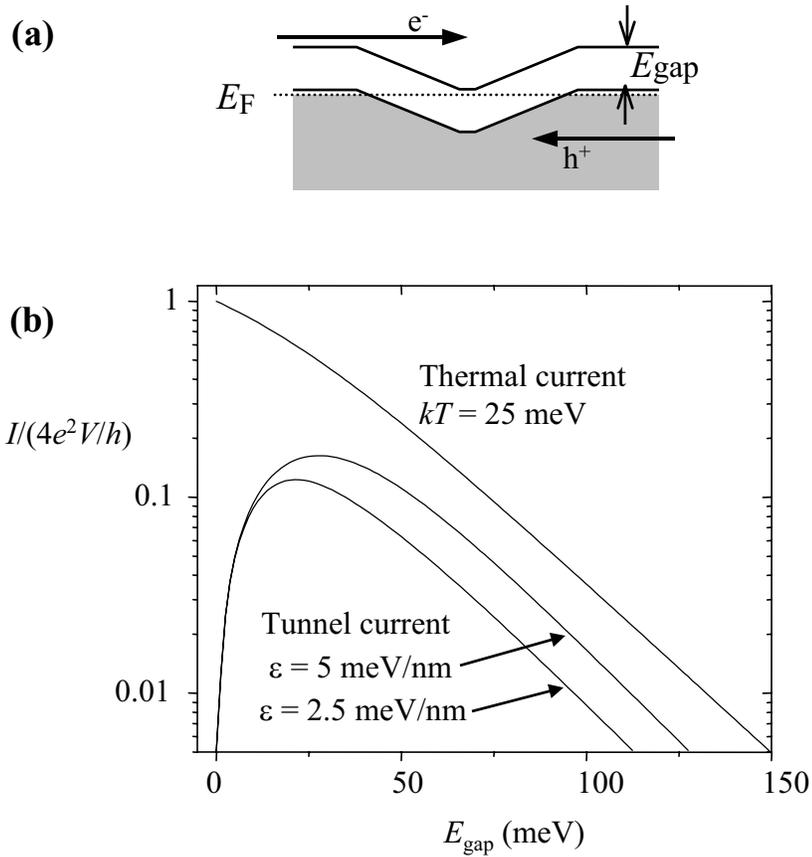
Figure 4.5 Tunneling through the depleted section of NT. **(a)** Holes with energies between E_F-E_gap and E_F may be transmitted via tunneling. The stepness of the barrier is ε. **(b)** Tunneling current and thermal activation current as a function of bandgap (see Eq. 4.5). Tunneling current is smaller thermal activation current for all E_gap if $\varepsilon < 10$ meV/nm.

comparable to thermal activation current when $\varepsilon \sim 10$ meV/nm. This is a reasonable upper bound for ε, corresponding to a depletion length of 20 nm (the radius of the AFM tip) when E_{gap}=200meV (the largest bandgap studied). These calculations show it is reasonable to assume that thermal activation is the dominant transport mechanism in our measurements of R_{max}.

4.6 Effect of local bending

When an AFM tip is used to strain a suspended NT there will be some amount of local deformation where the tube is touched by the tip (Fig. 4.6). In the first analysis of experiments by Tombler et al. (Liu et al. 2000; Tombler et al. 2000), electrical changes were attributed to this deformation. More recent analysis, however, together with the experimental results presented in this chapter, suggests that local deformation is not responsible for electrical changes.

Motivated by Tombler's experiment, Maiti et al. (2002) used molecular dynamics simulations to investigate the electronic effects of pushing a suspended NT with an atomically sharp AFM tip. In this simulation, conductance changes due to local deformation were overwhelmed by the effect of axial strain changing the NT bandgap. Maiti and co-workers conclude that Tombler's results can be explained entirely by bandgap changes induced by axial-strain.

Given these molecular dynamics simulations, and the good agreement between our results and axial-strain predictions, it is unlikely that local deformation contributes significantly to the electrical changes observed in our experiments.
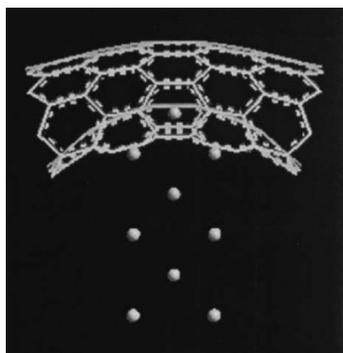
Figure 4.6 Simulation of local bending when a NT is pushed by an AFM tip (from Maiti et al. (2002)). The suspended (12,0) NT bends as pressure is applied by the atomically sharp tip. Atoms in the AFM tip are represented by spheres beneath the NT.

4.7 Chirality assignment

From our measurements of $dE_{gap}/d\sigma$ we can estimate NT chirality. For the NTs in Fig. 4.3(a) and (b) we found $|dE_{gap}/d\sigma|$ = 35 meV/% and 53 meV/% respectively. Using Eq. 4.2 we estimate chiral angles $\phi \approx 23^o$ and 19° for the two tubes. In principle, measurements of $dE_{gap}/d\sigma$ could be an accurate technique for determining chiral angle. The accuracy is currently limited, however, until further experiments verify the quantitative validity of Eqs. 4.2 and 4.3.

Chirality assignment is important as researchers look for correlations between ϕ and physical properties such as the onset of plastic deformations (Nardelli et al. 1998; Zhang et al. 1998) or the existence of curvature induced bandgaps in nominally metallic NTs (Kane & Mele 1997; Zhou et al. 2000). Currently, there are very few methods to experimentally determine the NT chirality. Direct imaging by STM is the most robust method (Odom et al. 1998; Wildoer et al. 1998), but requires special sample preparation, low temperatures, vibration isolation and vacuum. In contrast, measurements of $dE_{gap}/d\sigma$ can be performed in ambient conditions.

Chirality assignment of semiconducting NTs has also been achieved with a combination of photoluminescence and resonance Raman measurements on NTs in solution (Bachilo et al. 2002). The technique could potentially be extended to in-situ measurements of individual semiconducting NT devices. Interestingly, built-in axial strain or twist would confound chirality assignment by this technique, whereas measurements of $dE_{gap}/d\sigma$ should not be affected by built-in strains.

4.8 Conclusions

We have shown that metallic NTs can be made semiconducting with applied mechanical strain, and that the bandgap of semiconducting NTs can be modified by strain. The use of strain to continuously tune the bandgap of a NT has a number of potential applications. Accurate measurements of $dE_{gap}/d\sigma$ may be used to uniquely determine the wrapping indices of small-diameter tubes. Electrical transduction of small forces is also possible; for example, the most sensitive device studied here has a sensitivity of $0.1nN/(Hz)^{1/2}$ at low frequencies. Finally, NT heterostructures, where different sections of a single NT have different bandgaps, can be created if the different sections can be selectively strained. Heterostructures are enormously useful for engineering electronic devices. For example, a 1D super-lattice of quantum wells could be constructed using a periodically strained NT.

CHAPTER 5

ORBITAL MAGNETIC MOMENTS IN CARBON NANOTUBES

5.1 Introduction

Carbon nanotubes (NTs) have impressive mechanical and electromechanical properties, as discussed in previous chapters. Here we show that their magnetic properties are also fascinating and significant.

Electronic states near the energy gap of a NT are predicted to have a large orbital magnetic moment μ_{orb} much larger than the Bohr magneton (the magnetic moment due to electron spin) (Ajiki & Ando 1993; Lu 1995). The moment is due to electron motion around the NT circumference. We have used two techniques to quantitatively confirm predicted values for μ_{orb}. The first technique is thermally activated transport through individual small bandgap NTs that are depleted of charge carriers. These bandgap measurements are very similar to those discussed in Chapter 4. The second technique is transport spectroscopy of NT quantum dots (introduced in Section 1.4), a technique which allows us to probe the energies of discrete quantum states inside a NT. With both methods we measure μ_{orb} values that are in close quantitative agreement with theory (Ajiki & Ando 1993; Lu 1995). Using this coupling between magnetic field and electronic states we modify NT bandgaps, break the degeneracy between NT subbands, and shift energy levels in a NT quantum dot.

5.2 Previous work

Magnetic susceptibility measurements of bulk NT material show that NTs have a much larger magnetic response than other forms of carbon, such as C_{60}, graphite or diamond (Ramirez et al. 1994; Wang et al. 1994; Chauvet et al. 1995). Work with aligned NTs shows that the susceptibility of NTs is also very anisotropic (Chauvet et al. 1995; Walters et al. 2001). It is clear from these measurements that the unique geometry of NTs plays an important role in their magnetic behavior.

Magneto-resistance measurements of large multi-walled NTs ($D \sim 20$ nm) have also yielded interesting results (Bachtold et al. 1999; Fujiwara et al. 1999; Lee et al. 2000). These authors observe resistance modulations as a function of the magnetic flux threading a NT, showing that magnetic field strongly influences NT transport properties. However, the interpretation of these measurements is not clear. Localization effects (Aronov & Sharvin 1987) and changing NT bandgaps (Ajiki & Ando 1993; Lu 1995) may both affect resistance.

5.3 Coupling between magnetic field and electronic states

The effect of axial magnetic field on NT electronic structure can be described in two equivalent ways. Following Ajiki & Ando (1993) and Lu (1995) an Aharonov-Bohm phase is added to electron wave vectors that encircle the NT. The added phase leads to changes in the energy of electron states. Alternatively, a semiclassical argument can be used to calculate a magnetic moment for each electron state. Both descriptions predict the same energy shifts with applied magnetic field. A summary of the semiclassical description is given below (the Aharonov-Bohm description can be found in Section 2.9).

The electronic states of a NT are elegantly described by the quantization of electron wave vectors around a graphene cylinder (Dresselhaus et al. 2001)(see Chapter 2). Graphene is a zero band-gap semiconductor in which the valence and conduction states meet at two points in k-space, $\mathbf{K}_1$ and $\mathbf{K}_2$ (Fig. 5.1a). The dispersion around each of these points is a cone, $E_i(\mathbf{k}) = \hbar v_F |\mathbf{k}\text{-}\mathbf{K}_i|$ (Fig. 5.1b). When graphene is wrapped into a cylinder the electron wave number perpendicular to the NT axis, $k_\perp$, is quantized, satisfying the boundary condition $\pi D k_\perp = 2\pi j$, where D is the NT diameter and j is an integer. The resulting allowed $\mathbf{k}$'s correspond to the horizontal lines in Fig. 5.1a that miss $\mathbf{K}_i$ by an amount $\Delta k_\perp$. The conic sections of the dispersion cones by allowed $\mathbf{k}$ determine the NT band structure near the Fermi level as shown in Fig. 5.1b. The upper and lower branches of the conic sections correspond to the conduction and valence states of the NT. Both the $\mathbf{K}_1$ and $\mathbf{K}_2$ subbands have the same energy gap between conduction and valence states: $E_g^0 = \hbar v_F \Delta k_\perp$, where $v_F = 8\text{x}10^5$ ms^{-1} (Dresselhaus et al. 2001).

The electron states near the energy gap correspond to semi-classical electron orbits encircling the NT in a helical manner. The perpendicular component of orbital velocity $v_\perp = (1/\hbar)\, dE/dk_\perp$ determines the clockwise (CW) or counterclockwise (CCW) sense of an orbit. For example, in Fig. 5.1b we see that $v_\perp$ is negative for the $\mathbf{K}_1$ conduction states but is positive for $\mathbf{K}_1$ valence states. Electrons with positive (negative) $v_\perp$ encircle the NT in a CW (CCW) fashion. By symmetry, each CW (CCW) orbit in the $\mathbf{K}_1$ subband has an equal energy CCW (CW) partner in the $\mathbf{K}_2$ subband. As a consequence, the two subbands are degenerate, but the CW/CCW sense of valence and conduction states is reversed.

From basic electromagnetic theory, an electron moving at velocity v around a loop of diameter D has an orbital magnetic moment of magnitude $\mu = Dev/4$. In a NT, electron states at the band-gap edges, where $v_\perp$ is largest, have an orbital magnetic
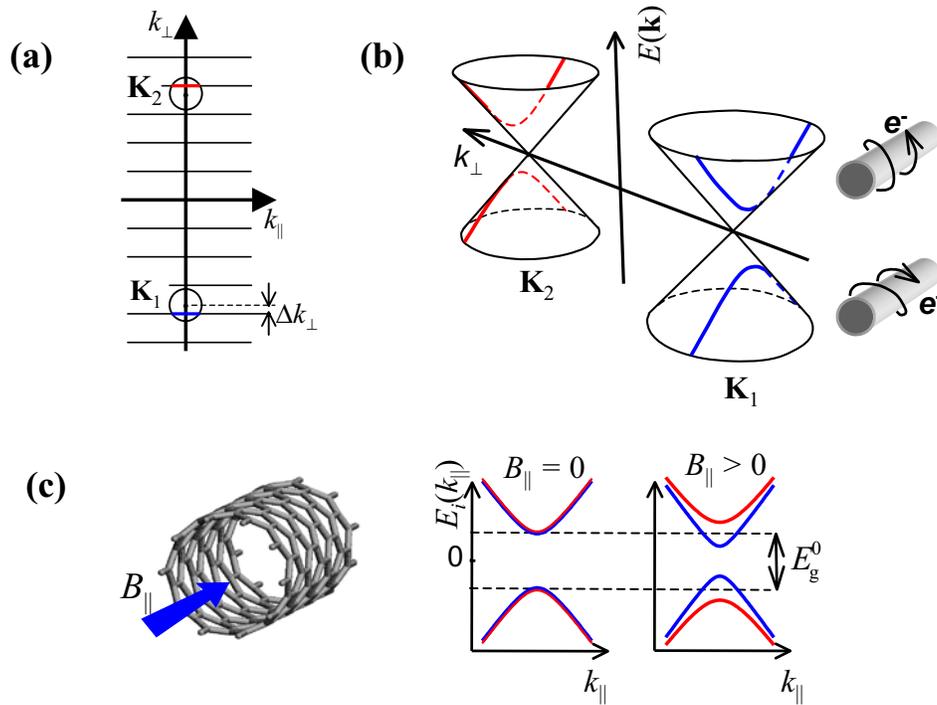
Figure 5.1 Nanotube electronic states and orbital magnetic moments. **(a)** The valence and conduction states of graphene meet at K_1 and K_2. Horizontal lines show the quantized values of $k_\perp$ for the NT structure in (c). The misalignment between horizontal lines and the K points is $\Delta k_\perp$. **(b)** Graphene dispersion near the K-points is described by the cones $E_i(k) = \pm \hbar v_F |\mathbf{k} - \mathbf{K}_i|$. Lines of allowed $\mathbf{k}$ intersect the two cones (blue and red curves). The conduction states near K_1 (upper blue curve) have $dE/d k_\perp < 0$. Electrons in these states move around the CNT in a counterclockwise (CCW) fashion. The valence states near K_1 (lower blue curve) have $dE/dk_\perp > 0$ and are associated with clockwise (CW) electron motion. CCW (CW) orbits correspond to positive (negative) magnetic moments along the CNT axis. The conic section near K_2 lies on the opposite face of an identical dispersion cone. Therefore, K_2 conduction (valence) states have CW (CCW) orbits. **(c)** Top, perspective view of a CNT in the presence of a magnetic field $B_\parallel$. Below, the dispersion relations $E_1(k_\parallel)$ and $E_2(k_\parallel)$, shown in blue and red respectively. The sub-bands are degenerate at $B_\parallel = 0$. The magnetic field breaks this degeneracy.

moment of magnitude $\mu_{\text{orb}} = Dev_F/4$ directed along the tube axis. A magnetic field parallel to the NT axis, $B_{\parallel}$, is predicted to shift the energy of these states by:

$$\Delta E = -\boldsymbol{\mu}_{\text{orb}} \cdot \mathbf{B} = \pm \frac{Dev_F B_{\parallel}}{4}. \tag{5.1}$$

For NTs with a finite energy gap at $B_{\parallel} = 0$, the energy gap of one subband becomes larger as $B_{\parallel}$ is increased, while the energy gap of the other subband becomes smaller (Fig. 5.1c). Electron orbits around a NT are much larger than electron orbits around atomic nuclei, therefore we expect μ_{orb} to be larger than the Bohr magneton μ_B ($\mu_B = 0.058$ meV/T). For a NT with $D = 1$ nm we find $\mu_{\text{orb}} \approx 0.2$ meV/T.

5.4 Suspended nanotube devices

We use small bandgap, suspended NTs in our experiments. Small bandgap NTs (see Section 2.8) have the advantage that thermally activated transport can be studied down to low temperatures ($kT \sim E_g^0$). The NTs are suspended to reduce potential fluctuations along the length of tube. Evidence of potential fluctuations in oxide-bound NTs is seen in scanned gate experiments; different parts of an oxide-bound semiconducting NT are depleted of charge carriers at different gate voltages (Bachtold et al. 2000; Tans & Dekker 2000). A NT in vacuum has a more uniform electrostatic environment than a NT on oxide, therefore, we expect depletion of charge carriers to be more uniform when NTs are suspended. Evidence for uniform depletion is seen in our conductance vs. gate voltage measurements of suspended small bandgap and semiconducting NTs: changes in conductance occur at sharply defined gate voltages. Recent work by the Delft group investigating NT transport before and after suspending a NT also shows reduced electrical disorder in suspended NTs (Jarillo-Herrero et al. 2004).

Devices were fabricated as described in Section 3.3. Trenches were defined between gold electrodes using e-beam lithograph and HF etching. Completed devices had sections of NT both bound to the oxide and suspended above a trench in the oxide (Fig. 5.2).

We have characterised our devices using a gold-coated atomic force microscope (AFM) tip as a movable, local electrode (de Pablo et al. 2002; Yaish et al. 2004). These measurements allow us to observe different doping levels in suspended sections of NT compared to oxide-bound sections of the same NT. For example, Fig. 5.2 shows measurements taken on a semiconducting NT device. The section of NT that rests on the oxide substrate remains conductive (p-type) up to large positive gate voltages. A section of the same NT that is suspended, however, becomes depleted of charge carriers at a much lower gate voltage.

The different threshold voltages for depletion of carriers in oxide-bound and suspended sections of a NT is not a capacitive effect. Removing dielectric material from between the NT and the backgate reduces capacitive coupling to the gate (Nygard & Cobden 2001). Even with a smaller gate coupling, the suspended section is depleted of charge carriers at a lower gate voltage. We conclude that charge on the oxide leads to p-doping of the oxide-bound sections of NT.

The substrate-induced doping effect is important because it allows us to study the electronic structure of a suspended section of NT independently from the adjoining oxide-bound sections. A small bandgap, suspended NT can be tuned from p-type to n-type using a small range of gate voltages. Over this range of gate voltages the oxide-bound sections of the same NT remain conducting and act as p-type electrodes to the suspended section.
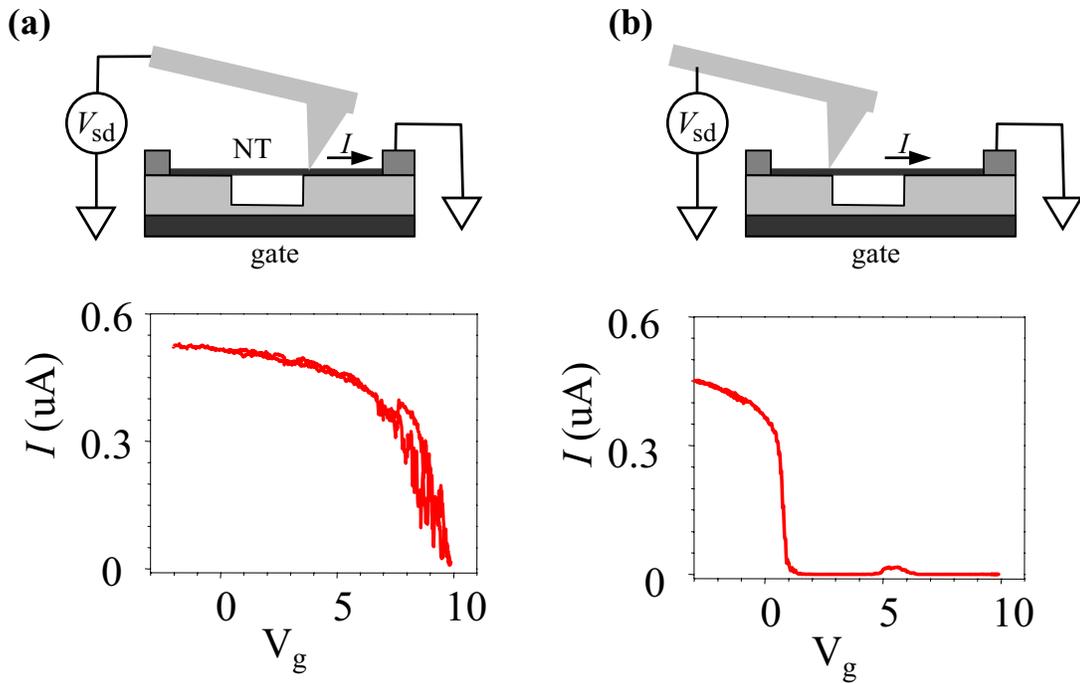
**Figure 5.2** Substrate induced doping. **(a)** A gold-coated AFM tip is used to measure conductance as a function of gate voltage V_g of an oxide-bound section of NT. This section of NT remains conductive up to large positive gate voltage. **(b)** The same measurement is made on the suspended section of NT (with the oxide-bound section in series). Conductance turns off very sharply at a low threshold voltage.

5.5 Thermal activation measurements

We first study thermally activated transport in small bandgap suspended NTs that have been depleted of charge carriers. An axial magnetic field has dramatic effects on this thermally activated current. The experiment is shown schematically in Fig. 5.3. Device conductance G is measured as a function of gate voltage V_g and magnetic field B. The field is misaligned from the NT axis by an angle ϕ.

Figure 5.4a shows G vs. V_g of two small band-gap NTs. Device 1 shows a sharp dip near $V_g = 0.4$ V, corresponding to depletion of carriers in the suspended segment. A second, broader dip occurs at $V_g \approx 2$ V as the oxide-bound segments become depleted. The inset shows the dip from the suspended section of Device 2. In both cases, the addition of a magnetic field substantially increases the conductance at the bottom of the dip.

When the suspended NT segment is depleted, conductance occurs via thermal activation of carriers across the energy gap. Conductance is smallest at $V_g = V^*$, immediately before the suspended segment becomes n-type (Fig. 5.3c). The minimum conductance due to thermal activation, $G_{act}(V^*)$, can be estimated by considering the Fermi-Dirac function at temperature T and the Landauer formalism for 1D conduction channels (Maiti et al. 2002; Minot et al. 2003)(see Appendix 3)

$$G_{act}(V^*,T) = \frac{2e^2}{h} \sum_{i=1,2} |t_i|^2 \frac{2}{\exp(E_g^{K_i}/k_B T)+1}, \qquad (5.2)$$

where $|t_i|^2$ is the transmission probability for thermally activated carriers in the ith subband. The device conductance G is a combination of G_{act} in series with the conductance of the p-type sections of NT and the conductance of the metal-NT contacts, both of which are largely temperature independent.
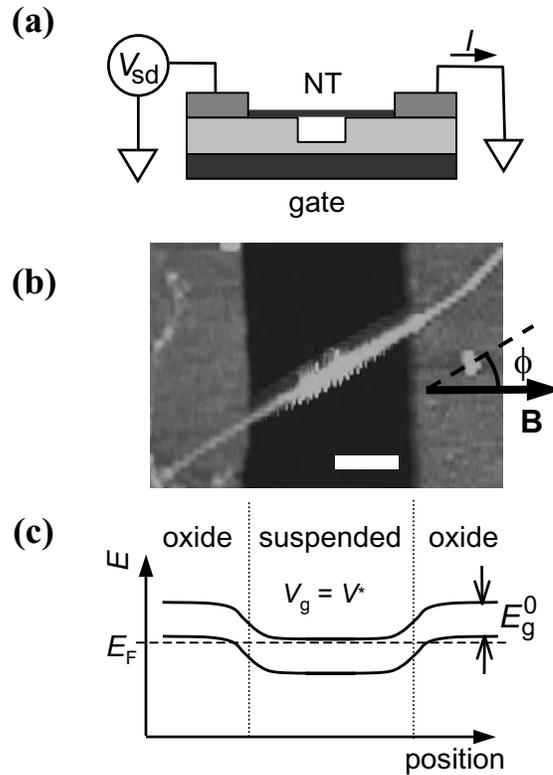
Figure 5.3 Device geometry and band bending. **(a)** The NT lies between two electrodes and crosses a trench in the oxide. **(b)** AFM image of the suspended section of NT and nearby oxide-bound sections of device 1. Scale bar, 130 nm. The suspended section appears fuzzy because it is displaced by the AFM tip during imaging. From the image we find CNT diameter $D=2.6$ nm, suspended length $L=500$ nm, and determine the misalignment angle ϕ between applied magnetic field and the CNT axis. **(c)** Band bending in the suspended NT segment and neighbouring oxide-bound segments when $V_g=V^*$. The number of thermally activated carriers is minimized and there is no n-type region to facilitate tunnelling processes. The oxide-bound sections remain p-type at small V_g.
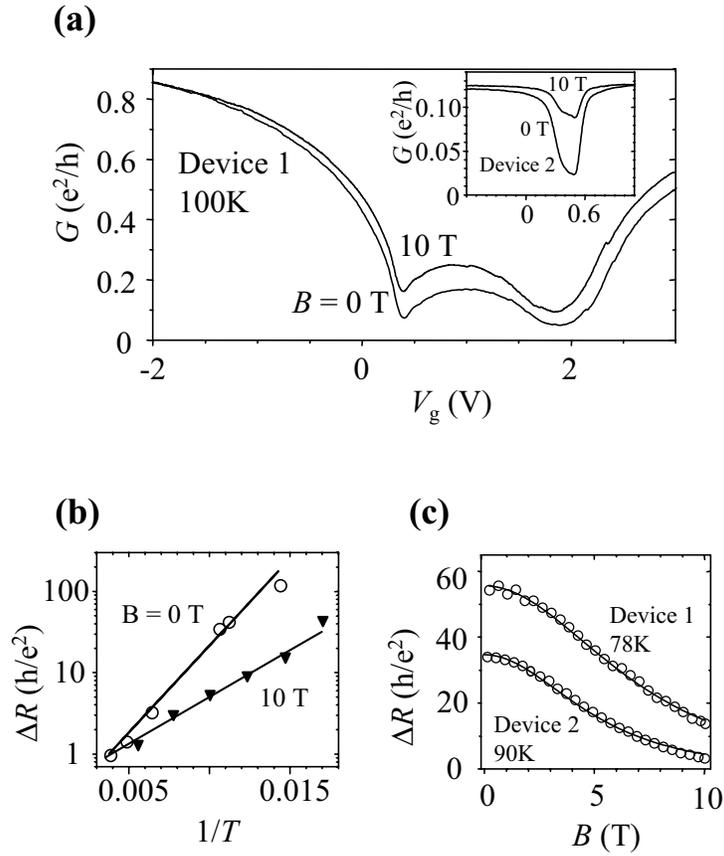
Figure 5.4 Effect of magnetic field on device resistance. **(a)** I–V_g curves for devices 1 and 2 at T=100 K. Curves taken at B=0 T have lower conductance than curves taken at B=10 T. **(b)** ΔR as a function of $1/T$ for device 2. The data shown are for B=0 T (larger ΔR) and B=10 T (smaller ΔR). The fit lines are exponentials of the form $A_0 \exp(A_1/T)$ where A_0 and A_1 are fitting parameters. **(c)** ΔR as a function of B for device 1 at T=78 K (upper curve) and device 2 at T=90 K (lower curve). The fit lines are given by Eq. 5.2 with $E_g^{Ki}=E_0\pm aB$.

We have measured G vs. V_g for Devices 1 and 2 at several temperatures. In Fig. 5.4b (open circles) we plot the change in resistance $\Delta R(T) = G(V^*, T)^{-1} - G(V_g \ll 0, T)^{-1}$ of Device 2 at $B = 0$ T. From the slope and intercept of the fitting exponential, and assuming subband degeneracy ($E_g^{K_i} = E_g^0$) we find: $E_g^0 = 40$ meV [1] and $|t_1|^2 + |t_2|^2 = 1.6$. Because $|t_1|^2 + |t_2|^2$ is close to 2, we conclude that transport is nearly ballistic and that both the $\mathbf{K}_1$ and $\mathbf{K}_2$ subbands make comparable contributions to the device conductance.

Magnetic fields dramatically reduce ΔR, as shown in Fig. 5.4c. The temperature dependence of ΔR at $B = 10$ T is shown for Device 2 in Fig. 5.4b (black triangles). If we fit this high-field temperature-dependence data with the same method used for zero-field data, we find $E_g^0 = 22$ meV and $|t_1|^2 + |t_2|^2 = 0.8$. This change in thermal activation behavior is the first clue that band structure is modified by magnetic field. At least one subband has a significantly smaller bandgap when $B = 10$ T. We argue below that the apparent change in $|t_1|^2 + |t_2|^2$ is due to the increasing band-gap of the second subband.

As magnetic field is swept from 0 to 10T, $\Delta R(B)$ shows a distinctive functional form (Fig. 5.4c). Changes in ΔR are small at low magnetic field, but at larger magnetic field ΔR decreases exponentially. This magnetic field dependence can be quantitatively described by equal and opposite changes in $E_g^{K_1}$ and $E_g^{K_2}$ due to the coupling of μ_{orb} with $B_\parallel$. At low fields, a small decrease in $E_g^{K_1}$ is compensated by a small increase in $E_g^{K_2}$ and ΔR is unchanged. At larger fields the subband with the

---

[1] We find similar values of E_g^0 in both devices (see Table 5.1). As discussed in section 2.8, small bandgaps occur in NTs where $\Delta k_\perp$ non-zero due to perturbations such as strain. If the dominant perturbation in our devices was curvature-induced strain we would expect $E_g^0 \propto 1/D^2$ (Kane & Mele 1997). The bandgaps studied here show no sign of diameter dependence, and are therefore unlikely to be curvature related. Further work is needed to identify the perturbations responsible for E_g^0.

smaller bandgap dominates the thermal activation behavior and we observe a exponential drop in ΔR. Quantitative fits to $\Delta R(B,T)$ are shown in Fig. 5.4c using Eq. 5.2 and setting $E_g^{K_1} = E_g^0 - aB$ and $E_g^{K_2} = E_g^0 + aB$. The only fit parameter is a; E_g^0 and $|t_i|^2$ are found from the temperature dependence of ΔR at $B = 0$ T and setting $|t_1|^2 = |t_2|^2$.

The fitting results for Devices 1 and 2 are summarized in Table 5.1. In agreement with Eq. 5.1, the measured μ_{orb} scale with diameter, and are an order of magnitude larger than previously measured spin magnetic moments in NTs (Cobden et al. 1998; Tans et al. 1998). Thermally activated transport (Eq. 5.2), combined with the breaking of CW/CCW subband degeneracy, describes ΔR over a wide range of T and B. At $B = 10$ T device conductance is almost entirely due to carriers which are thermally activated across the smaller band-gap, explaining why $|t_1|^2 + |t_2|^2$ decreases by a factor of 2 when subband degeneracy is incorrectly assumed at high field. Our measurements confirm theoretical predictions (Ajiki & Ando 1993; Lu 1995) for the sign and magnitude of orbital magnetic moments in NTs and show that an applied magnetic field can split the degeneracy of the $\mathbf{K}_1$ and $\mathbf{K}_2$ subbands.

5.6 Quantum dot spectroscopy

Orbital magnetic moments should also influence the energy level spectra of nanotube quantum dots (NTQDs) in applied magnetic fields (see Section 1.4 for an introduction to NTQDs). In our device geometry a NTQD forms when $V_g > V^*$ and electrons are confined to conduction states of the suspended section by p-n tunnel barriers (Fig. 5.5a). Figure 5.5b shows the formation of a NTQD in Device 1 at $V_g > V^*$, $T = 1.5$ K. There is a large region of zero conductance as the Fermi level passes through the energy gap of the suspended section. At higher V_g the Coulomb diamonds labelled 1, 2, 3 and 4 correspond to charge states of one, two, three and four electrons

Table 5.1 Summary of thermal activation results

	D (nm)	E_g^0 (meV)	ϕ (°)	a (meV/T)	μ_{orb} (meV/T) Experiment	Theory
Device 1	2.6 ± 0.3	36 ± 3	30 ± 3	1.3 ± 0.1	0.7 ± 0.1	0.5 ± 0.1
			60 ± 3	0.7 ± 0.1	0.7 ± 0.1	0.5 ± 0.1
Device 2	5.0 ± 0.3	40 ± 3	45 ± 3	2.1 ± 0.2	1.5 ± 0.2	1.0 ± 0.2

ϕ is the misalignment angle between NT axis and the magnetic field direction. The experimental value of μ_{orb} is given by $a/2\cos\phi$. There is uncertainty in theoretical values of μ_{orb} due to uncertainty in v_F and D.
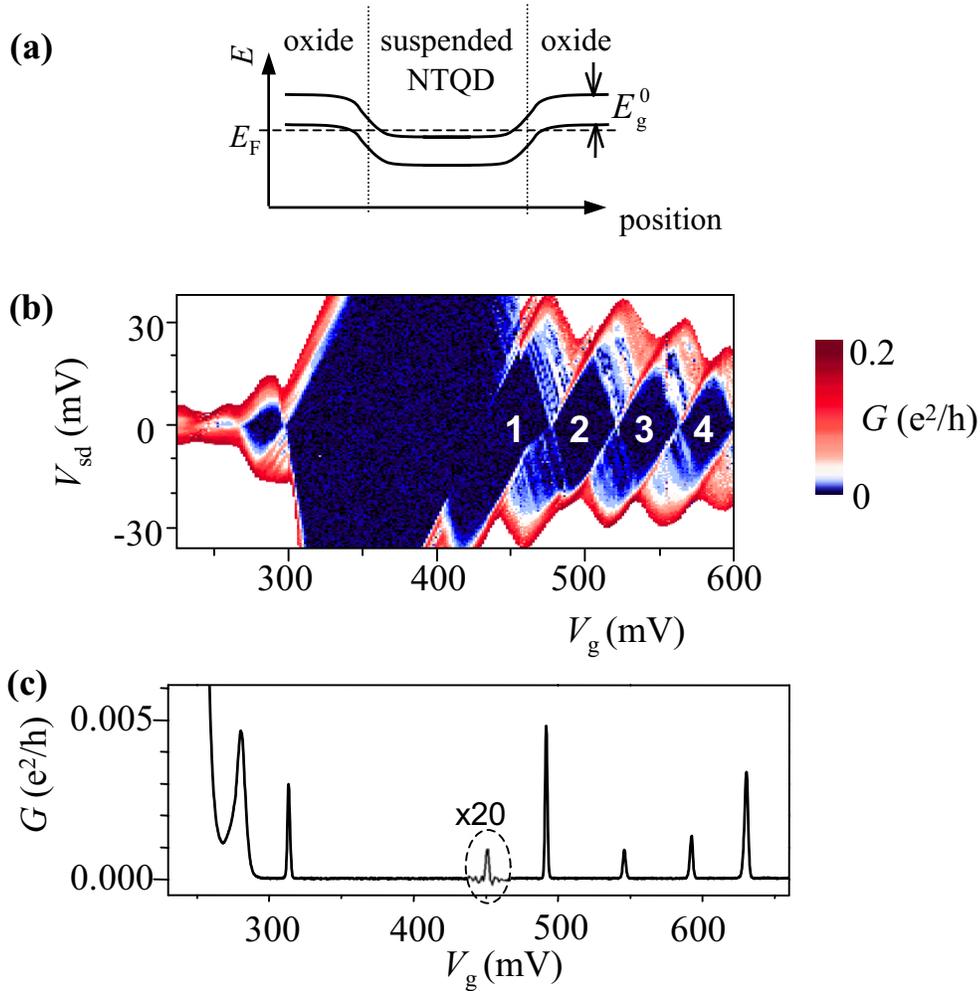
Figure 5.5 (a) Formation of a NTQD when $V_g > V^*$. Electrons are confined to conduction states of the suspended section by p-n tunnel barriers. **(b)** Differential conductance dI/dV_{sd} as a function of source–drain voltage, V_{sd}, and V_g. Data are from device 1 at T=1.5 K. Dark blue represents dI/dV_{sd}=0, dark red represents dI/dV_{sd}=0.2 e^2/h. In the white regions (top and bottom of the plot), current levels exceeded the measurement range. The first four Coulomb diamonds, corresponding to discrete charge states, are labelled 1–4. In the large region of zero-conductance (to the left of Coulomb diamond 1) no electrons occupy the dot as the Fermi level crosses the NT bandgap. **(c)** A low-bias ($V_{sd} \sim 0.1$ mV) slice of the conductance plot shown in (a). The Coulomb peaks mark the transitions between different charge states.

in the conduction band of the suspended segment. A low-bias ($V_{sd} \sim 0.5$ mV) slice of this conductance plot shows the peaks in conduction (Coulomb peaks) which mark the transitions between different charge states (Fig 5.5c).

In the constant interaction model of quantum dots (Kouwenhoven et al. 1997) (Section 1.4) the position of the Nth Coulomb peak is given by

$$V_g(N) = \frac{C}{eC_g}\left(\varepsilon_N + \frac{Ne^2}{C}\right) + constant ,$$ (5.3)

where C is the total capacitance of the dot, C_g is the capacitance between the dot and the backgate, and ε_N is the single particle energy of the state filled by the Nth electron. From Eq 5.3, we see that the position of Coulomb peaks can be used to monitor the energy of electron states in the NTQD.

We begin by measuring the effect of magnetic field on the energy gap between the valence and conduction states of the suspended NT. In Fig. 5.6 the low-bias conductance of Device 1 is plotted in color scale as a function of V_g and B. We see the large region of zero-conductance corresponding to the Fermi level passing through the energy gap of the suspended region, followed by the first and second Coulomb peaks. The width of the large zero-conductance region shrinks as magnetic field is increased.

Figure 5.6 shows that valance and conduction states move closer together in energy as magnetic field is increased. The sharp turn-off of conductance at $V_g \sim$ 180mV corresponds to filling the last valence state in the suspended NT, while the first Coulomb peak above the bandgap marks the entry of the first electron into the NTQD. From Eq. 5.3, we expect the position of the first Coulomb peak to be $V_g = (C/eC_g)\varepsilon_1 + constant$, where ε_1 is the energy of the first filled conduction state. Estimating $C/C_g \sim 2.2$ using the width-to-height ratio of Coulomb diamonds in Fig. 5.5b (Kouwenhoven et al. 1997)(Section 1.4) we calculate $d\varepsilon_1/dB \sim$ -0.7meV/T. This
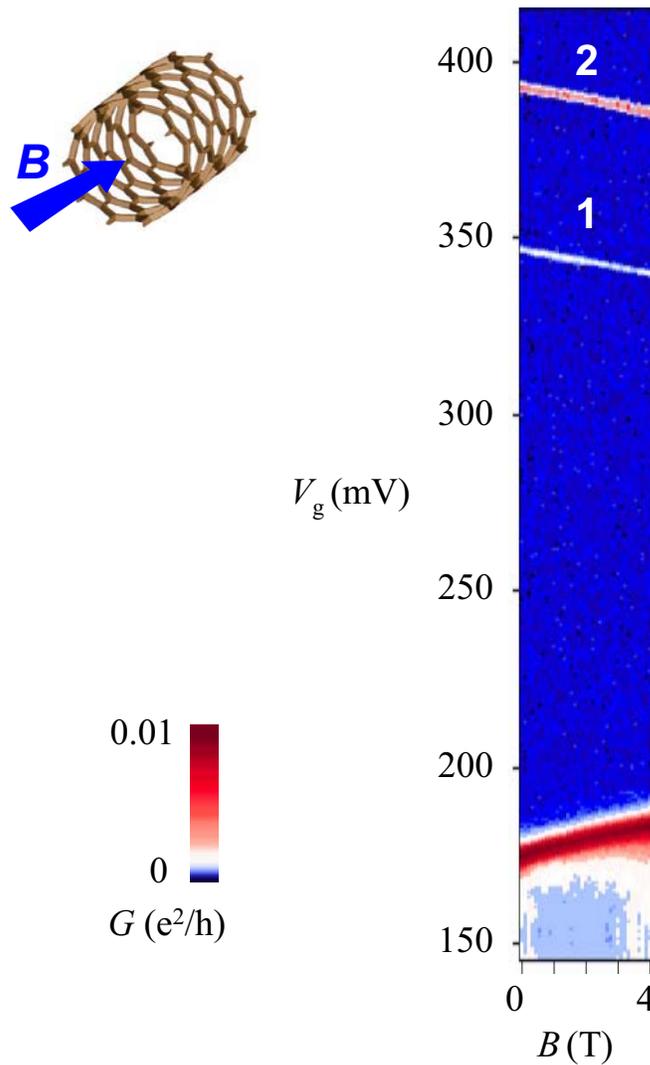
Figure 5.6 Changing bandgap of a nanotube quantum dot. The color scale shows low-bias conductance of device 1 at different magnetic fields (similar low-bias conductance data is shown in Fig 5.5c for $B = 0$). We associate the sharp turn-off of conductance at $V_g \sim 180$ mV to filling of the last valence state in the suspended NT. The Coulomb peaks at $V_g \sim 340$ mV and 380 mV mark the entry of the first and second electrons into the NTQD. The distance in V_g between the filling of the last valence state and putting the first electron in the NTQD is a measure of the NT bandgap.

energy shift suggests that the NT bandgap is reduced by ~ 1.4 meV/T, in good agreement with thermal activation measurements (see Table 1, device 1).

Bandgap reduction is expected in only one of the NT subbands. Energy shifts in the opposite direction are expected for states in the second subband. We now consider the NTQD in more detail to see how the two subbands contribute to the energy level spectrum.

We can estimate the energy level spectrum of our NTQD by considering the confinement of conduction electrons in a 1D potential well of length L. The confinement results in quantized $k_\parallel$ values which, combined with the dispersion relations $E_i(k_\parallel)$, determine the energy levels of the dot. Near the band-gap edge $E_i(k_\parallel)$ are parabolic, therefore, the energy levels of the first few conduction states should be:

$$\varepsilon(n,i,B_\parallel) = \frac{E_g^0}{2} + \frac{\hbar^2 \pi^2}{2 m_i^* L^2} n^2 \pm \mu_{orb} B_\parallel, \qquad (5.4)$$

where the quantum number n is a positive integer, the effective mass $m_i^* = E_g^{K_i}(B_\parallel)/2 v_F^2$, and +/− applies to the two different subbands (CW and CCW orbitals). For device 1 we expect an energy scale for level spacing $\delta = \hbar \pi/2 m^* L^2 \sim 0.25$ meV. The energy level spectrum described by Eq. 5.4 is plotted in Fig 5.7a. Energy level crossings occur when states from different subbands and different n become degenerate.

Figure 5.7b shows low-bias G-V_g plots of the first 8 Coulomb peaks in the NTQD. As the magnetic field is increased, peak positions move up and down between 1.2 and 1.6 mV/T. The fifth and subsequent peaks show clear changes between positive and negative slopes. Peaks appear to be paired, each pair having a different zigzag pattern.
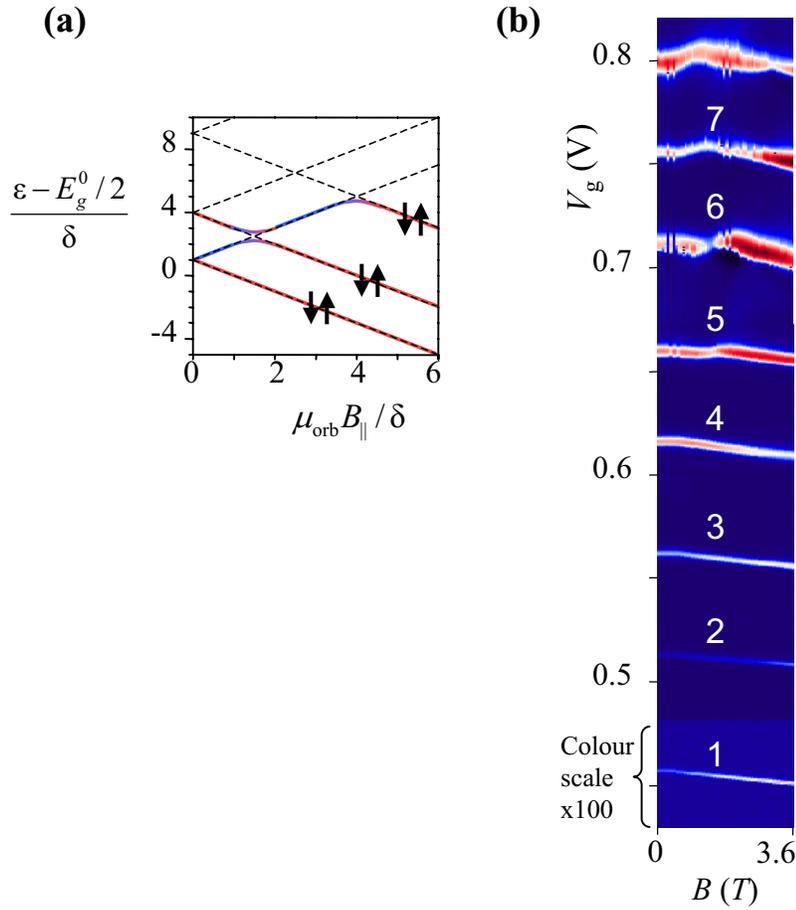
Figure 5.7 Energy levels of a nanotube quantum dot. **(a)** Modelled energies of quantum levels from Eq (5.3), approximating m_{eff} as constant. For device 1 we have $\delta \sim 0.25$ meV. Coloured lines represent the expected zigzags in the first six Coulomb peaks, with red and blue representing respectively CCW and CW states. Arrows indicate spin degeneracy for each state. **(b)** Low-bias conductance I/V_{sd} as a function of V_g and B showing the first eight Coulomb peaks of device 1, $\phi = 30°$. Dark blue represents $I/V_{sd}=0$; dark red represents $I/V_{sd}=0.35\ e^2/h$. The colour scale for peak 1 is magnified by 100 times.

The main features of Fig. 5.7b are described by the Eq. 5.4. Peaks with $d\varepsilon/dB > 0$ correspond to CW electron orbitals, while peaks with $d\varepsilon/dB < 0$ correspond to CCW electron orbital. The measured value of $\mu_{orb} = |\, d\varepsilon/dB_\parallel\,| = 0.7 \pm 0.1$ meV/T agrees with the values in Table 1 for Device 1. Furthermore, the striking difference between the first four peaks and later peaks is in qualitative agreement with the modeled spectrum (Fig. 5.7a). The first pair of peaks (spin up and spin down, $n = 1$, CCW orbital) are not expected to undergo level crossings. The second pair (peaks 3 and 4 in Fig. 5.7b) may undergo a level crossing at low field, however, the resolution of our data is limited by thermal broadening; levels separated by less than $4k_BT \approx 0.5$ meV merge together. The third and fourth pairs clearly show the changes in slope that are expected when level crossings occur. We conclude that there are quantum levels near the band-gap edges with both positive and negative orbital magnetic moments whose magnitudes are consistent with theoretical predictions (Ajiki & Ando 1993; Lu 1995). The Coulomb blockade model does not describe all the features in Fig. 5.7b. The detailed structure of this NTQD system may depend on effects such as exchange coupling (Tans et al. 1998; Liang et al. 2002), and will be the subject of future work.

5.7 Tranparency of p-n tunnel barriers

The tunnel barriers that confine electrons in our NTQD can be modified by a magnetic field. This effect will be useful for quantifying tunneling processes in NTs and for studying phenomena such as the Kondo effect which depend sensitively on the transparency of tunnel barriers to a quantum dot (Goldhaber-Gordon et al. 1998).

Figure 5.8a shows the second Coulomb peak from device 1 (the intersection of the first and second Coulomb diamonds in Fig. 5.5b). The peak shifts with magnetic field, as discussed in the previous section, and doubles in conductance as B reaches 3.6 T.

(a)

(b)
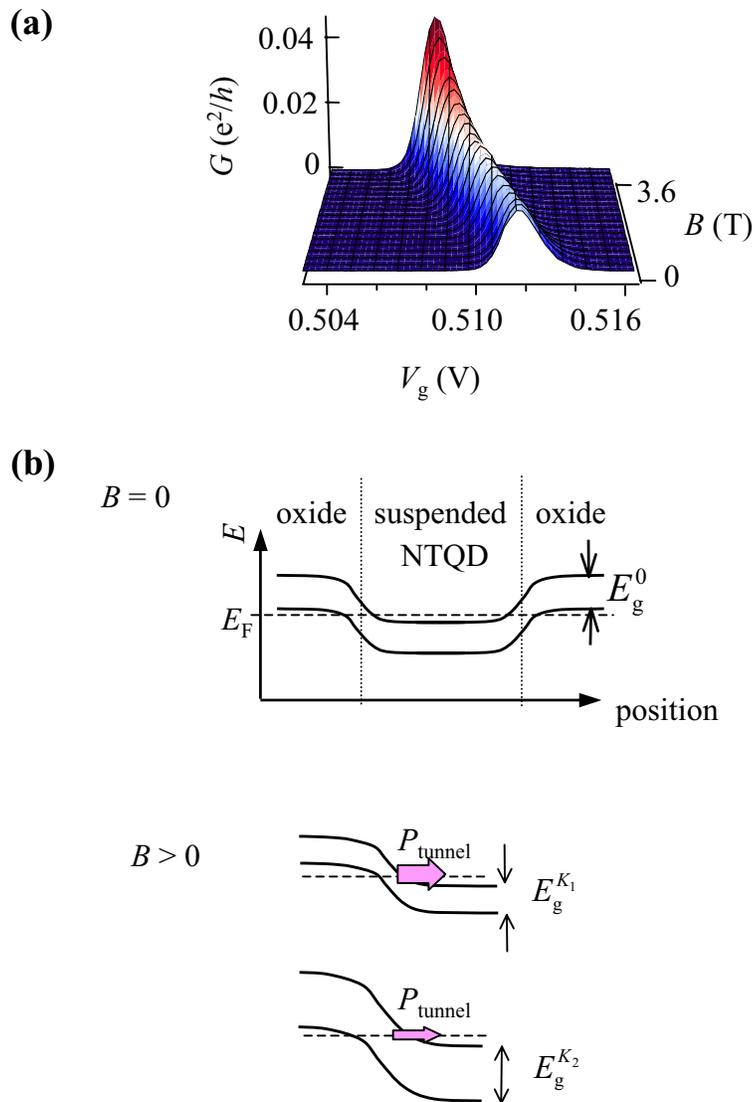
Figure 5.8 Changing transparency of the p-n tunnel barriers. **(a)** Low-bias conductance I/V_{sd} as a function of magnetic field B for the second Coulomb peak of Device 1, $\phi = 30°$, $V_{sd} = 0.5$ mV. Peak height increases with B. **(b)** Band bending model of NTQD. The tunnel barrier associated with one subband becomes more transparent for $B>0$ and the probability of tunneling P_{tunnel} increases. The tunnel barrier associated with the second subband becomes less transparent.

The increasing conductance of the second Coulomb peak shows that the tunnel barriers seen by the second electron become more transparent as B is increased. The p-n junctions responsible for the tunnel barriers are shown in Fig. 5.8b. The probability of tunneling across one of the barriers, P_{tunnel}, depends on the width of the junction and the NT bandgap (the tunneling calculations are described in detail in Section 4.5). Fig 5.8b illustrates the effect of magnetic field on the p-n junctions. One NT subband (labeled K_1 for convenience) has $dE_{gap}^{K_1}/dB < 0$. The p-n junction associated with this K_1 subband becomes smaller with B. Since the second electron occupies a state in the K_1 subband (the second Coulomb peak shifts towards lower energies as B is increased), we expect tunneling to increase as E^{K1}_{gap} decreases.

We also see evidence of decreasing tunneling probability to states in the K_2 subband ($dE_{gap}^{K_2}/dB > 0$). Coulomb peaks 5 and 6 in Fig. 5.7b show this effect most clearly. The conductance of peaks 5 and 6 is large when $d\varepsilon/dB < 0$ (tunneling into a state in the K_1 subband) but conductance drops when $d\varepsilon/dB > 0$ (tunneling into a state in the K_2 subband).

This simple model, based on $E_{gap}^{K_1}$ and $E_{gap}^{K_2}$ and treating the subbands as independent, does not explain all peak amplitudes seen in Fig. 5.7b. Tunnelling between subbands (Liang et al. 2001), and the shape of electron orbitals may also have important effects on tunneling rates.

5.8 Conclusions

We have measured μ_{orb} in NTs of diameter 2 – 5 nm and find values 10 - 20 times larger than the Bohr magneton and the spin magnetic moment in NTs (Cobden et al. 1998; Tans et al. 1998). These measurements confirm theoretical predictions for the magnetic properties of NTs (Ajiki & Ando 1993; Lu 1995).

Since the completion of this work similar observations have been reported by other authors. Zaric et al. (2004) studied the magneto-optical properties of small diameter NTs in aqueous solution. An applied magnetic field aligned the NTs (parallel to the field) and shifted the energy of optical absorption and optical emission peaks. New transport experiments on multi-walled NTs ($D \sim 30$nm) have also confirmed magnetic field induced changes in electronic structure (Coskun et al. 2004). By using very short devices (length $\sim$ 100 nm), Coskun et al. were able to eliminate weak localisation effects and study the coherent electron states on large diameter NTs. The results of both experiments are consistent with our measurements of μ_{orb}.

The large orbital magnetic moment of electrons in NTs give researchers a powerful new tool to control the electronic structure of NTs. The tunnel transparency of p-n barriers can be tuned by using a magnetic field to modify the band-gap. This will be useful, for example, to study Kondo physics in NTQDs (Nygard et al. 2000; Liang et al. 2002) at different tunneling strengths. Researchers can also tune the energy levels of electrons in the 1D box formed by a NT. By applying large magnetic fields it is possible to investigate the properties of a NT in which only one subband is occupied. Conversely, by matching the energies of different subband states, the interactions between states arising from CW and CCW orbits can be explored.

CHAPTER 6

CONCLUSION

6.1 Summary

We have demonstrated that carbon nanotube (NT) electronic structure can be tuned by mechanical stretching and by axial magnetic field. These results confirm theoretical predictions and show the significance of nanoscale geometry in determining the electronic properties of NTs.

To quantify electromechanical effects in NTs we developed methods to fabricate and manipulate suspended NTs, as discussed in Chapter 3. We showed that using an atomic force microscope it is possible to reversibly stretch suspended NTs while simultaneously monitoring tension forces. In Chapter 4 we combined mechanical manipulation techniques with electrical transport measurements to observe strain-induced changes in NT electronic structure. We found that applied mechanical strain opened a bandgap in metallic NTs and modified the bandgap of a semiconducting NTs. Our results were consistent with a linear relationship between strain and NT bandgap, with equal bandgap changes in degenerate subbands. As expected, the sign and magnitude of bandgap changes varied among different NTs and these differences could be attributed to different NT chiralities.

In Chapter 5 we demonstrated that the electronic structure of a NT can be tuned by an axial magnetic field. Measurements of thermally activated current, and energy shifts of the electron states in a NT quantum dot, showed that electron states near the NT bandgap couple strongly to magnetic field. The measurements also showed that subband degeneracy can be broken by axial magnetic field, with one bandgap growing and one bandgap shrinking as the field is increased. The observed coupling between

electron states and magnetic field was consistent with the predicted magnitude and direction of orbital magnetic moments in NTs.

6.2 Future outlook

The electromechanical and magnetic effects described in this thesis present new possibilities for studying quantum mechanics in NTs.

It is already well established that NTs are a versatile system for studying quantum mechanical effects. Electron coherence lengths in NTs are long and interesting behavior such as discrete electron energy levels, Fabery-Perot interference and the Kondo effect have been observed.

New possibilities lie in the ability tune NT properties. For example, by selectively straining different sections of a metallic NT, a series of semiconducting barriers can be created. Such a device would allow researchers to study the properties of electrons confined to a 1-D superlattice. Tuning the energies of electron states in a NT by magnetic field will also be an important tool. For example, it will be possible to learn more about interactions between electrons by examining the field-dependent energies of NT quantum dots containing two, three, four electrons etc.

APPENDIX

A.1 Forces during AFM imaging

Tapping mode imaging of suspended NTs can be understood more clearly if we consider the interaction between an oscillating AFM tip and a suspended NT. We find that upward pulling of the suspended NT by the AFM tip is the most violent aspect of the imaging process.

Figure A.1.1a shows a tapping mode image of a suspended NT. During imaging the AFM cantilever is driven into oscillation at its resonant frequency. The image is produced as the AFM tip scans across the surface and a feedback circuit tries to maintain constant oscillation amplitude. When the suspended NT is scanned, the tip height swings up and down wildly, as seen in the saw-tooth height profile (Fig. A.1.1a).

The large swings in tip height occur as the AFM tip sticks to the suspended NT and then pulls away. When the AFM tip meets the NT at the bottom of a swing, the oscillation amplitude drops because the cantilever/NT system has different resonance behavior than the bare cantilever (see Fig A.1.1b). The feedback circuit raises the AFM tip, attempting to restore oscillation amplitude. However, the NT is stuck to the tip. As the AFM tip is lifted the NT is put under greater strain and oscillation amplitude drops even further (Fig A.1.1b). Oscillation amplitude is not restored until the adhesion between NT and AFM tip is broken. As this process repeats, the AFM tip moves up and down, leading to the height swings in Fig. A.1.1a. The amplitude of the height variations is related to the slack in the suspended NT and the strength of the tip-tube adhesion.

When the adhesion force between AFM tip and NT is large, imaging can be violent. Poorly anchored NTs can be dislodged during imaging. Imaging could be

(a)

(b)
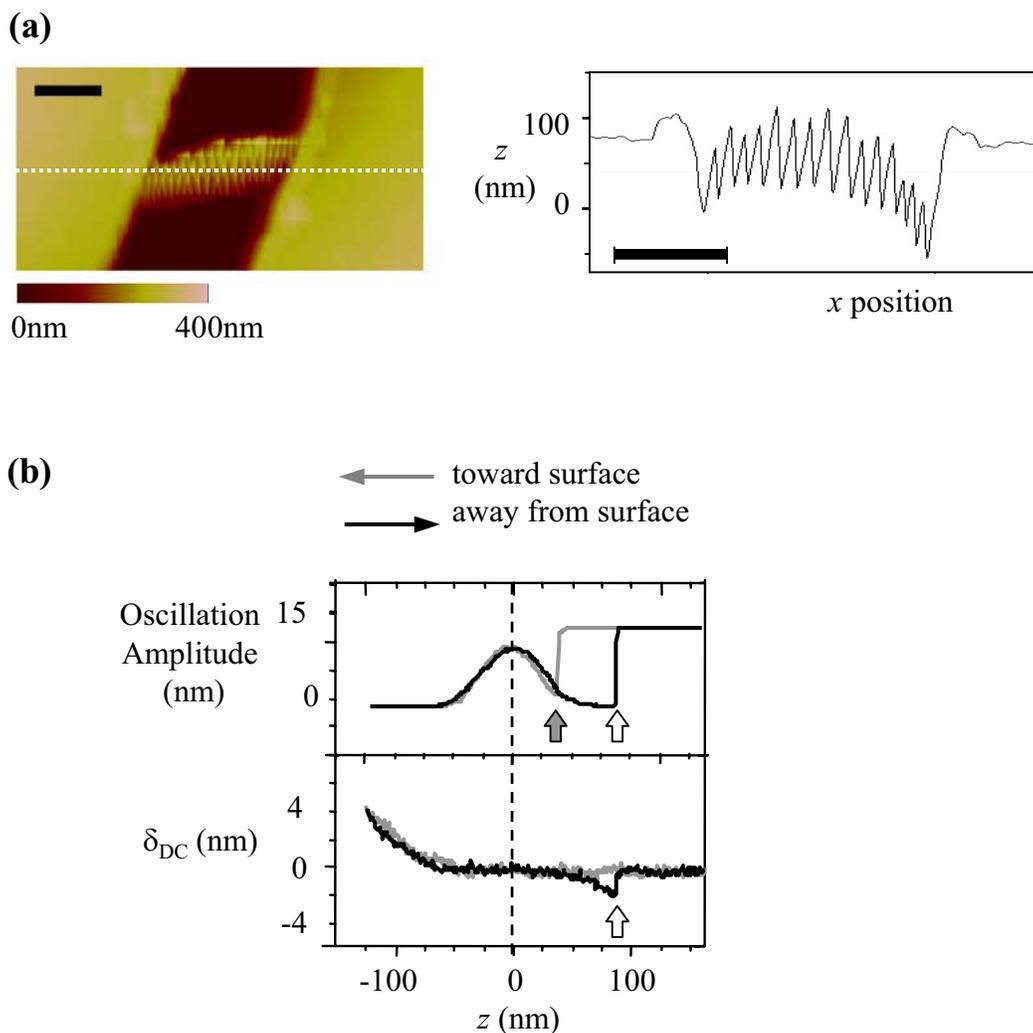
Figure A.1.1 (a) Tapping mode image of a suspended NT. A cross section of the image shows saw-tooth variations in tip height as the tip scans over the NT. The Cr/Au electrodes ($\approx$ 80 nm thick) are seen on the left and right side of the image and cross-section. Scale bars are 500nm. **(b)** Changes in resonance behavior when tip is in contact with NT. Oscillation amplitude drops when AFM tip touches the suspended NT (grey arrow). Oscillation amplitude is restored when tip/NT contact is broken (white arrow). The distance between the grey and white arrow corresponds to height variations in (a).

made less violent by reducing tip-tube adhesion forces. This may be possible by choosing appropriate material coatings for the AFM tip.

A.2 Voltage controlled tip-tube adhesion

We have investigated the possibility of using electrostatic forces to control the adhesion between an AFM tip and a NT.

Figures A.2.1b and c show the force needed to break contact between a NT and an AFM tip as a function of the voltage difference between them. The force increases significantly for both positive and negative voltages. The effect is more dramatic for the larger diameter NT show in Fig. A.2.1c.

The results suggest that the NT and the tip form two sides of a capacitor. The voltage difference induces positive (negative) charge on the NT which is attracted to negative (positive) charge on the AFM tip. In this model, electrostatic attraction will occur for both positive and negative voltages. The force depends on the area of the capacitor (the contact area between the NT and tip), and we expect larger forces for larger diameter NTs.

This voltage controlled adhesion may be useful for NT manipulation, where increasing adhesion forces could allow researchers to pick up NTs.
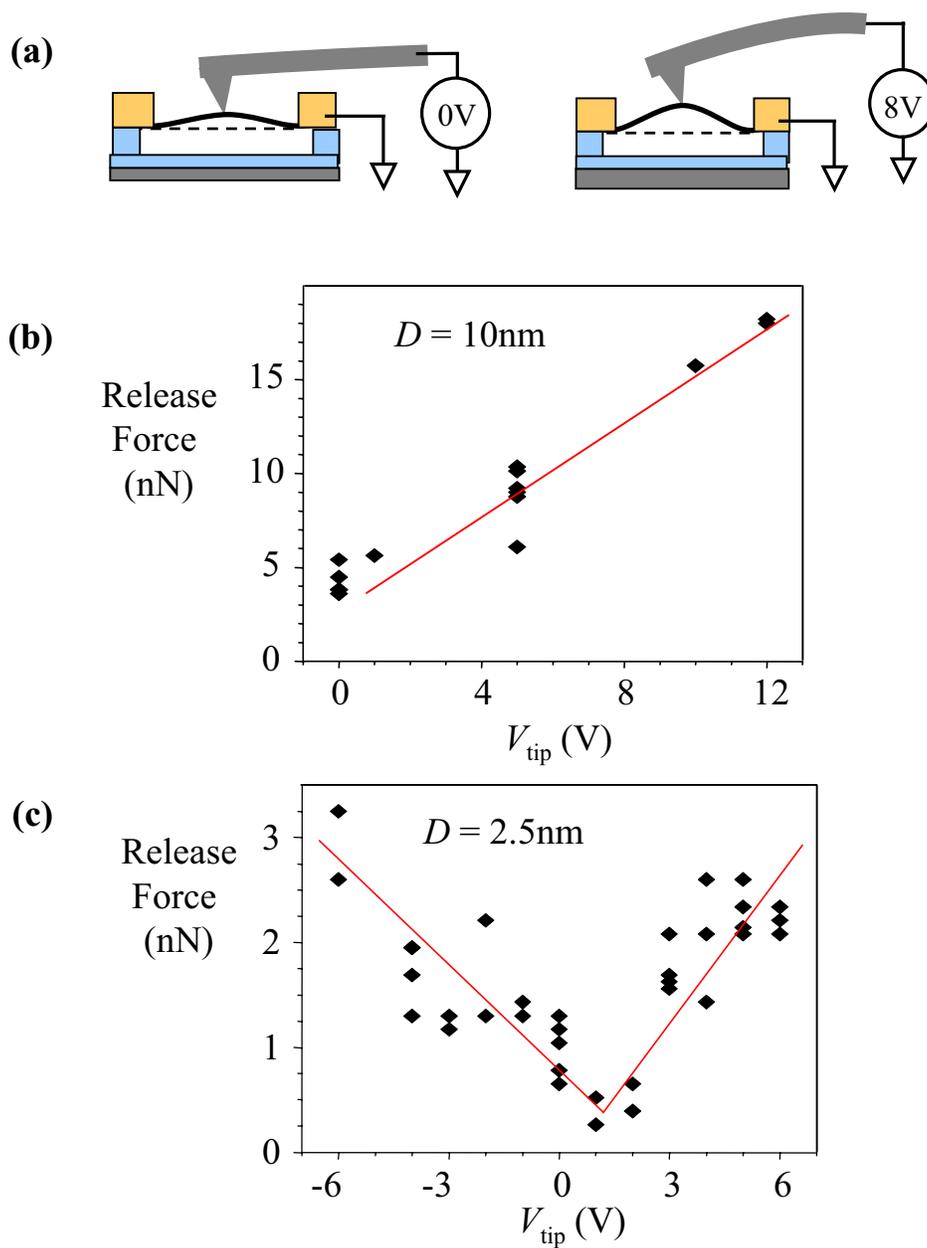
Figure A.2.1 Voltage control of release force. **(a)** Schematic of experiment. Adhesion forces increase as the voltage difference between NT and tip is increased. **(b) (c)** Deflection force on cantilever when NT/tip contact is broken for a NTs with $D = 10$nm and 2.5nm respectively.

A.3 Thermally activated current

The conductance of a semiconducting NT that has been depleted of charge carriers can be quantified using the Landauer-Buttiker formalism and the temperature-dependent Fermi-Dirac distribution.

The band bending diagram of a NT transistor in the off state is shown in Fig. A.3.1a. Electrons are transmitted if they have energy $E > E_F + E_{gap}$. Likewise, holes with energy corresponding to $E < E_F - E_{gap}$ are also transmitted. Carriers with energies between $E_F - E_{gap}$ and $E_F + E_{gap}$, however, can only be transmitted by tunneling to available states on the far side of the NT. Because the probability of tunneling across long distances is very small (Leonard & Tersoff 1999; Odintsov 2000) we assume that all carriers with energies between $E_F - E_{gap}$ and $E_F + E_{gap}$ are completely reflected.

From the Landauer-Buttiker formalism (Section 1.2), the current through a 1-D channel is

$$I = \frac{2e}{h} \cdot \int |t|^2 \left(f_R(E) - f_L(E) \right) dE \,,$$

and for small bias we have

$$I = \frac{2e}{h} \cdot eV \int |t|^2 \frac{df}{dE} dE \,. \tag{A.3.1}$$

For a semiconducting NT that is depleted of charge carriers the transmission probability $|t^2|$ is energy dependent. The integration in Eq. A3.1 is shown graphically in Fig. A.3.1b. The two shaded areas represent the energies where $|t|^2$ is non-zero. Assuming a constant $|t|^2$ for $E > E_F + E_{gap}$ and $E < E_F - E_{gap}$ we find

$$I \approx \frac{2e}{h}|t|^2 \cdot 2eV \int\limits_{E_F+E_{gap}}^{\infty} \left(\frac{df}{dE}\right) dE$$

$$= \frac{2e}{h}|t|^2 \cdot 2eV[f(E_F + E_{gap}) - f(\infty)]$$

$$= \frac{2e^2}{h}|t|^2 \left(\frac{2}{1+e^{E_{gap}/kT}}\right)V \;.$$

This is the thermally activated, off-state current though a 1-D subband of a NT transistor. The current depends on the width of the Fermi distributions ($\propto T$) compared to the size of E_{gap}. The current drops exponentially with bandgap when $E_{gap} \gg kT$.

(a)

(b)
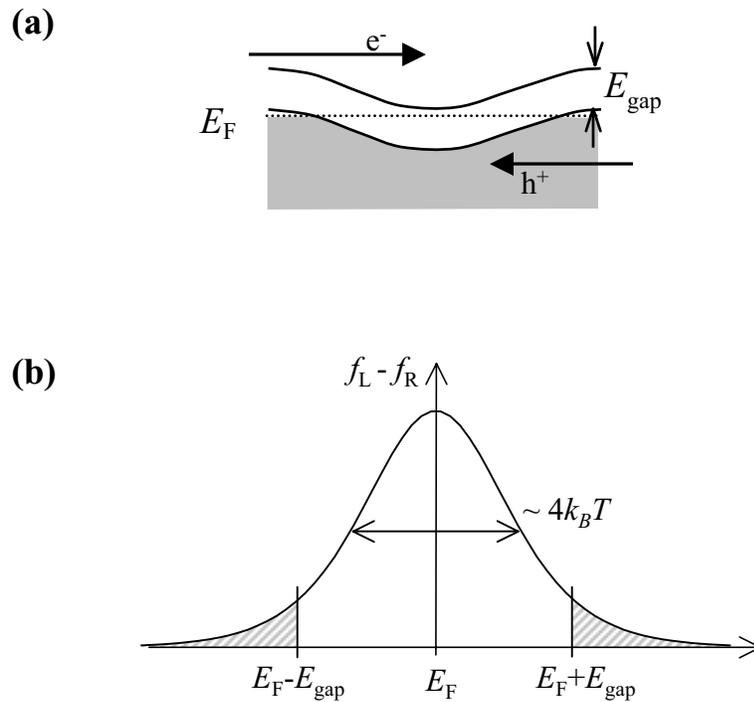
Figure A.3.1 Thermal activation of carriers. **(a)** Band diagram of a semiconducting NT in the off state. Thermally activated electron and holes can pass through the NT. **(b)** The difference between the Fermi functions in the left and right electrode, $f_L - f_R$. The shaded areas are integrated to find the off-state current through the NT transistor.

REFERENCES

Ajiki, H. and T. Ando, "Electronic states of carbon nanotubes." Journal of the Physical Society of Japan **62** 1255-1266 (1993).

Aronov, A. G. and Y. V. Sharvin, "Magnetic-flux effects in disordered conductors." Reviews of Modern Physics **59** 755-779 (1987).

Ashcroft, N. W. and N. D. Mermin *Solid state physics*. Orlando, Saunders College (1976).

Bachilo, S. M., M. S. Strano, et al., "Structure-assigned optical spectra of single-walled carbon nanotubes." Science **298** 2361-2366 (2002).

Bachtold, A., M. S. Fuhrer, et al., "Scanned probe microscopy of electronic transport in carbon nanotubes." Physical Review Letters **84** 6082-6085 (2000).

Bachtold, A., C. Strunk, et al., "Aharonov-Bohm oscillations in carbon nanotubes." Nature **397** 673-675 (1999).

Bockrath, M., D. H. Cobden, et al., "Single-electron transport in ropes of carbon nanotubes." Science **275** 1922-1925 (1997).

Calvert, P., "Nanotube composites - a recipe for strength." Nature **399** 210-211 (1999).

Chauvet, O., L. Forro, et al., "Magnetic anisotropies of aligned carbon nanotubes." Physical Review B **52** 6963-6966 (1995).

Cobden, D. H., M. Bockrath, et al., "Spin splitting and even-odd effects in carbon nanotubes." Physical Review Letters **81** 681-684 (1998).

Coskun, U. C., T. C. Wei, et al., "h/e magnetic flux modulation of the energy gap in nanotube quantum dots." Science **304** 1132-1134 (2004).

Craighead, H. G., "Nanoelectromechanical systems." Science **290** 1532-1535 (2000).

Cumings, J. and A. Zettl, "Low-friction nanoscale linear bearing realized from multiwall carbon nanotubes." Science **289** 602-604 (2000).

Dai, H. J., J. H. Hafner, et al., "Nanotubes as nanoprobes in scanning probe microscopy." Nature **384** 147-150 (1996).

Datta, S. *Electron Transport in Mesoscopic Systems*. Cambridge, Cambridge University Press (1995).

de Pablo, P. J., C. Gomez-Navarro, et al., "Nonlinear resistance versus length in single-walled carbon nanotubes." Physical Review Letters **88** 036804 (2002).

de Pablo, P. J., C. Gomez-Navarro, et al., "Performing current versus voltage measurements of single-walled carbon nanotubes using scanning force microscopy." Applied Physics Letters **80** 1462-1464 (2002).

Decossas, S., G. Cappello, et al., "Interaction forces between carbon nanotubes and an AFM tip." Europhysics Letters **53** 742-748 (2001).

Dekker, C., "Carbon nanotubes as molecular quantum wires." Physics Today **52** 22-28 (1999).

Dresselhaus, M. S., G. Dresselhaus, et al., Eds. *Carbon nanotubes*. Topics in Applied Physics. New York, Springer (2001).

Fujiwara, A., K. Tomiyama, et al., "Quantum interference of electrons in multiwall carbon nanotubes." Physical Review B **60** 13492-13496 (1999).

Goldhaber-Gordon, D., H. Shtrikman, et al., "Kondo effect in a single-electron transistor." Nature **391** 156-159 (1998).

Heyd, R., A. Charlier, et al., "Uniaxial-stress effects on the electronic properties of carbon nanotubes." Physical Review B **55** 6820-6824 (1997).

Hutter, J. L. and J. Bechhoefer, "Calibration of atomic-force microscope tips." Review of Scientific Instruments **64** 1868-1873 (1993).

Jarillo-Herrero, P., S. Sapmaz, et al., "Electron-hole symmetry in a semiconducting carbon nanotube quantum dot." Nature **429** 389-392 (2004).

Javey, A., J. Guo, et al., "Ballistic carbon nanotube field-effect transistors." Nature **424** 654-657 (2003).

Kane, C. L. and E. J. Mele, "Size, shape, and low energy electronic structure of carbon nanotubes." Physical Review Letters **78** 1932-1935 (1997).

Kim, G. T., G. Gu, et al., "Simple method to prepare individual suspended nanofibers." Applied Physics Letters **80** 1815-1817 (2002).

Kong, J., H. T. Soh, et al., "Synthesis of individual single-walled carbon nanotubes on patterned silicon wafers." Nature **395** 878-881 (1998).

Kong, J., E. Yenilmez, et al., "Quantum interference and ballistic transmission in nanotube electron waveguides." Physical Review Letters **87** 106801 (2001).

Kouwenhoven, L. P. and C. M. Marcus, "Quantum dots." Physics World **11** 35-39 (1998).

Kouwenhoven, L. P., C. M. Marcus, et al. "Electron transport in quantum dots." *Mesoscopic Electron Transport*. eds. L. P. Kouwenhoven, G. Schon and L. L. Sohn, Kluwer, Dordrecht (1997).

Krishnan, A., E. Dujardin, et al., "Young's modulus of single-walled nanotubes." Physical Review B **58** 14013-14019 (1998).

Kwon, Y. K. and D. Tomanek, "Electronic and structural properties of multiwall carbon nanotubes." Physical Review B **58** 16001-16004 (1998).

Lee, J. O., J. R. Kim, et al., "Observation of magnetic-field-modulated energy gap in carbon nanotubes." Solid State Communications **115** 467-471 (2000).

Leonard, F. and J. Tersoff, "Novel length scales in nanotube devices." Physical Review Letters **83** 5174-5177 (1999).

Liang, W. J., M. Bockrath, et al., "Fabry-Perot interference in a nanotube electron waveguide." Nature **411** 665-669 (2001).

Liang, W. J., M. Bockrath, et al., "Shell filling and exchange coupling in metallic single-walled carbon nanotubes." Physical Review Letters **88** 126801 (2002).

Liu, L., C. S. Jayanthi, et al., "Controllable reversibility of an sp(2) to sp(3) transition of a single wall nanotube under the manipulation of an AFM tip: A nanoscale electromechanical switch?" Physical Review Letters **84** 4950-4953 (2000).

Lu, J. P., "Novel magnetic-properties of carbon nanotubes." Physical Review Letters **74** 1123-1126 (1995).

Lu, J. P., "Elastic properties of carbon nanotubes and nanoropes." Physical Review Letters **79** 1297-1300 (1997).

Maiti, A., A. Svizhenko, et al., "Electronic transport through carbon nanotubes: Effects of structural deformation and tube chirality." Physical Review Letters **88** 126805 (2002).

McEuen, P. L., "Single-wall carbon nanotubes." Physics World **13** 31-36 (2000).

McEuen, P. L., M. S. Fuhrer, et al., "Single-walled carbon nanotube electronics." IEEE Transactions on Nanotechnology **1** 78-85 (2002).

Minot, E. D., Y. Yaish, et al., "Determination of electron orbital magnetic moments in carbon nanotubes." Nature **428** 536-539 (2004).

Minot, E. D., Y. Yaish, et al., "Tuning carbon nanotube band gaps with strain." Physical Review Letters **90** (2003).

Nardelli, M. B., B. I. Yakobson, et al., "Brittle and ductile behavior in carbon nanotubes." Physical Review Letters **81** 4656-4659 (1998).

Nygard, J. and D. H. Cobden, "Quantum dots in suspended single-wall carbon nanotubes." Applied Physics Letters **79** 4216-4218 (2001).

Nygard, J., D. H. Cobden, et al., "Kondo physics in carbon nanotubes." Nature **408** 342-346 (2000).

Odintsov, A. A., "Schottky barriers in carbon nanotube heterojunctions." Physical Review Letters **85** 150-153 (2000).

Odom, T. W., J. L. Huang, et al., "Atomic structure and electronic properties of single-walled carbon nanotubes." Nature **391** 62-64 (1998).

Park, J. W. and P. L. McEuen, "Formation of a p-type quantum dot at the end of an n-type carbon nanotube." Applied Physics Letters **79** 1363-1365 (2001).

Park, J. Y., Y. Yaish, et al., "Electrical cutting and nicking of carbon nanotubes using an atomic force microscope." Applied Physics Letters **80** 4446-4448 (2002).

Park, J. Y., S. Rosenblatt, et al., "Electron-phonon scattering in metallic single-walled carbon nanotubes." Nano Letters **4** 517-520 (2004)

Paulson, S., M. R. Falvo, et al., "In situ resistance measurements of strained carbon nanotubes." Applied Physics Letters **75** 2936-2938 (1999).

Poncharal, P., Z. L. Wang, et al., "Electrostatic deflections and electromechanical resonances of carbon nanotubes." Science **283** 1513-1516 (1999).

Postma, H. W. C., A. Sellmeijer, et al., "Manipulation and imaging of individual single-walled carbon nanotubes with an atomic force microscope." Advanced Materials **12** 1299 (2000).

Ralph, D. C., C. T. Black, et al., "Spectroscopic measurements of discrete electronic states in single metal particles." Physical Review Letters **74** 3241-3244 (1995).

Ramirez, A. P., R. C. Haddon, et al., "Magnetic-susceptibility of molecular carbon - nanotubes and fullerite." Science **265** 84-86 (1994).

Reed, M. A., "Molecular-scale electronics." Proceedings of the IEEE **87** 652-658 (1999).

Rochefort, A., D. R. Salahub, et al., "The effect of structural distortions on the electronic structure of carbon nanotubes." Chemical Physics Letters **297** 45-50 (1998).

Rosenblatt, S., Y. Yaish, et al., "High performance electrolyte gated carbon nanotube transistors." Nano Letters **2** 869-872 (2002).

Salvetat, J. P., J. M. Bonard, et al., "Mechanical properties of carbon nanotubes." Applied Physics A - Materials Science & Processing **69** 255-260 (1999).

Sazonova, V., Y. Yaish et al., "A tunable carbon nanotube electromechanical oscillator." to appear in Nature (2004).

Tans, S. J. and C. Dekker, "Molecular transistors - Potential modulations along carbon nanotubes." Nature **404** 834-835 (2000).

Tans, S. J., M. H. Devoret, et al., "Individual single-wall carbon nanotubes as quantum wires." Nature **386** 474-477 (1997).

Tans, S. J., M. H. Devoret, et al., "Electron-electron correlations in carbon nanotubes." Nature **394** 761-764 (1998).

Tans, S. J., A. R. M. Verschueren, et al., "Room-temperature transistor based on a single carbon nanotube." Nature **393** 49-52 (1998).

Tombler, T. W., C. W. Zhou, et al., "Reversible electromechanical characteristics of carbon nanotubes under local-probe manipulation." Nature **405** 769-772 (2000).

Treacy, M. M. J., T. W. Ebbesen, et al., "Exceptionally high Young's modulus observed for individual carbon nanotubes." Nature **381** 678-680 (1996).

Vanwees, B. J., H. Vanhouten, et al., "Quantized conductance of point contacts in a two-dimensional electron-gas." Physical Review Letters **60** 848-850 (1988).

Wallace, P. R., "The band theory of graphite." Physical Review **71** 622-634 (1947).

Walters, D. A., M. J. Casavant, et al., "In-plane-aligned membranes of carbon nanotubes." Chemical Physics Letters **338** 14-20 (2001).

Walters, D. A., L. M. Ericson, et al., "Elastic strain of freely suspended single-wall carbon nanotube ropes." Applied Physics Letters **74** 3803-3805 (1999).

Wang, X. K., R. P. H. Chang, et al., "Magnetic-susceptibility of buckytubes." Journal of Materials Research **9** 1578-1582 (1994).

Wharam, D. A., T. J. Thornton, et al., "One-dimensional transport and the quantization of the ballistic resistance." Journal of Physics C-Solid State Physics **21** 209-214 (1988).

White, C. T. and J. W. Mintmire, "Density of states reflects diameter in nanotubes." Nature **394** 29-30 (1998).

Whittaker, J. D., M. Brink, et al., "Self-aligned mechanical attachment of carbon nanotubes to silicon dioxide structures by selective silicon dioxide chemical-vapor deposition." Applied Physics Letters **83** 5307-5309 (2003).

Wildoer, J. W. G., L. C. Venema, et al., "Electronic structure of atomically resolved carbon nanotubes." Nature **391** 59-62 (1998).

Wong, E. W., P. E. Sheehan, et al., "Nanobeam mechanics: Elasticity, strength, and toughness of nanorods and nanotubes." Science **277** 1971-1975 (1997).

Yaish, Y., J.-Y. Park, et al., "Electrical Nanoprobing of Semiconducting Carbon Nanotubes Using an Atomic Force Microscope." Physical Review Letters **92** 046401 (2004).

Yakobson, B. I., C. J. Brabec, et al., "Nanomechanics of carbon tubes: Instabilities beyond linear response." Physical Review Letters **76** 2511-2514 (1996).

Yang, L., M. P. Anantram, et al., "Band-gap change of carbon nanotubes: Effect of small uniaxial and torsional strain." Physical Review B **60** 13874-13878 (1999).

Yang, L. and J. Han, "Electronic structure of deformed carbon nanotubes." Physical Review Letters **85** 154-157 (2000).

Yu, M. F., O. Lourie, et al., "Strength and breaking mechanism of multiwalled carbon nanotubes under tensile load." Science **287** 637-640 (2000).

Zhang, P. H., P. E. Lammert, et al., "Plastic deformations of carbon nanotubes." Physical Review Letters **81** 5346-5349 (1998).

Zhou, C. W., J. Kong, et al., "Intrinsic electrical properties of individual single-walled carbon nanotubes with small band gaps." Physical Review Letters **84** 5604-5607 (2000).